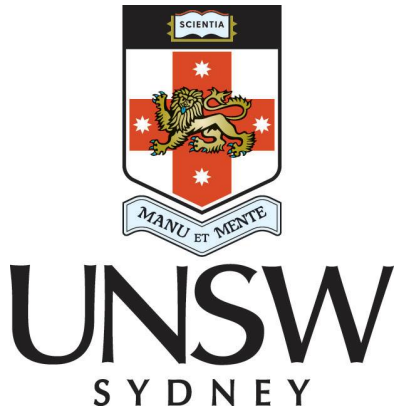


Constraining Deep Mixing in RGB Stars with APOGEE and Kepler

Honours Thesis

Christopher J. Brockett
z5075621

Supervisor: Dr Sarah Martell



School of Physics
University of New South Wales
Sydney, Australia
November 2019

Statement of Originality

I hereby declare that this submission is my own work and to the best of my knowledge it contains no materials previously published or written by another person, or substantial proportions of material which have been accepted for the award of any other degree or diploma at UNSW or any other educational institution, except where due acknowledgement is made in the thesis. Any contribution made to the research by others, with whom I have worked at UNSW or elsewhere, is explicitly acknowledged in the thesis. I also declare that the intellectual content of this thesis is the product of my own work, except to the extent that assistance from others in the project's design and conception or in style, presentation and linguistic expression is acknowledged.

Christopher J. Brockett

Date

Abstract

Deep mixing is a process that occurs on the upper red giant branch which results in a decrease of surface [C/Fe] and increase in surface [N/Fe] and the $^{13}\text{C}/^{12}\text{C}$ ratio. The mixing rate is known to be dependent on both the mass and composition of the star, but the strength of the dependence has not been clearly demonstrated in field stars. This process is a poorly understood aspect of stellar evolutionary theory, and a strong understanding is required to properly understand the chemical evolution of both stars and galaxies. This project was designed to examine the dependence of deep mixing on both mass and metallicity. To do this we use the APOGEE survey for spectroscopically determined abundances, and masses derived by asteroseismology by the *Kepler* survey. Using these masses we build a random forest regression model to predict masses for stars without seismology data. We present Mixing rates for stars in different mass and metallicity models, finding a maximum mixing rate of $d[\text{C}/\text{N}]/d \log(g) = 0.96$ for stars in the mass range of $1.00 \leq M/M_{\odot} < 1.25$ and metallicity $[\text{Fe}/\text{H}] \leq -1.75$. We then compare our results for field stars to globular clusters in the APOGEE dataset, finding the metallicity dependence of the mixing rate is more difficult to determine due to the comparatively few stars in the clusters. Lastly we compare to theoretical predictions, and we note that the model is unable to consistently match the observed mixing rates, under predicting the mixing rates at intermediate masses ($1.25 \leq M/M_{\odot} < 1.75$).

Acknowledgements

A huge thank you to everyone who has helped me throughout the past two years. To my supervisor Dr Sarah Martell: thank you so much for everything. I could not have asked for a more capable, caring and brilliant supervisor. Without you none of this would have happened, so thank you so much for everything.

To Mum, Dad and Kayla: Thanks for supporting me through all my studies, you have made this all possible so thank you so much for that.

To my housemate and fellow Honours student Kirsten: Thank you for being there for me all year round. You and I have dealt with this year together and I am so thankful to have you in my life.

Contents

1	Introduction	1
2	General Background	3
2.1	Stellar Structure and Evolution	3
2.1.1	Energy Transport in Stellar Interiors	3
2.1.2	Stellar Nucleosynthesis	4
2.1.3	Stellar Evolution	7
2.2	Spectroscopy	13
2.2.1	Stellar Spectra	13
2.2.2	Measuring Stellar Properties	14
2.3	Asteroseismology	17
2.3.1	Stellar Oscillations and Asteroseismology	17
2.3.2	Scaling Relations	19
3	Deep Mixing on the RGB	21
3.1	Observational Evidence of Deep Mixing on the RGB	21
3.1.1	Weak G-Band Stars and Early Observations	21
3.1.2	Modern Survey Projects	23
3.2	Mixing Models	26
3.2.1	Rotational Mixing	26
3.2.2	Magnetic Mixing	26
3.2.3	Thermohaline Mixing	27
4	Data Sources	33
4.1	APOGEE	33
4.2	Kepler & K2	35
4.3	The APOKASC Catalogue	36
4.4	Catalogue Matching and Sample Selection	37

5 Predicting Masses	39
5.1 Machine Learning Methods	39
5.1.1 Linear Regression	40
5.1.2 Random Forest Regression	40
5.1.3 Multilayer Perceptron	40
5.1.4 Bayesian Ridge Regression	41
5.2 Determining the Best Model	41
5.3 Uncertainties in Predictions	43
5.4 Predicting APOGEE Masses	45
6 Constraining Mixing Rates	47
6.1 Finding the Red Giant Branch Bump	47
6.2 Mixing Rates as Functions of Mass and Metallicity	52
7 Discussion	55
7.1 Comparison to Globular Clusters	55
7.1.1 The Masseron Catalogue	55
7.1.2 The Nataf Catalogue	58
7.1.3 ASPCAP Globular Clusters	59
7.2 Comparison with Theoretical Predictions	62
7.3 Comparison to the Literature	66
8 Conclusions	69
8.1 Future Work	70
A Additional Figures & Tables	73
B Python Code	77
B.1 Mass Prediction Code	77
B.2 Determine Mixing Rates	82
Bibliography	87

List of Symbols, Abbreviations and Nomenclature

Abbreviations

IR	Infrared
NIR	Near-Infrared
LTE	Local Thermodynamic Equilibrium
UV	Ultra-Violet

Constants

a	Radiation Constant	$7.566 \times 10^{-16} \text{ J m}^{-3} \text{ K}^{-4}$
c	Speed of Light	$2.998 \times 10^8 \text{ m s}^{-1}$
L_{\odot}	Solar Luminosity	$3.828 \times 10^{26} \text{ W}$
M_{\odot}	Solar Mass	$1.988 \times 10^{30} \text{ kg}$
R_{\odot}	Solar Radius	$6.957 \times 10^8 \text{ m}$

Stellar Evolutionary States

MS	Main Sequence
SGB	Sub-Giant Branch
RGB	Red Giant Branch
RC	Red Clump
HB	Horizontal Branch
AGB	Asymptotic Giant Branch

Nomenclature

dex	An order of magnitude
H-R Diagram	Hertzsprung-Russell Diagram
Population I	Metal rich stars, typically young
Population II	Metal poor stars, typically old

Other Symbols

$\log(g)$	\log_{10} of surface gravity in cm s^{-2}
\odot	Solar Value
A_V	Total Extinction in the V-Band
M_V	Absolute Magnitude in the V-Band
T_{eff}	Effective Temperature

Photometric Filters

G-band	Green photometric filter	$\lambda_{\text{eff}} = 464 \text{ nm}, \Delta\lambda = 128 \text{ nm}$
V-band	Visual photometric filter	$\lambda_{\text{eff}} = 551 \text{ nm}, \Delta\lambda = 88 \text{ nm}$
H-band	Infrared photometric filter	$\lambda_{\text{eff}} = 1630 \text{ nm}, \Delta\lambda = 307 \text{ nm}$

List of Figures

2.1	The CNO bi-cycle	7
2.2	Evolution of a $5M_{\odot}$ star	8
2.3	Evolution of stars with masses $M = 1, 1.25$ and $1.5M_{\odot}$	9
2.4	Evolution of stars with masses $M = 2.25$ and $3M_{\odot}$	10
2.5	Present-day photospheric elemental abundances as a function of atomic number	15
2.6	Comparison of APOGEE spectra for two stars of different metallicities	16
2.7	Power spectrum of solar oscillations	18
2.8	Asteroseismc H-R Diagram	19
2.9	Schematic diagram of the power spectrum of solar oscillations	20
3.1	Carbon abundances as a function of absolute magnitude . . .	22
3.2	Li abundances plotted against absolute magnitude	24
3.3	[C/N] ratios for RGB and RC stars as a function of $\log g$ for different selections of metallicity	25
3.4	[C/N] distributions for synthetic stellar populations	30
3.5	[C/N] as a function of [Fe/H] for synthetic populations and stars in the Gaia-ESO survey	31
4.1	APOGEE in the context of other Galactic archaeology surveys	34
4.2	Diagram of the Sloan Foundation Telescope and APOGEE Spectrographs	35
4.3	H-R Diagram of the stars in APOKASC-2	36
5.1	Comparison of the four different regression methods for predicting masses	42
5.2	Mass predicted by RFR plotted against the mass determined by asteroseismology for APOKASC stars.	43

5.3	The normalised distribution of asteroseismic mass M_{Astero} and predicted mass M_{Pred} for each mass selection.	44
5.4	Distribution of predicted masses from the APOGEE dataset	46
5.5	Predicted mass vs metallicity for APOGEE stars.	46
6.1	Normalised histogram of surface gravity for each of the subsets of APOGEE. The blue dashed lines indicate upper and lower bounds for the RGBb found using the Dartmouth isochrones (Dotter <i>et al.</i> , 2008), and the red dashed line is the mean surface gravity of the RGBb for each selection of mass and metallicity. The RGBb can be identified in many subsets as a large overdensity at a small range of surface gravities, and is most clearly seen in the highest metallicity stars. The isochrones tend to predict the RGBb at lower surface gravities than we observe. The histograms have been normalised to increase readability.	50
6.2	[C/N] abundance ratio for different selections of mass and metallicity in the APOGEE dataset.	51
7.1	[C/Fe] abundances for M3, M5, M13, M71 and M107	56
7.2	[N/Fe] abundance against $\log(g)$ for globular clusters determined by Nataf <i>et al.</i> (2019)	59
7.3	Comparison of [C/Fe] vs $\log(g)$ for the three different pipelines to analyse GCs from APOGEE spectra.	61
7.4	APOGEE carbon-nitrogen abundance ratio plotted against surface gravity, grouped by both mass and metallicity	64
7.5	Histograms of predicted mass (M_{Pred} , a), metallicity (b), carbon and nitrogen abundances (c) and (d) respectively) for the full APOGEE set used in this project, and the subset analysed in Shetrone <i>et al.</i> (2019)	67
A.1	[N/Fe] abundances for M3, M5, M13, M71 and M107	74
A.2	Comparison of [N/Fe] vs $\log(g)$ for the three different pipelines to analyse GCs from APOGEE spectra.	74
A.3	[C/Fe] abundances for APOGEE stars, selected by their mass and metallicity.	75
A.4	[N/Fe] abundances for APOGEE stars, selected by their mass and metallicity.	76

List of Tables

2.1	Evolutionary Lifetimes (10^8 yr)	11
3.1	[C/Fe] and [N/Fe] abundance predicted in Charbonnel and Lagarde (2010) in models with and without thermohaline and rotation induced mixing.	30
5.1	Correlation coefficient and root-mean-squared errors for the four mass prediction methods.	41
5.2	Properties of the skewed-normal distribution fitted to each mass range.	45
6.1	Synthetic isochrone parameters from Dotter <i>et al.</i> (2008). . .	48
6.2	Location of the RGBb in surface gravity at different mass and metallicity ranges. Stars with masses greater than $2.2M_\odot$ are not observed to appear in the RGBb in these isochrones. . . .	49
6.3	Change in [C/N] abundance for different selections of mass and metallicity.	52
7.1	Mixing rates for [C/Fe] and [N/Fe] from Masseron <i>et al.</i> (2019). .	58
7.2	The mixing rates from the Nataf <i>et al.</i> (2019) catalogue. . . .	60
7.3	Mixing rates using the ASPCAP abundances and surface gravities	60
7.4	Comparison between $\frac{d[\text{C}/\text{N}]}{d\log(g)}$ for the three different analyses of globular clusters in APOGEE.	61
7.5	Mixing rates for 24 of the Lagarde <i>et al.</i> (2012) models with thermohaline and rotational mixing (Th+Rot) and without any deep mixing (None). The file name of each model used is listed as well.	62

7.6	$\frac{d[C/N]}{d\log(g)}$ for the APOGEE field stars and models developed by Lagarde <i>et al.</i> (2012). The metallicity and mass ranges are the ranges used for the selection of APOGEE stars, the numbers in brackets are the mass and metallicity of the Lagarde model.	66
7.7	Mixing rates at different metallicity ranges in APOGEE as found by (Shetrone <i>et al.</i> , 2019).	66
A.1	Change in [C/Fe] abundance for different selections of mass and metallicity.	75
A.2	Change in [N/Fe] abundance for different selections of mass and metallicity.	76

CHAPTER 1

Introduction

Developing a strong understanding of stellar evolution has long been one of the primary goals of astrophysics. Studying the evolution of stars not only leads to insights about how stars change over time, but also reveals information on the internal structure and composition of the star, how mass and composition alter these processes, and how these process affect the chemical evolution of galaxies. Galactic archaeology is the name given to the study of how these evolutionary processes will alter the chemical composition of the Galaxy, and uses methods such as chemical tagging to study the chemical evolution of stars. In order for galactic archaeology to be accurate, a strong understanding of the chemical evolution of stars is required, particularly with how mass and initial composition of the stars can affect evolutionary processes. This project is focused on the analysis of just one evolutionary process that is currently poorly understood.

This process, known as “deep mixing”, occurs on the upper-red giant branch (RGB) stage of a star’s evolution, and has been observed since the 1970s (Zinn, 1973). The mixing process is often referred to as a non-canonical process, as standard stellar evolution theories do not predict this process occurring. The observational signs of this mixing event are changes in the surface abundances in stars on the upper RGB, notably a decrease in ^{12}C and an increase in ^{13}C and ^{14}N . The leading explanation for this non-canonical mixing is known as “thermohaline mixing” (Charbonnel and Zahn, 2007), though there are doubts as to whether this process alone is strong enough to produce the changes in abundance observed.

Much of the previous work on this topic has been focused either in globular clusters (Carbon *et al.*, 1982; Langer *et al.*, 1986; Smith and Martell, 2003; Martell *et al.*, 2008; Angelou *et al.*, 2012), or in field stars without

strict knowledge of their masses and ages (Gratton *et al.*, 2000; Lagarde *et al.*, 2019; Shetrone *et al.*, 2019). A knowledge of mass and age will aid in the understanding of the mixing process, specifically its mass dependence, which is theorised but has not been well demonstrated in field stars. It will also help in determining whether thermohaline mixing predicts the mixing rates of stars well, or if different mixing process is required to reproduce observations. This project will differ from much of the previous work in this topic as we use asteroseismology from the *Kepler* survey (Borucki *et al.*, 2010) to determine masses for many stars on the RGB, and examine how the observed mixing rate compares to predictions at the same mass and metallicity. Combining the seismology data with spectroscopically determined abundances from the APOGEE survey (Majewski *et al.*, 2017), we can accurately find how the deep mixing rate varies with mass and composition.

The specific aim of this project is to constrain the deep mixing rate with respect to the mass and metallicity of the stars. To accomplish this we introduce a new process to estimate masses for stars without asteroseismic data. While our method is not accurate for stars with masses $M/M_{\odot} \geq 2.2$, it is accurate enough at low masses for the purposes of this project, where we focus on low mass stars and separate the data into broad mass and metallicity groups. The mixing rate will then be found for each selection of mass and metallicity, and can be compared to theoretical predictions. We also find the mixing rates for 6 globular clusters in APOGEE, and compare them to field stars.

The thesis is structured as follows: *Chapter 2* introduces the basic concepts needed to understand this project, including an overview of stellar structure and evolution, and outlining the basics of spectroscopy and asteroseismology. *Chapter 3* presents the previous work on deep mixing, including both observational analyses and theoretical modelling of mixing processes. *Chapter 4* outlines the two sources of raw data for this project, APOGEE and K2, as well as the reduction pipelines that we use to determine stellar properties for the surveys (ASPCAP and the APOKASC catalogue). We follow this with *Chapter 5* where we use the seismology data to predict the masses of stars without any seismology data. This section also discusses uncertainties in the models we used, and the overall accuracy of our methods. *Chapter 6* uses our mass predictions so we can begin to analyse the dependence of deep mixing on both mass and metallicity. This is followed by *Chapter 7*, where we discuss the results found in the previous chapter, and compare this to mixing rates in globular clusters in the APOGEE. We also compare our results to theoretical predictions and to results from the literature. Our conclusions are given in *Chapter 8*, while *Appendix A* provides additional figures and tables, and *Appendix B* provides some of the Python code used in this project.

CHAPTER 2

General Background

This chapter aims to ground the reader with some fundamental knowledge of stellar astrophysics, providing a brief outline of stellar structure, evolution and nucleosynthesis, as well as briefly summarising methods and theory behind two key observational techniques: spectroscopy and asteroseismology. An understanding of the theory behind stellar evolution is key to understanding the theoretical predictions for deep mixing, and an overview spectroscopy and asteroseismology are both necessary for the reader to understand the observational component of the project.

2.1 Stellar Structure and Evolution

This section will endeavour to outline the basic principles of stellar structure and evolution. We will begin by outlining the methods by which energy is transported within the stellar interior, and then define the nuclear fusion processes that supply this energy. We then conclude with a brief overview of the major stages of stellar evolution.

2.1.1 Energy Transport in Stellar Interiors

There are three ways energy is transported through the stellar interior: radiative transfer, conduction and convection (Clayton, 1968). Radiative transfer always needs to be considered in stellar interiors, as it is efficient in the core and inner layers of stars. Conduction is, in general, a much less efficient method of energy transport in most stellar environments (Carroll and Ostlie, 2006), and will not be covered here. Convection is the most important process of energy transfer to understand for this project as it plays a significant role in deep mixing.

Radiative Transfer

The basic idea of radiative transfer is very simple: photons emitted thermally in hot regions of stars and absorbed in cooler regions transport energy from the hot regions to the cold regions (Clayton, 1968). This process is then dependent on two main factors: the temperature gradient and the opacity of the star. Opacity is a measurement of how easily light can travel through a medium, and is related to the mean free path, which is the average distance a photon can travel before interacting with matter (Clayton, 1968). The transfer of radiation is then a slow process of photons being absorbed and re-emitted, inefficiently transporting energy towards the surface of the star. The radiative temperature gradient is (Carroll and Ostlie, 2006):

$$\frac{dT}{dr} = -\frac{3}{4ac} \frac{\bar{\kappa}\rho}{T^3} \frac{L_r}{4\pi r^2} \quad (2.1)$$

Where $\bar{\kappa}$ is the mean opacity, a is the radiation constant, c is the speed of light, ρ is the density, and L_r is the local radiative luminosity of the star at radius r .

Convection

Convection is the transportation of energy by the movement of hot material through its cool surroundings, typically taking the form of bubbles (Kippenhahn *et al.*, 2012). Convection occurs if the magnitude of the temperature gradient exceeds what is known as the “adiabatic temperature gradient”, which is given by:

$$\left. \frac{dT}{dr} \right|_{ad} = -\frac{g}{C_p} \quad (2.2)$$

where g is the gravitational acceleration at radial coordinate r , and C_p is the isobaric heat capacity. If the star’s temperature gradient is steeper than this quantity, then all of the energy in this region will be transported by convection, and convection will continue until the condition is broken, at which point the energy will be transported by radiation again (Carroll and Ostlie, 2006). Because convection moves material through the star, as well as energy, regions where convection occur tend to be homogeneous in composition, while radiative regions are not. Convection dominates the majority of the stellar atmosphere in red giants, while radiative transfer only occurs near the core and hydrogen burning shell (Iben, 1965).

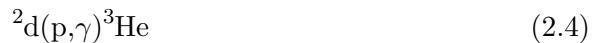
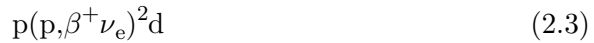
2.1.2 Stellar Nucleosynthesis

There are three main processes that generate energy inside a star, and which reaction is dominant depends on the mass, age and composition of the star

(Carroll and Ostlie, 2006). Here we will summarise the three process, as well as some variations to these processes, and highlight when they will be the dominant form of energy production.

The *p-p* Chain

The proton-proton chain (*p-p* chain) is the dominant form of energy production in young low-mass and low-metallicity stars. The net reaction is to convert $4 \text{ } ^1\text{H} \longrightarrow ^4\text{He} + 2\beta^+ + 2\nu_e$ (Clayton, 1968). The full process is as follows¹:



Where ^2d is an isotope of hydrogen called deuterium, and β^+ , ν_e and γ are a positron, electron neutrino and photon respectively. There are two other variations of the *p-p* Chain that exist, typically referred to as PPII and PPIII (The above reactions being PPI). The PPII chain requires a large concentration of both ^3He and ^4He as the probability of their fusion reaction is low (Clayton, 1968). The reactions are as follows:



and the PPIII chain has an even lower probability of occurring as ^7Be has a very short lifetime, so high temperatures are required to increase the probability of it interacting with a proton before decaying (Clayton, 1968). The PPIII chain is:



The CNO Bi-Cycle

The CNO (Carbon-Nitrogen-Oxygen) cycle converts four protons into a helium nucleus, using carbon, nitrogen and oxygen as catalysts. The cycle has

¹We will be using the standard notation for astrophysical nuclear synthesis, and not stoichiometric notation. The reaction $^2\text{d} + \text{p} \longrightarrow ^3\text{He} + \gamma$ will be written as $^2\text{d(p,}\gamma)^3\text{He}$

various forms, however we will only discuss 2 of these cycles as the others only occur in massive stars (Adelberger *et al.*, 2011). These two cycles work in tandem, and dominate energy production in intermediate-high mass, high metallicity stars (Carroll and Ostlie, 2006). The CNO-I cycle has a net process of $^{12}\text{C} + 4\text{H} \longrightarrow ^{12}\text{C} + ^4\text{He} + 2\beta^+ + 2\nu_e$ (Clayton, 1968). The full process is:



The CNO-II cycle starts with ^{14}N as the catalyst, and has a net reaction of $^{14}\text{N} + 4^1\text{H} \longrightarrow ^{14}\text{N} + ^4\text{He} + 2\beta^+ + 2\nu_e$. In the Sun reaction 2.17 only makes up 0.04% of total CNO reactions due to the low probability of the $^{15}\text{N} + \text{p}$ reaction resulting in ^{16}O instead of $^{12}\text{C} + ^4\text{He}$ (Clayton, 1968).



These two cycles work in tandem (hence it being known as the CNO bi-cycle), with the ^{14}N produced at the end of the CNO-II cycle being re-injected to the CNO-I cycle (Adelberger *et al.*, 2011), as seen in Figure 2.1.

Triple-alpha Process and Helium Burning

The Triple-Alpha process is comparatively a much simpler reaction than the *p-p* Chain and CNO Bi-Cycle. The net process is $3^4\text{He} \longrightarrow ^{12}\text{C}$, and the full form is:



The ^8Be nucleus is unstable, and will quickly decay back into two helium nuclei. However, if the helium abundance is high enough then another helium nucleus can interact with the ^8Be and can fuse into a stable ^{12}C nucleus (Clayton, 1968). The Triple-Alpha Process requires large concentrations of helium, and high pressure and temperature in order to occur

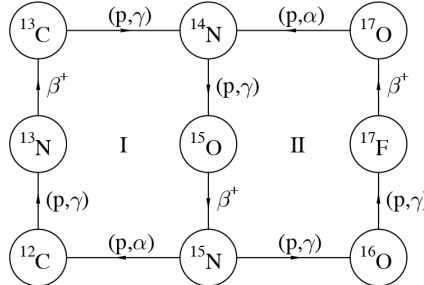
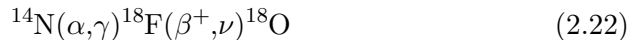


Figure 2.1: The CNO bi-cycle reactions demonstrating how the two cycles are linked by the same $^{14}\text{N}(\text{p},\gamma)^{15}\text{O}(\beta^+\nu_e)^{15}\text{N}$ reactions. The CNO-I and II cycles are marked I and II respectively. Figure is originally FIG 2. in Adelberger *et al.* (2011)

(Clayton, 1968). For this reason, only evolved stars in the RC, HB and AGB evolutionary stages burn helium in sufficient quantities (Carroll and Ostlie, 2006). In addition to the triple-alpha process, helium can also be depleted by the alpha-capture process once sufficient amounts of ^{12}C have been created. The three most common alpha-capture processes are (Iben, 1965):



This process of alpha-capture continues all the way to ^{56}Fe , after which photodisintegration destroys heavier nuclides (Kippenhahn *et al.*, 2012).

2.1.3 Stellar Evolution

In this section we will outline the evolution of a low mass star from the main sequence, along the red giant branch up to the point of the helium flash. We will also provide a brief overview of the horizontal branch, red clump and early asymptotic branch. The evolution of a $5M_\odot$ star from the main sequence to the asymptotic giant branch is plotted on an H-R diagram in Figure 2.2, with annotations for major evolutionary changes and times, and may serve as useful guide to aid the readers understanding of these processes. Evolutionary tracks for low mass stars from the main sequence to the tip of the red giant branch are plotted in Figures 2.3 and 2.4, with the evolutionary lifetimes presented in Table 2.1.

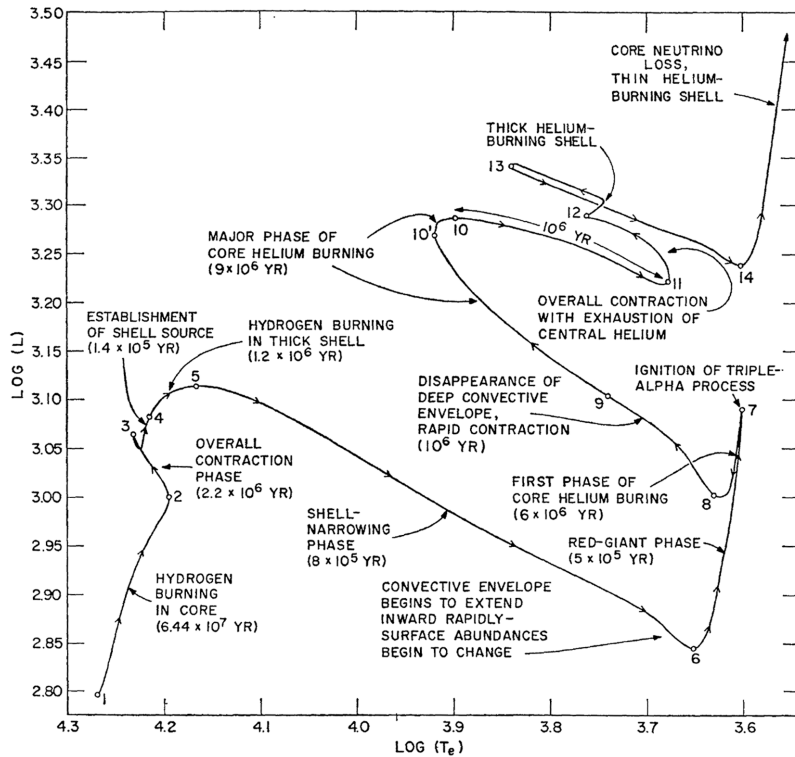


Figure 2.2: Evolution of the metal rich $5M_{\odot}$ star on a H-R diagram. Luminosity is in solar units, and temperature is in Kelvin. Times between points is given in years. Figure and caption from Iben (1967c).

Main Sequence

The main sequence (MS) is the period of a star's life when hydrogen fusion is occurring in the core, and where it spends the majority of its life (Carroll and Ostlie, 2006). For low-mass stars, the fusion processes are dominated by the p - p chain, with the CNO cycles only playing a minor role (Iben, 1967d). The time spent on the main sequence is determined primarily by the mass of the star, with high mass stars ageing off the main sequence more rapidly (Iben, 1967d). The lifetimes of the stars are presented in Table 2.1, with points 1 to 3 being the primary hydrogen burning phase on the main sequence, with a $1M_{\odot}$ star remaining on the MS for approximately 7 billion years (Carroll and Ostlie, 2006).

The structure of a MS star is mass dependent, with a low mass star ($M \leq 1M_{\odot}$) consisting of a radiative core where the p - p chain generates energy, with the CNO cycle operating inefficiently. It is also noteworthy that a considerable amount of ^{3}He is built up outside the core H-burning zone. This leads to the “ ^{3}He Problem”, where observations of the interstellar medium

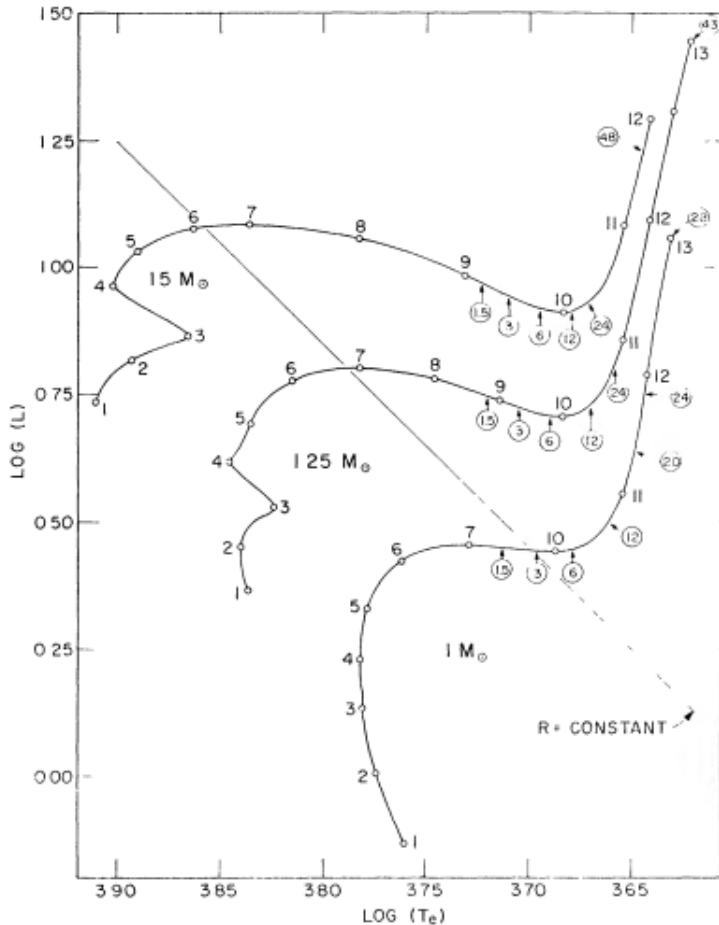


Figure 2.3: The evolutionary paths for Population I stars of mass $M/M_{\odot} = 1, 1.25$ and 1.5 . Times to reach labelled points along each track are given in Table 2.1. Luminosity L is in solar units and T_e is in Kelvin. Circled numbers represent the factors by which surface ^7Li abundance has been depleted relative to its main sequence value. The straight line is one of constant radius R . Figure and caption from Iben (1967d)

(ISM) yield lower abundances of ^3He than the models predict (Dearborn *et al.*, 1996). In the intermediate mass stars ($1.25 \leq M/M_{\odot} \leq 5$) the core becomes convective, due to the increase in internal energy production (Iben, 1967b).

Sub-Giant Branch

The main sequence ends with a phase of over-all contraction (points 3-4). The decreasing hydrogen abundance requires the core to contract and heat up to supply enough energy for the star to remain stable. Eventually the

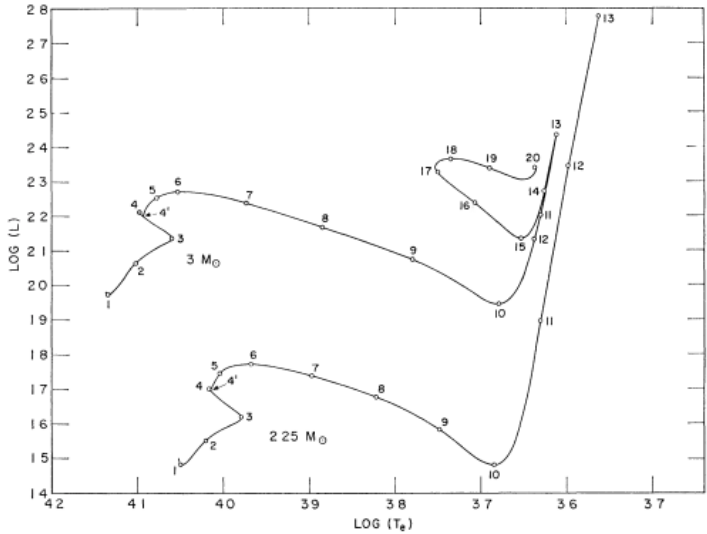


Figure 2.4: The evolutionary paths for Population I stars of mass $M/M_{\odot} = 2.25$ and 3 . Times to reach each labelled points along each track are given in Table 2.1. Luminosity L is in solar units and surface temperature T_e is in Kelvin. Figure and caption from Iben (1967b)

continuity between the contracting core and expanding envelope cannot be maintained, and the envelope will also contract and heat up. This simultaneously corresponds to the end of convection within the core, as the decrease in the temperature gradient no longer satisfies the condition for convection (Iben, 1965). This process does not occur for the $1M_{\odot}$ star, which does not have a convective core (Iben, 1967d). Once the core of the star is depleted of hydrogen, the star will move along the sub-giant branch (SGB), a transitional phase until the star reaches the red giant branch. This phase is points 4-10 on Figures 2.3 and 2.4, and overall sees a large decrease in the surface temperature of the star (Iben, 1967a).

On the SGB, hydrogen fusion occurs in a thick shell (H-burning shell) that surrounds the inert helium core. As the shell depletes its hydrogen, it will contract and heat up, while the envelope cools and expands to accommodate the increase in energy production. Eventually the helium core reaches the maximum mass that can support the envelope while remaining isothermal (Iben, 1965), and begins to contract. This mass is called the Schönberg-Chandrasekhar limit, and causes energy production rates decrease and the envelope to expand and cool rapidly (Schönberg and Chandrasekhar, 1942). This occurs at point 6 for the higher mass stars, which is where their luminosity decreases as they continue to cool. The lower mass stars have this phase occur at lower temperatures, closer to point 7, and the $1M_{\odot}$ star does not see a decrease in luminosity at this phase at all as

Point	$1M_{\odot}$	$1.25M_{\odot}$	$1.5M_{\odot}$	$2.25M_{\odot}$	$3M_{\odot}$
1	0.5060	0.2954	0.1821	0.058550	0.24586
2	38.209	14.220	10.277	2.7989	1.3892
3	67.100	28.320	15.710	4.8503	2.2367
4	81.719	30.144	16.520	5.0150	2.3409
4'	-	-	-	5.0174	2.3422
5	92.012	35.534	18.261	5.2018	2.4012
6	99.030	39.213	19.666	5.3847	2.4442
7	101.95	40.597	20.010	5.4460	2.4700
8	-	41.204	20.397	5.4737	2.4787
9	-	41.593	20.676	5.4947	2.4843
10	103.52	42.060	21.059	5.1571	2.4893
11	105.65	43.427	21.991	5.6167	2.4982
12	107.50	44.505	22.628	5.7774	2.5073
13	108.75	45.349	-	5.8986	2.5316

Table 2.1: Evolutionary Lifetimes (10^8 yr)

electrons become degenerate before the Schönberg-Chandrasekhar limit can be reached (Iben, 1967d).

Red Giant Branch

As the star approaches the minimum in luminosity (point 10), the temperatures are cool enough for hydrogen and helium in the envelope to recombine with electrons, which results in an increase in opacity. This results in the conditions for convection being met near the surface (Iben, 1965). In the radiative zone near the base of the envelope, the opacity decreases as electrons recombine with metals, and fewer H^- ions² can form. This results in an increase in luminosity to maintain a sufficiently high flux through the surface (Iben, 1965).

As the convective envelope continues to grow, it penetrates deep enough that it reaches regions where nuclear fusion has occurred during the MS phase. This leads to a surface abundances of elements changing, notably an increase in 3He , ^{13}C and ^{14}N , as well as a decrease in lithium and ^{12}C (Iben, 1967c). This process is called the “first dredge up” (FDU), and after FDU the surface abundances of RGB stars are not expected to change. At its deepest extent, the FDU leaves a discontinuity in chemical composition (μ -barrier), which inhibits further mixing Sweigart and Mengel (1979). As the H-burning expands it penetrates the μ -barrier, and the H-burning shell now starts to burn the hydrogen rich material above it (Kippenhahn *et al.*, 2012). This leads to a decrease in the luminosity, and increase in the surface

² H^- in the stellar atmosphere is a dominant supplier of opacity

temperature of the star. Once the discontinuity has been erased the star will continue to increase in luminosity (Christensen-Dalsgaard, 2015). This process was first observed in globular clusters as an overdensity of stars at a particular luminosity, and became known as the bump in the luminosity function (or RGB bump).

Horizontal Branch and the Red Clump

When the star reaches the highest point of the red giant branch (RGB tip, point 13 on Figures 2.3 and 2.4), core temperatures and densities become high enough to ignite the triple-alpha process (see *Section 2.1.2*). This causes the core to rapidly expand, which in turn causes the H-burning shell to cool, and energy production for the shell to decrease (Carroll and Ostlie, 2006). This leads to an overall decrease in luminosity and an increase in temperature as the star transitions onto the horizontal branch (HB, Iben 1965).

For low mass stars ($M < 1.8M_{\odot}$), the helium core at the RGB tip is dense enough that electron degeneracy prevents further contraction of the core, and cools due to neutrino loss. When the triple-alpha process begins, the energy generated initially goes into lifting the degeneracy in the core, after which helium fusion occurs at a rapid pace (Carroll and Ostlie, 2006). This is known as the “helium core flash”, and occurs so rapidly and explosively it is difficult to model the process (which is why Figures 2.3 and 2.4 stop at the RGB tip for the low mass stars).

After the RGB tip the core of the star is now converting helium into carbon, and the star proceeds along the horizontal branch (HB). As the core helium is depleted, the star moves towards higher temperatures, and slowly increases in luminosity (Carroll and Ostlie, 2006). This stage of core helium burning mimics the MS hydrogen burning phase. Stars that are low mass ($M < 1.8M_{\odot}$) and metal-rich tend to stay on the red end of the horizontal branch, forming what is known as the “red clump” (RC, Kippenhahn *et al.* 2012). The RC’s proximity to the RGB in temperature and luminosity makes the two types of stars difficult to differentiate by photometry and spectroscopy, but can be relatively easily differentiated by asteroseismology (Stello *et al.*, 2013; Elsworth *et al.*, 2017). Higher mass stars perform what is known as the “blue loop”, where they move to higher temperatures as they fuse helium in their cores. When the core is depleted of helium, the star cools and begins to burn helium in a thick shell around the inert CO-core, similar to the SGB stars and their H-burning shells (Iben, 1967c).

Early Asymptotic Giant Branch

Similar to how the HB resembles to the MS, the asymptotic giant branch (AGB) resembles the RGB. The stars again cool from the end of the HB

and asymptotically approach the RGB, and helium fusion takes place in a thin shell surrounding the CO core. Above the helium burning shell there is a layer of inert helium, and above that is the H-burning shell (Iben, 1965). The fusion layers are again surrounded by a convective envelope, which penetrates further into the depths of the star, eventually reaching the fusion processed material, bringing it to the surface in a process called the “second dredge-up” (Carroll and Ostlie, 2006). The upper portion of the AGB (called the thermal-pulse asymptotic giant branch, or TP-AGB) is outside the scope of this project, so we will end our discussion of stellar evolution here.

2.2 Spectroscopy

Spectroscopy is the process of studying the different wavelengths of light produced in a medium to determine properties of that matter. In a star the spectrum produced informs us of the composition of the surface of the star, as well as the temperature and gravity at the surface. While it is a powerful tool in astronomy, it can only tell us properties of the surface of the star. To gain insight on the interior of stars we need different tools, such as asteroseismology (see *Section 2.3*). This section will outline firstly how stellar parameters affect the stellar spectra, and then present on how stellar parameters are determined via spectroscopy.

2.2.1 Stellar Spectra

It is well known that stars radiate as blackbodies; however, the composition of the stellar atmosphere creates “absorption lines” in the stellar spectrum (Carroll and Ostlie, 2006). The absorption lines come from an atom (or molecule) absorbing a photon, which will move the atom into an excited state. The energy of the photon must exactly correspond to the energy required for the atom to move to the excited state, and since this energy is dependent on the properties of the atom (atomic number, atomic mass, ionisation level, and the type of transition), the frequencies which the atom absorbs are a unique “fingerprint” of each element (Carroll and Ostlie, 2006). The Balmer absorption lines in hydrogen are a well known example of stellar absorption lines, and each line corresponds to an electron moving to an excited state from the $n = 2$ state. These frequencies are exact and can easily be identified in a stellar atmosphere.

The stellar atmosphere’s temperature will change the relative strength of absorption lines, as electrons will tend to occupy higher energy states in high temperatures. Ionisation also changes the energy of an atom’s orbitals, and hence the spectral lines of the ion will change with the degree of ionisation. From statistical mechanics we know the the degree of ionisation and the probability of an atom occupying a certain energy level is temperature

dependent, so by measuring the absorption lines we can not only determine the composition of the stellar atmosphere, but also the temperature of the star's surface (Carroll and Ostlie, 2006).

In practice the lines are not infinitely narrow, but are broadened for a variety of reasons. Pressure broadening for example is caused by a collision between the absorbing atom and another nearby particle, which perturbs the energy levels and alters the frequency which will be absorbed (Gray, 1975). There will also be thermal broadening of lines, due to the Doppler effect. Similar broadening is observed in rotating stars, and is known as Doppler broadening (Gray, 1975). When discussing a star's spectral lines, we can learn a lot from a star due to the width of the absorption features, as well as the wavelengths.

2.2.2 Measuring Stellar Properties

As discussed above a variety of information is encoded in a star's spectra, and in this section we will outline the scale used for abundances, and the important stellar parameters that are determined from the spectra. Then we provide a brief discussion on how spectral lines are measured and converted into abundance calculations.

Determining Stellar Parameters

The abundances are typically measured on a logarithmic scale where the solar hydrogen abundance is defined to be $\log(\epsilon_H) = 12.0$, and other elements are defined as $A(X) = \log(\epsilon_X) = \log(N_X/N_H) + 12$, where N_X and N_H are the number density of the element X and hydrogen respectively (Asplund *et al.*, 2009). For other stars, we measure their abundances relative to the solar values, which we define to be:

$$[X/H] = \log\left(\frac{N_X}{N_H}\right)_* - \log\left(\frac{N_X}{N_H}\right)_\odot \quad (2.24)$$

where $*$ denotes the star's abundance, while \odot denotes the solar abundance. It is common to measure elemental abundance against iron, as it is typically representative of the overall metallic components of a star, and is easily measured from spectra (Carroll and Ostlie 2006, see Figure 2.6 for example spectra). The iron abundance ($[Fe/H]$) is referred to as the metallicity of the star, though sometimes total metallicity $[M/H]^3$ is used. The abundance ratio can be defined using logarithmic laws as:

$$[X/Fe] = [X/H] - [Fe/H] \quad (2.25)$$

³ $[M/H] = \log(Z/X)_* - \log(Z/X)_\odot$, where X=mass fraction of hydrogen, Z=mass fraction of all metals

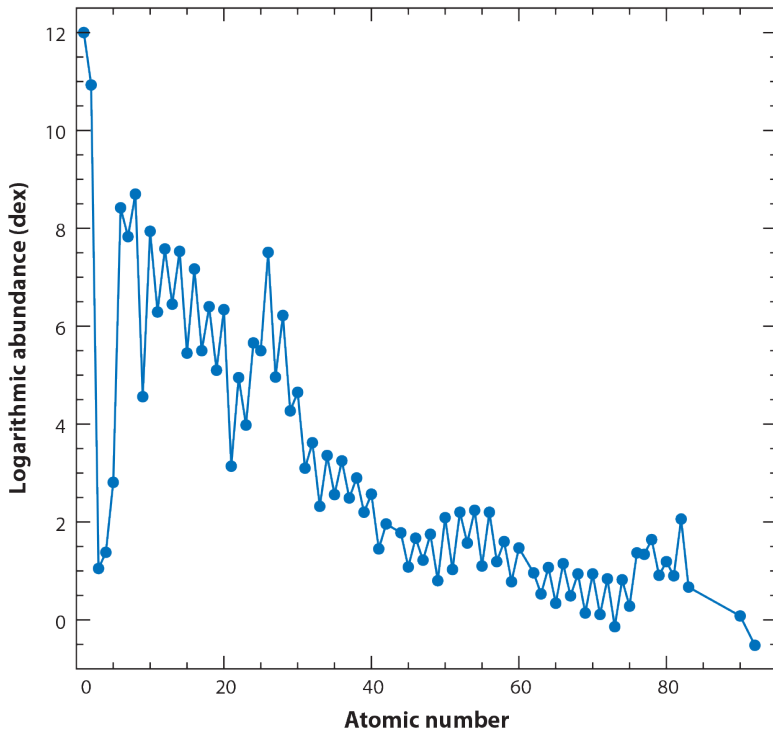


Figure 2.5: The present-day solar photospheric elemental abundances as a function of atomic number. As throughout this review, the logarithmic abundance of H is defined to be $\log(\epsilon_H) = 12.0$. Figure and caption from Asplund *et al.* (2009).

Before individual abundances can be determined, the stellar atmospheric parameters must first be found. These parameters include surface temperature (T_{eff}), surface gravity ($\log(g)$), metallicity ([Fe/H]) and the alpha abundance ([α /Fe]). These parameters are often determined by fitting the observed spectra to a synthetic spectrum from a model photosphere (see Majewski *et al.* (2017) for details on this process for the APOGEE project).

While it is obvious why knowing T_{eff} and $\log(g)$ is useful, the importance of metallicity and alpha abundance is less evident. The metallicity is a measure of how much metal⁴ is in a star. The metal content is important as it affects the opacity of the star, as well as the reaction rates of the CNO cycles, which will change the energy output of the star.

The alpha abundance is a measure of how much “alpha-process” elements are in a star. The alpha-process is a fusion reaction that occurs in the cores of massive stars, where an alpha particle fuses with another element (see *Section 2.1.2*). This is one of the primary methods where helium

⁴For astrophysicists any element more massive than helium is a metal.

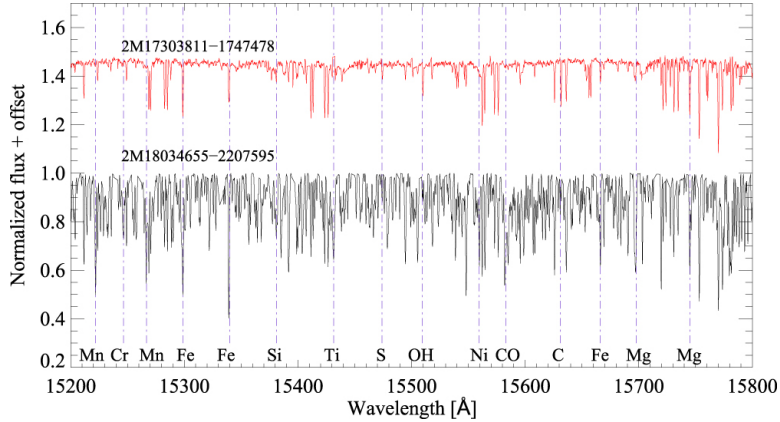


Figure 2.6: Comparison of a section of the APOGEE spectra for two stars with the same temperature (approximately 4060 K) with about a $100\times$ ratio in the abundance of iron. The red (top) spectrum is for a star that has $[\text{Fe}/\text{H}] = -1.68$ and $\log(g) = 0.40$. The black (bottom) spectrum is for a star that has $[\text{Fe}/\text{H}] = +0.28$ and $\log(g) = 1.39$ (SDSS DR12 values). Figure and caption from Majewski *et al.* (2017).

is fused into heavier elements (including ^{12}C , ^{16}O , ^{20}Ne , ^{24}Mg , ^{28}Si etc.). This process ends in ^{56}Ni , after which photodisintegration destroys heavier nuclides (Clayton, 1968). This process occurs rapidly in core-collapse (Type II) supernovae. Figure 2.5 depicts the abundances of elements in the solar photosphere. You can note the higher abundance of the alpha elements (even-numbered nuclides higher than ^{12}C), and a peak which corresponds to iron at atomic number 26, as ^{56}Ni decays into ^{56}Fe , which leads to an increase in the iron abundance in the star. The $[\alpha/\text{Fe}]$ abundance is then a comparison of how many elements were formed in Type II supernovae compared to synthesis occurring in Type Ia supernovae, which often produce Ti, V, Cr, Mn, Fe, Co and Ni (Clayton, 1968).

Measuring Spectral Lines

It is important to know the profile of the line, as well as its relative intensity. If we have a spectrum we can denote two different components for the feature: the continuum (given by F_c) and the line flux (F_ν). The continuum is the approximation of the blackbody radiation, and the line flux is the absorption or emission feature (Gray, 1975). We can define the line profile as:

$$R_\nu = \frac{F_c - F_\nu}{F_c} \quad (2.26)$$

The strength of the line is defined by the “equivalent width”, which is

defined as a rectangle with the height of the continuum emission, and a width such that it has the same total absorption as the real absorption line (Gray, 1975). It is defined as:

$$W = \int_0^{\infty} \frac{F_c - F_{\nu}}{F_c} d\nu \quad (2.27)$$

In practice these definitions are extremely simplified (Gray, 1975), but will suffice for our purposes. To determine abundances from equivalent widths we must combine the temperature, surface gravity and metallicity with atomic data such as energy levels and transition probabilities. Equivalent width can then be converted into abundances using a scaling relation called the “curve of growth”, which relates the equivalent width of the line to the column density of the stellar atmosphere (Gray, 1975). See Holtzman *et al.* (2015, 2018) for details on how abundances are calculated for APOGEE.

2.3 Asteroseismology

Asteroseismology is the process of measuring oscillations in the stellar surface to determine the internal structure of a star. The mass and radius of a star can also be determined by this method, making it a powerful tool for astronomy. Measuring these oscillations has, until recently, been extremely difficult and high-frequency asteroseismology could only be performed on the Sun. With new photometric surveys like *Kepler* and its successor, TESS, we can finally measure these oscillations for large numbers of stars

2.3.1 Stellar Oscillations and Asteroseismology

There are two different types of oscillations in stellar surfaces that we can detect, pressure waves (or p-modes) and gravity modes (g-modes) (Aerts *et al.*, 2010). The solutions for the displacement of the nodes of the oscillation, ξ , are given in the (r, θ, ϕ) directions as:

$$\xi_r(r, \theta, \phi, t) = a(r) Y_l^m(\theta, \phi) \exp(-i2\pi\nu t) \quad (2.28)$$

$$\xi_{\theta}(r, \theta, \phi, t) = b(r) \frac{\partial Y_l^m(\theta, \phi)}{\partial \phi} \exp(-i2\pi\nu t) \quad (2.29)$$

$$\xi_{\phi}(r, \theta, \phi, t) = \frac{b(r)}{\sin(\theta)} \frac{\partial Y_l^m(\theta, \phi)}{\partial \phi} \exp(-i2\pi\nu t) \quad (2.30)$$

Where $a(r)$ and $b(r)$ are the amplitudes of the oscillations, ν is the frequency of the oscillation and Y_l^m are spherical harmonics given by:

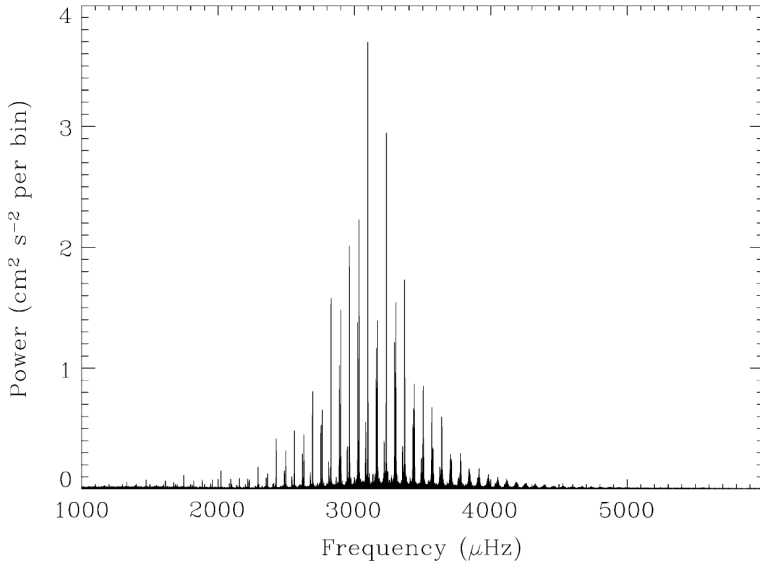


Figure 2.7: A power spectrum of radial velocity variations in the Sun seen as a star for 9.5 years of data taken with the Birmingham Solar Oscillation Network (BiSON) telescopes. The equivalent amplitude noise level in this diagram is 0.5 mm s^{-1} . Figure and caption from Aerts *et al.* (2010)

$$Y_l^m(\theta, \phi) = (-1)^m \sqrt{\frac{2l+1}{4\pi} \frac{(l-m)!}{(l+m)!}} P_l^m(\cos(\theta)) \exp(im\phi) \quad (2.31)$$

Where $P_l^m(\cos(\theta))$ are the Legendre polynomials. The higher degree modes of p-mode oscillations are not able to penetrate deeply into a star, but lower degree modes can, with the depth penetrated being dependent on the density of the star. By measuring the frequency of the mode on the surface, we can determine the internal pressure and temperature profile of the star. This requires us to fully resolve the surface of the star in order to see the modes of oscillation, so has primarily only been performed on the Sun (Aerts *et al.*, 2010).

Plotting the power spectrum of these oscillations gives us a “comb” of frequencies of alternating even and odd l -modes, as seen in Figure 2.7. The separation between the oscillations alone can tell us about the mass of the star, with low mass stars tending to have much larger frequency separations. Figure 2.8 displays the relation between the large and small frequency separations ($\Delta\nu$ and $\delta\nu$ respectively) and mass of low and intermediate mass stars. This type of plot is referred to as an asteroseismic H-R diagram.

Helioseismology⁵ has the capacity to inform us of much of the internal structure of the Sun, mostly due to its proximity to us. Applying these

⁵Asteroseismology is called helioseismology when applied to the Sun

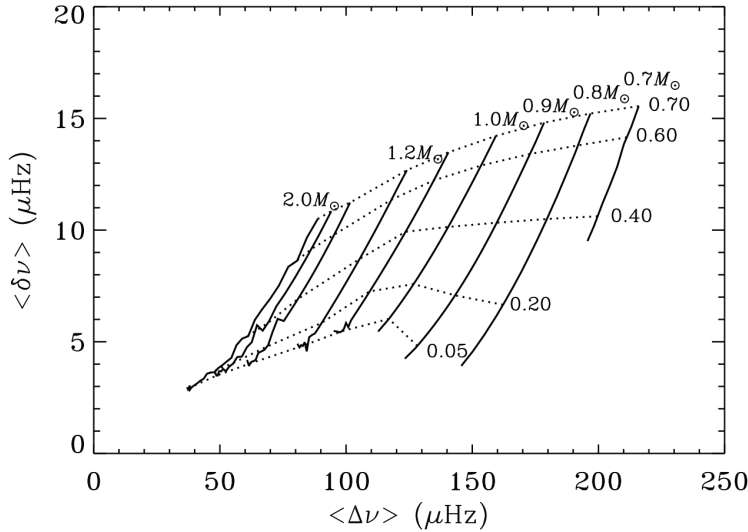


Figure 2.8: An asteroseismic HR Diagram in which the large separation $\Delta\nu$ is most sensitive to mass, and the small separation $\delta\nu$ is most sensitive to age. The solid, nearly vertical lines are lines of constant mass, and the nearly horizontal dashed lines are isopleths of constant hydrogen mass fraction in the core, at the values indicated in the figure. Figure and caption from Aerts *et al.* (2010)

techniques to learn about other stars is not an easy accomplishment as asteroseismology requires long, consistent observing times, which often are difficult to obtain due to the Earth's orbit around the Sun, and allocation of observing time (Christensen-Dalsgaard, 2002).

2.3.2 Scaling Relations

Due to the lack of knowledge of the amplitude of solar-like oscillations in stars, Kjeldsen and Bedding (1995) developed scaling relations (equations 2.32 and 2.33) to predict the frequency of maximum power (ν_{\max}) and the large frequency separation ($\Delta\nu$) of the oscillations as a function of the mass, radius and temperature of the star, using the Sun's values as a basis. Figure 2.9 depicts the power spectrum of the solar-like oscillations, with $\Delta\nu$, ν_{\max} and n_{\max} labelled.

$$f_{\nu_{\max}} \left(\frac{\nu_{\max}}{\nu_{\max,\odot}} \right) = \frac{M/M_{\odot}}{(R/R_{\odot})^2 \sqrt{T_{\text{eff}}/T_{\text{eff},\odot}}} \quad (2.32)$$

$$f_{\Delta\nu} \left(\frac{\Delta\nu}{\Delta\nu_{\odot}} \right) = \left(\frac{M/M_{\odot}}{(R/R_{\odot})^3} \right)^{\frac{1}{2}} \quad (2.33)$$

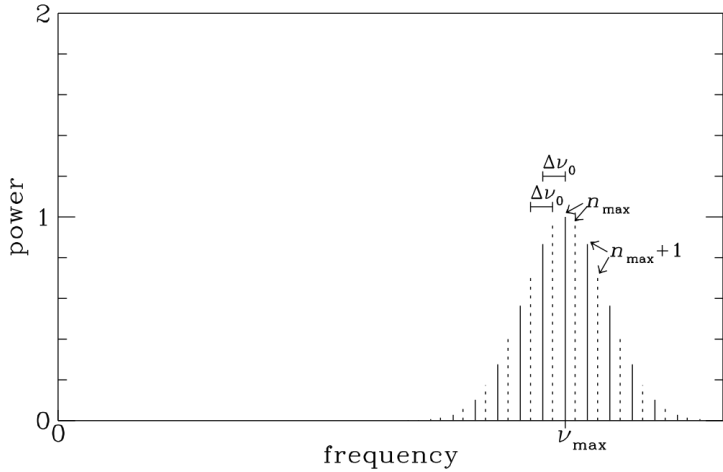


Figure 2.9: Schematic diagram of the power spectrum of solar oscillations. Each peak corresponds to an oscillation mode: solid peaks are $l = 0$ modes and dashed peaks are $l = 1$. Figure and caption from Kjeldsen and Bedding (1995)

where $T_{\text{eff},\odot} = 5777 \text{ K}$, $\nu_{\text{max},\odot} = 3.05 \text{ mHz}$ and $\Delta\nu_{\odot} = 134.9 \mu\text{Hz}$. The scaling factors $f_{\nu_{\text{max}}}$ and $f_{\Delta\nu}$ are usually set to 1. These can be rearranged to give estimates of mass and radius of the stars:

$$\frac{M_{sc}}{M_{\odot}} = \left(\frac{T_{\text{eff}}}{T_{\text{eff},\odot}} \right)^{\frac{3}{2}} \left(\frac{\nu_{\text{max}}}{\nu_{\text{max},\odot}} \right)^3 \left(\frac{\Delta\nu}{\Delta\nu_{\odot}} \right)^{-4} \quad (2.34)$$

$$\frac{R_{sc}}{R_{\odot}} = \left(\frac{T_{\text{eff}}}{T_{\text{eff},\odot}} \right)^{\frac{1}{2}} \left(\frac{\nu_{\text{max}}}{\nu_{\text{max},\odot}} \right) \left(\frac{\Delta\nu}{\Delta\nu_{\odot}} \right)^{-2} \quad (2.35)$$

Stello *et al.* (2009) also investigated the relation between $\Delta\nu$ and ν_{max} , and found that:

$$\frac{\Delta\nu}{\Delta\nu_{\odot}} \approx \left[\frac{(M/M_{\odot})^{-0.27} (T_{\text{eff}}/T_{\text{eff},\odot})^{0.305}}{(L/L_{\odot})^{-0.02}} \right] \left(\frac{\nu_{\text{max}}}{\nu_{\text{max},\odot}} \right)^{0.77} \quad (2.36)$$

The implication of this relation is that only either ν_{max} or $\Delta\nu$ must be known, and the other can then be predicted using other known stellar quantities. With these scaling relations the mass and radius of stars can be determined. Often this process will be streamlined into a pipeline that utilises grid-based modelling which will compare ν_{max} , $\Delta\nu$ and other observable parameters to synthetic models to predict the mass, radius, surface gravity and age of the star.

CHAPTER 3

Deep Mixing on the RGB

This section will be split into two subsections: one outlining a brief history of previous observations of an extra-mixing process occurring in the RGB, and the second detailing theories that explain this mixing, with particular emphasis on “thermohaline mixing”, which is currently the most accepted model of deep mixing.

3.1 Observational Evidence of Deep Mixing on the RGB

Carbon depletion in giant stars was first observed in globular clusters in what was known as “weak G-band stars” in the 1970s (Zinn, 1973). Since then numerous spectroscopic surveys looking at both globular cluster and field stars have been performed.

3.1.1 Weak G-Band Stars and Early Observations

While examining the spectra of 20 giants in the globular cluster M92, Zinn (1973) noted that six of the stars have unusually weak G-bands in their spectra, which is the band of the CH molecule at $\lambda \approx 4300 \text{ \AA}$. This observation is one of the first that indicates that there is an unknown process that removes carbon from a star’s photosphere. Analysis of these stars indicated that these stars were likely asymptotic giant branch (AGB) stars, and the red giant branch (RGB) stars in M92 have normal G-bands. Examination of the normal G-band stars indicated that this was also not an effect of differences in surface temperature or gravity, which suggested that it is likely an evolutionary event that is responsible. Zinn (1973) suggested that depletion

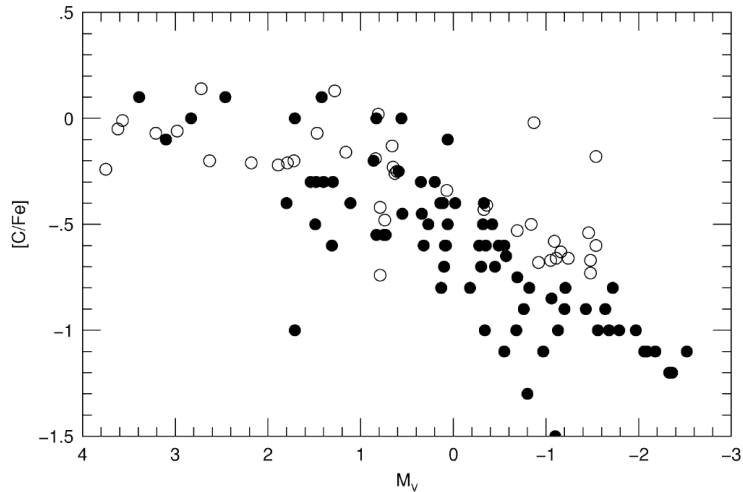


Figure 3.1: Carbon abundance $[C/Fe]$ as a function of absolute magnitude for field giants from Gratton *et al.* (2000) (open circles) and M92 giants (filled circles). Figure from Smith and Martell (2003).

of the surface carbon abundance is the most likely explanation for the weak G-bands, and proposed that mixing between the convective surface and radiative hydrogen burning shell at some point in the blue horizontal branch would deplete the carbon.

Carbon *et al.* (1982) re-examined M92 nearly 10 years later in another spectroscopic survey. Carbon's goal was to determine both carbon and nitrogen abundances to a) verify Zinn's previous observations and b) find out if the carbon is being processed into nitrogen via the CN-cycle. While they were able to demonstrate that the carbon abundances in AGB stars are on average 10 times smaller than RGB stars with the similar T_{eff} and surface gravity, Carbon also found that there was no clear anti-correlation between C and N in any of the stars surveyed, and the average nitrogen abundances, while enhanced ($\langle [N/Fe] \rangle = 0.65$), were the same in both AGB and SGB stars.

This work was continued in Langer *et al.* (1986), who observed fainter, less evolved stars on the SGB in M92. Langer concludes that the fainter less evolved stars have on average a higher carbon abundance than the brighter, more evolved stars. This supports the hypothesis that a previously unknown mixing mechanism is adding CN processed material from the H-burning shell to the convective surface.

3.1.2 Modern Survey Projects

In the 2000s the observations began to move away from globular clusters to field stars, with Gratton *et al.* (2000) being one of the first to analyse these stars. Gratton analysed the abundances for Li, C, N, O, Na and the $^{12}\text{C}/^{13}\text{C}$ ratios for field stars believed to be in four different phases of stellar evolution: main-sequence turn-off for primordial [C/N] ratio, lower red giant branch for FDU abundances, upper red giant branch for abundance changes from the unknown mixing process and red horizontal branch for the post-helium flash abundances. The stars were selected to be within the range of $-2.0 < [\text{Fe}/\text{H}] < -1.0$, to ensure they were within the metallicity range where the extra-mixing had been previously observed in globular clusters. Gratton observed that the extra-mixing responsible for carbon depletion appeared to be metallicity dependent, reaching a maximum at $[\text{Fe}/\text{H}] \approx -1.5$. At lower metallicity there was a large scatter in [C/Fe] after the RGB bump; however, they were unable to determine if this is due to scatter in the initial elemental abundances, or some other factor which is modulating the mixing.

Data from Gratton *et al.* (2000) was also used in Smith and Martell (2003), who compared mixing in field giants to globular clusters of similar metallicity. The globular clusters include the previously mentioned M92, as well as NGC 6397, M3 and M13. This comparison is significant as it can tell us several things about the mixing process: 1) Is the mixing dependent on metallicity? 2) Is the mixing mass dependent? 3) Does the mixing occur to the same extent in all stars, or is it stronger in Population II¹ stars? Smith found that field stars of similar metallicity depleted carbon at similar rates, but only for stars brighter than the bump in the luminosity function (see Figure 3.1). However due to the small sample size and potential primordial enrichment of globular clusters, no strong conclusions could be made about the strength of the metallicity dependence, or whether there is a mass dependence for the mixing.

Along with carbon and nitrogen, lithium is one of the key indicators of the extra mixing process (Charbonnel *et al.*, 1998), with lithium abundances observed to decrease. This is likely due to primordial lithium in the envelope being mixed into the hotter radiative zone of the star, where it is destroyed (Charbonnel and Zahn, 2007). Figure 3.2 compares a colour-magnitude diagram of globular cluster NGC 6397 to the lithium abundances against absolute magnitude, which nicely compares the lithium abundance to the evolutionary phase of the star (Lind *et al.*, 2009). The points of inflection in A(Li) are at FDU and the onset of deep mixing, which also correspond to the beginning of the RGB, and the luminosity bump.

Possibly the largest project investigating the extra-mixing phenomenol-

¹Population II stars are metal poor stars found in the Galaxy's halo, typically in globular clusters

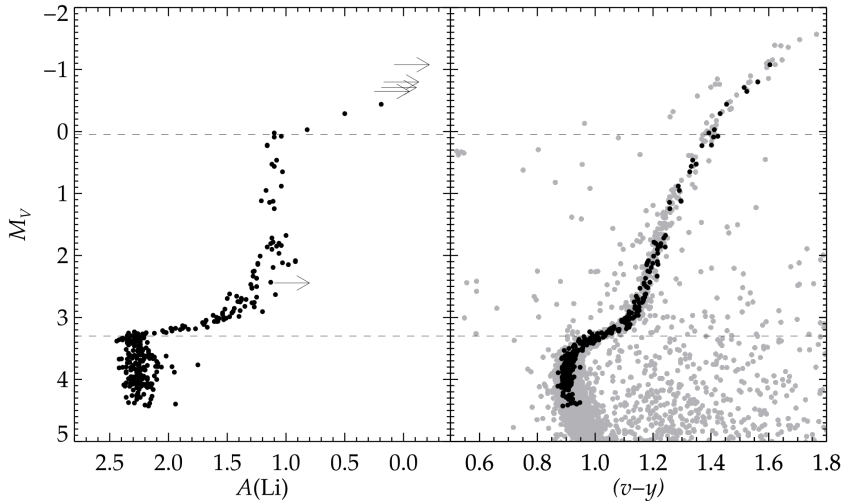


Figure 3.2: **Left:** Non-LTE Li abundances inferred for our sample are plotted against absolute absolute visual magnitude. Arrows mark Li upper limits. **Right:** the spectroscopic targets marked with black filled circles in the colour-magnitude diagram of NGC 6397. The two horizontal dashed lines mark the locations of rapid decrease in Li abundance caused by FDU ($M_V \approx 3.3$) and the onset of deep mixing ($M_V \approx 0.0$). Figure from Lind *et al.* (2009).

ogy is Shetrone *et al.* (2019). Shetrone uses APOGEE data (see *Section 4.1*) to obtain carbon and nitrogen abundances for approximately 20,000 RGB stars and 5000 RC stars. To select lower mass stars they implemented a cutoff in the alpha abundance, with any stars with $[\alpha/\text{Fe}] > 0.14$ considered to be a low mass star ($M < 1.2M_\odot$). The quality of this selection will be discussed in this project, as it can lead to contamination by some high mass stars. Additionally the selection removes a substantial number of low mass stars with low alpha abundances.

Since Shetrone was working with field giants whose absolute magnitude was unknown, the mixing is instead described as a function of the surface gravity $\log g$, which can be determined spectroscopically. The [C/N] ratio is plotted as a function of $\log g$ in Figure 3.3 for 10 different selections of metallicity. This plot also indicates the mean surface gravities where first dredge up (magenta arrow) and the extra mixing process (green arrow) occur for each metallicity selection. Red Clump stars are also plotted separately from the RGB stars. What is clear from this plot is the metallicity dependence of the extra-mixing in these stars, being strongest in low metallicity stars, with a maximum depletion in the [C/N] ratio of 0.58 dex. We also observe significant scatter in the most metal poor stars ($[\text{Fe}/\text{H}] < -1.5$).

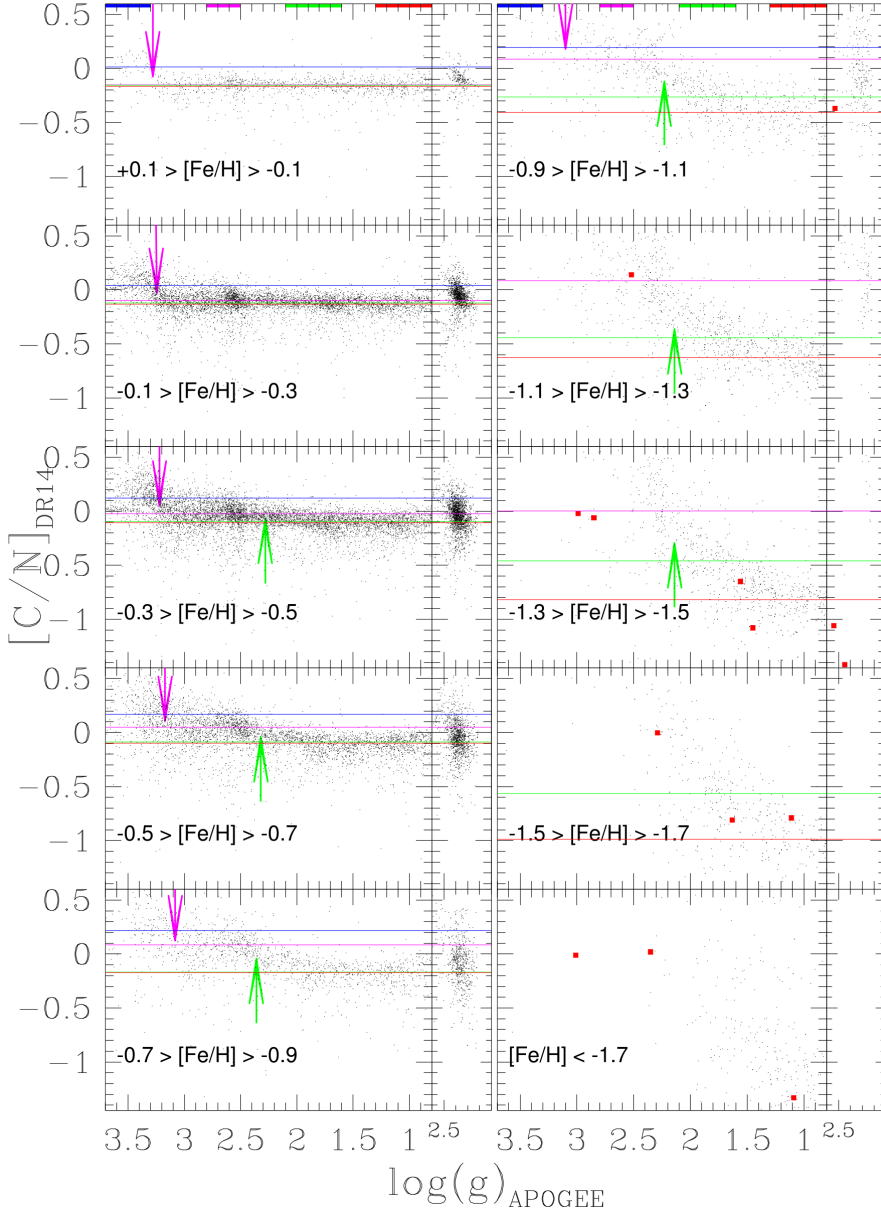


Figure 3.3: $[C/N]$ ratios for the RGB (left panels) and the Red Clump (RC, smaller right panels) from Shetrone *et al.* (2019) as a function of $\log g$. Each row is a sub-sample based on a range in $[Fe/H]$ as listed on the figure. The magenta and green arrows show the mid-point of the first dredge-up and onset of extra-mixing respectively. Medians are calculated for the regions with luminosities below first dredge-up (blue), above first dredge-up (magenta), above the bump in the luminosity function (green) and higher on the RGB (red). The red points represent literature $[C/N]$ values taken from Gratton *et al.* (2000). Figure taken from Shetrone *et al.* (2019).

3.2 Mixing Models

Now that we have outlined the observations that tell us that the stars are undergoing some form of mixing, we must address the next question: why? Here we will outline three potential mechanisms which either individually or together may be responsible for the observed change in abundances.

3.2.1 Rotational Mixing

Rotation was one of the first explanations proposed for the strange abundance patterns observed on the RGB. Sweigart and Mengel (1979) proposed the idea that meridional circulation created from a rotating core in RGB stars could induce a mixing mechanism, and bring CN-processed materials from the H-burning shell to the surface of the star. This process is inhibited by a mean molecular weight gradient (μ -gradient) in the radiative zone of the star on the lower giant branch, which is destroyed at the RGB bump. Sweigart and Mengel conclude that the mixing does provide a reasonable explanation for the depletion of carbon, and suspect that at low metallicities, the mixing extent is able to penetrate further into the H-burning shell, possibly far enough to bring ON-processed material to the surface.

However, interior rotation of stars is difficult to determine, and more recent works (see Charbonnel and Palacios 2004 and references therein) suggest that meridional circulation alone is not enough to explain the abundances observed in evolved RGB stars. Chanamé *et al.* (2005) compared their recent evolutionary model which considered internal rotation to abundance data from globular clusters, and proposed a model in which the mixing was driven by the energy (luminosity) of the star, which explains why the mixed stars are only seen on the upper-RGB, where the stars are brighter. This is contrary to the “ μ -gradient” theory that others had proposed to inhibit the mixing. They also predict that the mixing would primarily be dependent on the initial rotation rate, and secondarily be affected by mass and metallicity, with low mass and low metallicity stars having the strongest mixing, which matches observations.

3.2.2 Magnetic Mixing

Another early theory to explain the deep mixing phenomenon was that it was driven by internal magnetic fields. Hubbard and Dearborn (1980) presented a theory where “magnetic flux tubes” form at the boundary of the core convection zone of main sequence stars. The magnetic field in these tubes exerts an additional pressure on the material inside it, which tends to make it buoyant. If we assume that the plasma that makes up the inside of the star is highly conductive, then the material will be bound onto the magnetic field lines and transported up, and be mixed into the outer regions of the

star. This would only occur in stars with masses $1.5M_{\odot} \leq M \leq 5M_{\odot}$, as lower mass stars don't have a convective core, and in higher mass stars the mixing time scale will be longer than the MS lifetime.

Busso *et al.* (2007) proposed that a similar process could occur in RGB and AGB stars, and be the mixing process which was linked to the unusual RGB abundances. Using phenomenological arguments they conclude that this magnetic mixing mechanism is plausible, but requires very high internal magnetic fields for AGB stars that have been extensively mixed. Nordhaus *et al.* (2008) showed that an α - Ω dynamo operating in the interior of an RGB star could supply the field strength necessary to mix material to the surface, but note that further work is needed in studying the relation between convection and the magnetic mixing, and they emphasise that 3D hydrodynamic simulations are required to further support this theory. Further work by Palmerini *et al.* (2009) showed that this form of mixing was also metallicity dependant, supporting the idea that this could be responsible for deep mixing. Their models also found that it could produce lithium abundances that correlate to the observed patterns in globular clusters, which many other models struggle to do (Lind *et al.*, 2010).

3.2.3 Thermohaline Mixing

Thermohaline mixing is widely considered the most likely mechanism which produces the observed abundance patterns. This mechanism, first suggested by Eggleton *et al.* (2006) and refined by Charbonnel and Zahn (2007) is produced by an inversion in the mean molecular weight created by the $^3\text{He}(^3\text{He}, 2\text{p})^4\text{He}$ reaction, which causes mixing between the radiative zone just above the H-burning shell and the convective surface. This was noticed by Dearborn *et al.* (2006) after completing 3D hydrodynamical simulations of low mass red giants. The retreating of the convective zone after the RGB bump leaves an abundance of ^3He . This forms a small ^3He burning shell just above the hydrogen burning shell, and this results in a small inversion in the mean molecular weight (Eggleton *et al.*, 2007). This simultaneously provides a mechanism to explain the extra-mixing on the RGB while also explaining why there is not an overabundance of ^3He , which previous models of stellar evolution had predicted, despite observations to the contrary (Eggleton *et al.*, 2006).

This inversion, though quite small and often ignored in previous 1D stellar models (Eggleton *et al.*, 2007), is enough to create a “double diffusive instability”, which can result in what is known as “thermohaline convection” (Charbonnel and Zahn, 2007). This kind of mixing was first characterised by Stern (1960) who described it in the context of stratification of salinity and temperature in oceans, and was applied to a stellar context by Ulrich (1972), but in a different context to what is discussed here. The instability can best be described using the common oceanographic case: warm water with a high

salt content lies on top of cold, fresh water. The warm water is denser due to the salt content, but the stratification is stable due to the temperature difference. The future instability of the system is then dependent on two processes, the time for the (stabilising) heat to diffuse into the cold water, and the time for the (destabilising) salt to diffuse (hence this being referred to as a “doubly diffusive instability”). In the oceanographic case the heat diffuses much more quickly, creating dense regions that descend through the cool water without exchanging salt content with their surroundings. This creates a “salt finger” which will eventually transport salt into the fresh water, while reciprocal fresh-water “fingers” ascend and take their place (Angelou *et al.*, 2011).

In our stars, the salt is replaced by a decrease in the mean molecular weight from the $^3\text{He}(^3\text{He},2\text{p})^4\text{He}$ reaction. The reaction is exothermic and its products have a lower mean molecular weight than their surroundings, so a parcel of hot material will form. This will rapidly expand and cool to reach pressure equilibrium with its surroundings, but is now less dense than the surrounding material, so will begin to rise, creating an upflow of material from the H-burning shell. Simultaneously, material from the envelope will be mixed into the H-burning shell, where any excess ^3He will undergo fusion reactions. This has a net effect of decreasing the amount of ^3He and ^{12}C in the surface, as well as transporting ^{13}C and ^{14}N to the surface. Since the thermohaline instability is rather weak, we only see mixing in homogenised regions, such as the region left behind from FDU (Iben, 1967c). To be more specific, FDU leaves a homogenised region in the radiative region of a star, but further mixing is inhibited by the discontinuity in molecular weight (μ -barrier) at this point. When the H-burning shell reaches this point at the RGB bump, the μ -barrier is erased and mixing can now occur. Angelou *et al.* (2011) provides a succinct, detailed description of this process.

While this mechanism has been identified as a likely candidate to explain the extra-mixing, the extent of the mixing has been much debated, and numerous simulations have been used to try to estimate the extent of the mixing. Denissenkov (2010) used 2D simulations to determine the effective ratio of a salt finger’s length to its width, α . This parameter determines the efficiency of the mixing, therefore an accurate knowledge of its value is key to understanding if the thermohaline instability is responsible for the deep mixing. Ulrich (1972) suggested that $\alpha \approx 5$ based on their simulations, a number Charbonnel and Zahn (2007) agrees with as it closely reproduces the change in abundances. Denissenkov (2010), however, finds that in their simulations $\alpha < 1$ for the RGB case, and the thermohaline instability is unable to cause sufficient mixing to explain the observed change in abundances. However, they also note that if the mixing ratio is set to $\alpha \approx 7$ the simulations are able to reproduce observations almost exactly. A follow up 3D simulation was completed a year later and described in Denissenkov and Merryfield (2011), confirming that the mixing ratio predicted by the

simulations is about 50 times lower than required to reproduce observations. Denissenkov (2012) states that while thermohaline mixing alone may not explain the mixing phenomenon, a combination of thermohaline mixing, rotation and gravity waves may be sufficient to explain the abundance patterns.

Conversely, Charbonnel and Lagarde (2010) found using their evolutionary models that thermohaline mixing accounts for the observed behaviour of the abundances on RGB, and rotation-induced mixing can account for star-to-star variations. The models used are computed with the STAREVOL code (Siess *et al.*, 2000; Palacios *et al.*, 2003, 2006; Decressin *et al.*, 2009) at solar metallicity for stars with initial masses between 1 and $4M_{\odot}$. The abundances for [C/Fe] and [N/Fe] both before and after the onset of mixing are provided in Table 3.1. This table is a condensed version of the table that appears in Charbonnel and Lagarde (2010), which includes more predictions at different masses, as well as more parameters. We note that with increasing mass, higher rotational velocities (V_{ZAMS}) are required to produce similar mixing rates to the low mass case. It is also noteworthy that the intermediate mass stars ($M \geq 2.0M_{\odot}$) tend to have lower [C/Fe] and higher [N/Fe] due to the FDU being stronger. The follow up papers, Lagarde *et al.* (2011, 2012), compute the models for both varying masses and metallicities, and examine thermohaline mixing's role in destroying ^3He . In all papers the mixing ratio α is chosen to be 5, as it had previously been shown to reproduce observations. They also note that modelling the stellar interior accurately is difficult so the simulations performed by Denissenkov do not necessarily reflect reality.

Lagarde *et al.* (2019) constructed synthetic stellar populations using their model of thermohaline mixing, and compared them to C and N abundances determined using the UVES spectrograph in the Gaia-ESO survey (Gilmore *et al.*, 2012) to test thermohaline mixing on a larger scale. Figure 3.4 depicts how the [C/N] abundance is predicted to change at different stages of stellar evolution in models with and without thermohaline mixing. Figure 3.5 compares the two synthetic populations with Gaia-ESO data. Lagarde *et al.* (2019) claims that the thermohaline models fit well with the observed data, but again provide no further evidence that their chosen mixing length is correct.

Thermohaline mixing was again verified to reproduce observations in Angelou *et al.* (2011), where they used the stellar evolution code MONSTAR (see Campbell and Lattanzio 2008 for details on the evolutionary code) to compare the theories to observations in the globular cluster M3. Testing both different mixing ratios, as well as the non-diffusive model Eggleton *et al.* (2008) proposed called “ $\delta\mu$ -mixing”. The comparison finds that it is indeed the diffusive model with a large mixing ratio ($\alpha = 6$) that best matches M3. A follow up paper (Angelou *et al.*, 2012) investigated other globular clusters to see if their model is able to match their abundance

Mass (M_{\odot})	Mixing	V_{ZAMS} (km s $^{-1}$)	FDU		RGBt		$\Delta[\text{C}/\text{Fe}]$	$\Delta[\text{N}/\text{Fe}]$
			[C/Fe]	[N/Fe]	[C/Fe]	[N/Fe]		
1	st	0	-0.05	0.16	-0.05	0.16	0.00	0.00
	th	0	-0.05	0.16	-0.09	0.25	-0.04	+0.09
	th+rot	50	-0.10	0.27	-0.10	0.27	0.00	0.00
1.25	th	0	-0.10	0.37	-0.12	0.31	-0.02	-0.06
	th+rot	80	-0.12	0.39	-0.14	0.34	-0.02	-0.05
	th+rot	110	-0.13	0.31	-0.15	0.35	-0.02	+0.04
1.5	st	0	-0.14	0.33	-0.14	0.33	0.00	0.00
	th	0	-0.14	0.33	-0.15	0.34	-0.01	+0.01
	th+rot	110	-0.16	0.36	-0.18	0.38	-0.02	+0.02
2.0	st	0	-0.19	0.39	-0.19	0.39	0.00	0.00
	th	0	-0.19	0.40	-0.19	0.39	0.00	0.00
	th+rot	110	-0.22	0.47	-0.22	0.47	0.00	0.00
	th+rot	180	-0.23	0.47	-0.23	0.48	0.00	+0.01
2.5	st	0	-0.19	0.45	-0.19	0.45	0.00	0.00
	th	0	-0.19	0.45	-0.19	0.45	0.00	0.00
	th+rot	300	-0.53	0.55	-0.53	0.82	0.00	+0.22

Table 3.1: [C/Fe] and [N/Fe] abundances predicted in Charbonnel and Lagarde (2010) at the end of first dredge up (FDU) and the tip of the red giant branch (RGBt) for stars with solar metallicity modelled with no extra mixing (st), thermohaline mixing (th) and a combination of thermohaline and rotation induced mixing (th+rot). In this last model the rotational velocity of the star (V_{ZAMS}) as a zero-age main sequence (ZAMS) star is provided. See text for further details.

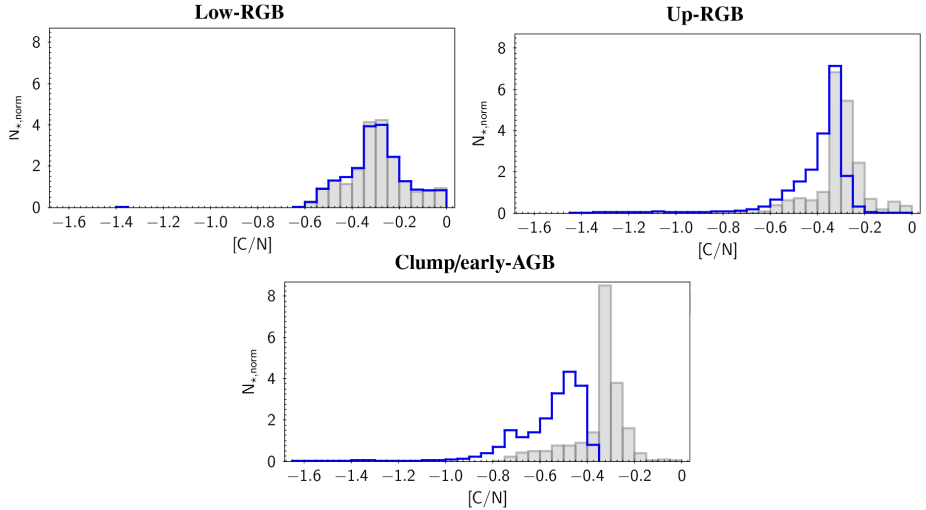


Figure 3.4: [C/N] ratios normalised to the histogram area for synthetic stellar populations produced in Lagarde *et al.* (2019). The blue histogram includes thermohaline mixing, while the grey is without. Stars are divided into three groups: low-RGB (before the RGB bump, top panel), upper-RGB (after the RGB bump, middle panel) and red clump/early AGB stars (bottom panel). Figure and caption from Lagarde *et al.* (2019).

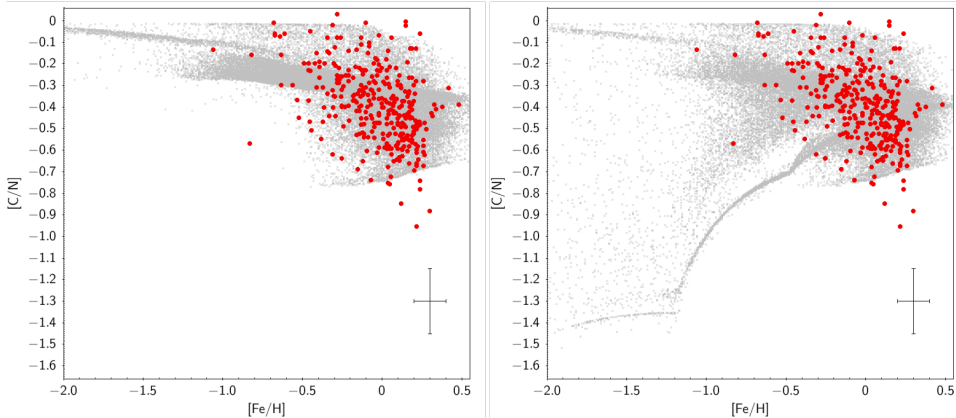


Figure 3.5: $[C/N]$ as a function of $[Fe/H]$ for synthetic populations computed in Lagarde *et al.* (2019) with the effects of thermohaline instability (right panel) and without (left panel). The $[C/N]$ values for our sample of UVES giant field stars are also shown (red dots). Figure and caption from Lagarde *et al.* (2019).

patterns. While the model matches the clusters M3, M13 and NGC 5466 well, it is unable to model the mixing in M92 and M15. They assert that either the mixing appears to begin before the RGB bump, or the first dredge up reaches a deeper extent than predicted.

Henkel *et al.* (2017) also used the MONSTAR stellar evolution code, in this case to determine if a modified version of thermohaline mixing can simultaneously fit carbon and lithium abundances to globular cluster NGC 6397, which previous models had failed to do. The most successful variation they found was by adding a temperature dependence to the thermohaline mixing rate. This has the effect of more rapid mixing at the base of the thermohaline region, and slower mixing at the base of the convective envelope. This increases the lithium abundance by mixing more beryllium out of the H-burning shell and into the envelope, where it captures an electron and forms lithium. Henkel *et al.* (2018) continues this work by developing further models for extremely metal poor stars ($[Fe/H] \approx -3.0$). These models fit well, but they note that more data for metal poor stars is required to gain insight into this problem. It should also be stressed that this solution is entirely phenomenologically driven, and currently has no underlying physics supporting it. Furthermore it does not address the issue of the mixing ratio that we discussed earlier, and indicates that both more theoretical and observational work is required to fully understand this phenomenon.

CHAPTER 4

Data Sources

For this project we will be sourcing our data from the APOGEE survey Majewski *et al.* (2017) and the Second APOKASC Catalogue (Pinsonneault *et al.*, 2018). This catalogue combines spectroscopic parameters from the APOGEE with asteroseismic data from the Kepler Survey (Borucki *et al.*, 2010). The combination of abundance data with masses, radii and ages derived from asteroseismic parameters makes this catalogue a useful tool for analysing the mass dependence of deep mixing. We also use the APOGEE survey for spectroscopic parameters for our stars, and predict masses for these stars using a regression model (see *Chapter 5*). This which gives us a much larger sample size than using APOKASC alone.

4.1 APOGEE

The Apache Point Observatory Galactic Evolution Experiment (APOGEE, Majewski *et al.* 2017) is one of the programs in the third Sloan Digital Sky Survey (SDSS-III; Eisenstein *et al.* 2011), and was designed to build a database of over 10^5 stars with high resolution ($R \sim 22,500$) near-infrared (NIR; $1.6\text{ }\mu\text{m }H\text{-band}$) spectra. The stars observed mainly consist of RGB and other bright post-main-sequence stars, with observation emphasised in parts of the Milky Way that are heavily obscured by dust. The abundance of red giants in the APOGEE data set, combined with its large overlap of Kepler targets, makes it ideal for a study on deep mixing. Many other large surveys are based on optical observations, which leaves them hampered by interstellar dust in the Galactic plane. In Figure 4.1 we have a comparison of APOGEE to other Galactic surveys in terms of resolution and number of stars observed (top) and in terms of the expected nominal depth of the

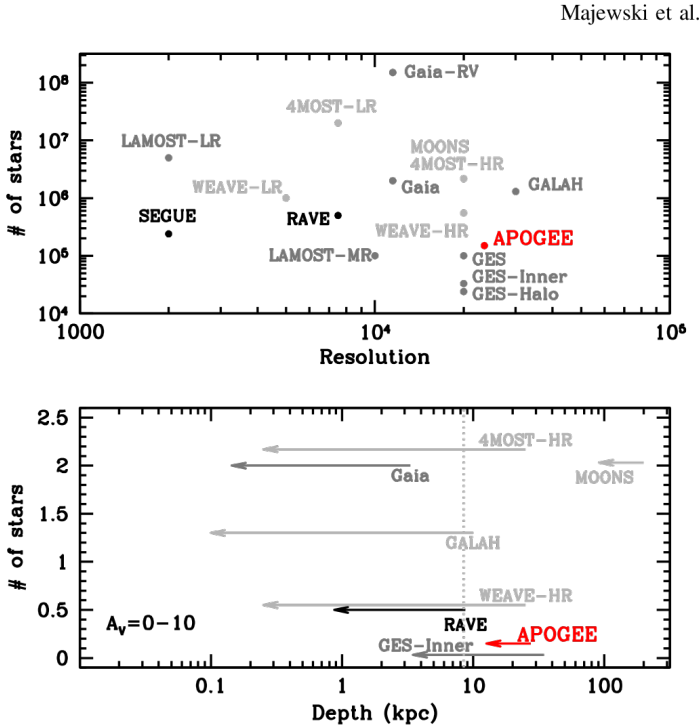


Figure 4.1: APOGEE in the context of other Galactic archaeology surveys, past, present, and future from Majewski *et al.* (2017).

The top panel shows the number of Milky Way stars, observed or anticipated, as a function of survey resolution. For those surveys with at least a resolution of $R = 10,000$ the bottom panel shows the expected nominal depth of the survey for a star with $M_V = -1$ in the case of no extinction (right end of arrows) and in the case of $A_V = 10$ (left end of arrows). In both panels, already completed surveys are shown in black, ongoing surveys in dark grey, and planned surveys in light grey. For surveys with multiple resolution modes, data in the top panel are plotted separately for high resolution (HR), medium resolution (MR), and/or low resolution (LR). For the *Gaia*/ESO survey, data for the “Inner Galaxy” and “Halo” subsamples are shown separately as well. “*Gaia*-RV” includes *Gaia* HR spectra of enough S/N to deliver radial velocities, whereas “*Gaia*” indicates only those with S/N high enough for abundance work. For *Gaia*, we adopted A_G/A_V from Jordi *et al.* (2010), assuming $(V - I_C)_0 = 1.7$; sample numbers were taken from <http://www.cosmos.esa.int/web/gaia/science-performance>. Figure and caption originally Figure 1 from Majewski *et al.* (2017).

survey, taking into account extinction from interstellar dust (bottom). From this figure you note that while APOGEE observes fewer stars than other surveys of comparable resolution, it covers a larger volume of the galaxy.

APOGEE uses the 2.5 m Sloan Foundation Telescope (Gunn *et al.*, 2006), using a specially designed spectrograph (Wilson *et al.*, 2019) to obtain the spectra. A second site was established in 2014 using the 2.5 m du Pont Tele-

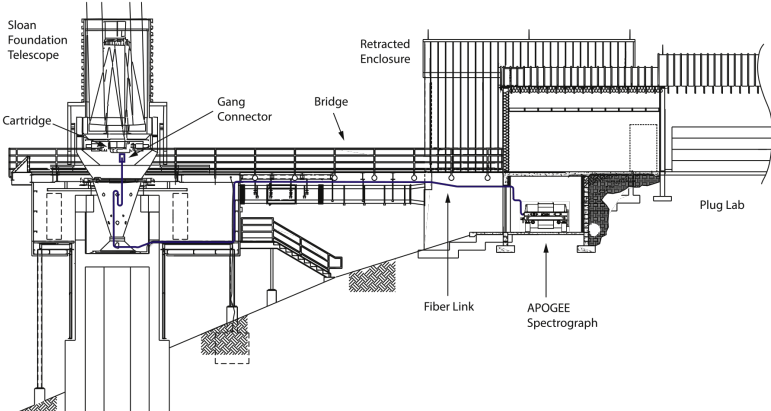


Figure 4.2: Diagram of the Sloan Foundation Telescope and APOGEE Spectrographs. Fibre routing from the telescope to the instrument in the adjacent warm support building. Three hundred fibres, each about 46 m long and made up of two segments, transfer the light imaged by the telescope onto the fibres at the plug plate to the instrument pseudo-slit. Figure includes a portion of the telescope schematic originally shown in Gunn *et al.* (2006). Figure and caption originally Figure 1 in Wilson *et al.* (2019)

scope at the Las Campanas Observatory in Chile, for southern hemisphere observations (Majewski *et al.*, 2017). The spectrograph at the second site is a near identical copy of the original instrument (Wilson *et al.*, 2019). Abundances were determined through the APOGEE Stellar Parameter and Chemical Abundances Pipeline (ASPCAP, García Pérez *et al.* 2016), which fits the APOGEE spectra to synthetic spectra produced by Zamora *et al.* (2015). The ASPCAP pipeline gives us the stellar parameters T_{eff} , $\log(g)$, [M/H], $[\alpha/\text{M}]$ and abundances C, N, O, Na, Mg, Al, Si, S, K, Ca, Ti, V, Mn, Fe, Ni. The full data analysis is described in Holtzman *et al.* (2015, 2018).

4.2 Kepler & K2

NASA's *Kepler* satellite was launched in 2009 and was designed as an exoplanet finding survey telescope (Borucki *et al.*, 2010). However, the lightcurve data generated in this survey is also useful for asteroseismology, and was used to determine the masses and radii of the stars in the APOKASC catalogue (Majewski *et al.*, 2017). After two of the reaction wheels failed, the spacecraft mission was updated to K2 (Howell *et al.*, 2014); however, our project only utilises data from the original *Kepler* mission. Many previous projects have used *Kepler* or K2 for performing asteroseismology on red giants, including determining their evolutionary state (Stello

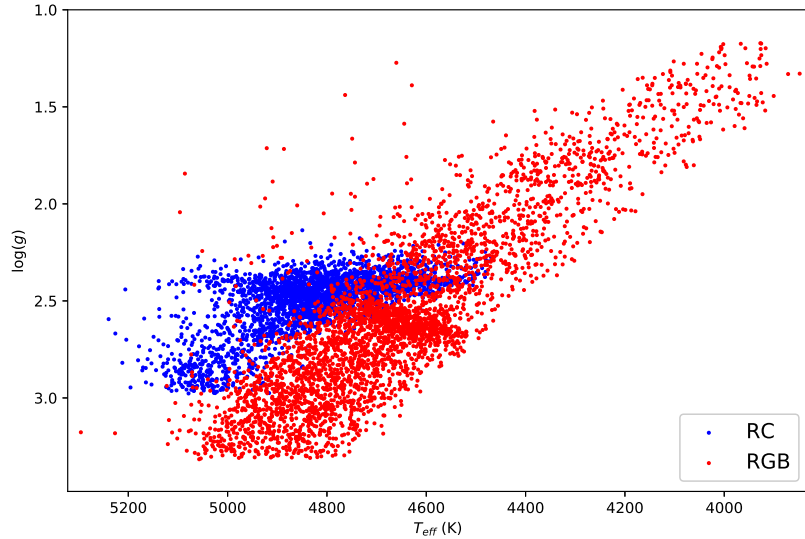


Figure 4.3: H-R Diagram of the stars in the APOKASC-2 catalogue (Pinsonneault *et al.*, 2018). The effective temperature (T_{eff}) is determined spectroscopically, while the surface gravity ($\log(g)$) was determined via asteroseismology. RGB stars are plotted in red while RC stars are plotted in blue.

et al., 2013; Elsworth *et al.*, 2017) and determining ages (Silva Aguirre *et al.*, 2018), so it has been proven to be a reliable and useful source for determining masses for giants. It is estimated that 22,000 oscillating red giants have been observed in *Kepler* (Hon *et al.*, 2019), so a large overlap with spectroscopic surveys is likely.

4.3 The APOKASC Catalogue

The APOKASC catalogue combines spectroscopic data obtained by the APOGEE survey with asteroseismic data from *Kepler*, which was analysed by members of the *Kepler* Asteroseismology Science Consortium (KASC). The first APOKASC catalogue (APOKASC-1, Pinsonneault *et al.* 2014) was released in 2014, using the 10th data release of SDSS (hereafter SDSS DR10, Ahn *et al.* 2014), and contained estimates for the mass, radius, mean density and surface gravity for 1916 red giants. The second APOKASC catalogue (APOKASC-2, Pinsonneault *et al.* 2018) used the 14th data release of the SDSS (hereafter SDSS DR14, Abolfathi *et al.* 2018), and was released in 2018. The second release is not only significantly larger than the

first, having asteroseismic data for 6676 stars, but the spectroscopic pipeline has also been modified since SDSS DR10, with much greater accuracies for spectroscopic parameters. This will affect the asteroseismic parameters too as they are derived using T_{eff} , and if grid-based modelling is used, [Fe/H] and $[\alpha/\text{Fe}]$ are also used.

APOKASC-1 used grid-based modelling to predict the asteroseismic data, while APOKASC-2 adopted an empirical approach utilising scaling factors $f_{\nu_{\text{max}}}$ and $f_{\Delta\nu}$, which are empirically calculated to be in agreement with known data. The corrected mass and radius in APOKASC-2 are then determined by the following relationships:

$$M_{\text{cor}} = \frac{f_{\nu_{\text{max}}}^3}{f_{\Delta\nu}^4} M_{sc} \quad (4.1)$$

$$R_{\text{cor}} = \frac{f_{\nu_{\text{max}}}}{f_{\Delta\nu}^2} R_{sc} \quad (4.2)$$

Where M_{sc} and R_{sc} are determined by equations 2.34 and 2.35. The factor $f_{\Delta\nu}$ is treated as a function of stellar parameters, and is calculated star-to-star. Meanwhile the factor $f_{\nu_{\text{max}}}$ is a scalar calibrated to fit with the known data. Ages are also determined for these stars, using the derived mass, surface gravity, [Fe/H] and $[\alpha/\text{Fe}]$ and stellar evolution models. The median systematic mass uncertainties calculated for RGB stars are around 4%, while those for RC stars are higher, at around 9%.

4.4 Catalogue Matching and Sample Selection

To ensure that high quality data is used for this project, we use the target flags in the APOGEE catalogue. First we remove the high temperature stars that were used to remove telluric absorption features (TARG_FLAGS: APOGEE_TELLURIC), and all stars that are flagged as having either “bad” or no stellar parameters, ASPCAPFLAGS:

- STAR_BAD
- ATMOS_HOLE_BAD
- BAD_PIXELS,
- BAD_RV_COMBINATION
- APOGEE_SCI_CLUSTER
- APOGEE_SGR_DSPH,
- APOGEE2_DSPH_CANDIDATE

We also remove any stars that failed their abundance calculation for [C/Fe], [N/Fe] or [O/Fe], and remove any stars that fail surface gravity determination, all of which produce values of -9999. This selection criteria is very similar to that used by Shetrone *et al.* (2019).

In the APOKASC catalogue we ensure that we have seismic data for all of our stars and remove any that do not (Notes: No Seis) as well as removing stars that have large uncertainties in their seismic parameters (Notes: SeisUnc) and stars that don't have scaling parameters (Notes: No Fdnu). Stars that have ages that are greater than 14 Gyr are also removed (Notes: Ageold). We add APOGEE abundances to the APOKASC catalogue by matching their 2MASS IDs to their APOGEE IDs.

CHAPTER 5

Predicting Masses

The first task we set ourselves in this project is to estimate the masses of APOGEE stars. The masses will be estimated using machine learning, with the APOKASC catalogue as a training set. The first step in this progress will be to identify the method which produces the best results, after which we will apply this to the full APOGEE dataset to predict the masses of the stars.

5.1 Machine Learning Methods

We train the regressors by splitting the APOKASC catalogue into a training set, and a test set. The split is done such that stars are selected for each set randomly, and the training set contains 80% of the catalogue. The four methods we will be testing are linear regression, random forest regression, a multilayer perceptron and Bayesian ridge regression. The four regressors are from the `Scikit-Learn` Python library (Pedregosa *et al.*, 2011). With each regression we will use the surface temperature (T_{eff}), surface gravity ($\log g$), metallicity ([Fe/H]) and alpha abundance ([α /Fe]) as feature inputs, along with [C/Fe], [N/Fe] and [O/Fe]. These features were chosen as T_{eff} and $\log g$ vary with age in a way that is dependent on [α /Fe] and [Fe/H]. The carbon and nitrogen abundances only change during the first dredge up and during the extra-mixing process, which are both metallicity and mass dependent, and oxygen abundance is expected to remain constant, but is included as the three abundances are calculated from similar spectral lines (CH, CN and CO). As such these abundances, combined with their metallicity, temperature and surface gravity should give an indication of the mass of the star. We will begin by providing a brief outline of each method,

before going over the results produced. Information on how the regression models work was taken from the **Scikit-Learn** documentation, which can be found here: <https://scikit-learn.org/stable/documentation.html>

5.1.1 Linear Regression

The simplest of the four methods used, linear regressions assumes that each feature of the data can be scaled and added linearly to produce the predicted value. The regression will try to fit the data to the following equation:

$$y = \beta_0 + \beta_1 x_1 + \beta_2 x_2 + \beta_3 x_3 + \dots + \beta_n x_n \quad (5.1)$$

Where the x_1, x_2, \dots, x_n are the features the regression uses to predict values, and the β values are weights applied to each feature. The regression then uses an ordinary least squares fit to determine the weights that best fit the data given. Once the weights are determined new values can be predicted using those weights.

5.1.2 Random Forest Regression

Random forests are an ensemble learning method for regression, averaging the output of multiple decision trees to improve accuracy and reduce overfitting. A decision tree uses binary rules to calculate the desired variable. In essence the regressor asks a series of true-false questions about the data to determine the target value. This process has a tendency to over-fit to the training data, which makes it worse at predicting on new data. A random forest uses multiple decision trees which are trained on a random sample of the training set. While this will increase the variance of each tree, it lowers the variance over the entire forest. The largest drawback of a random forest is its inability to extrapolate outside of the scope of its training set. This will result in any stars in APOGEE that exist outside the scope of the training set will not have their masses predicted accurately.

5.1.3 Multilayer Perceptron

A multilayer perceptron (MLP) is a supervised machine learning algorithm that uses a training dataset to learn a non-linear function to make predictions in new data, and can be used for both classification and regression problems. In essence an MLP is the most simple version of a neural network, a form of machine learning which we chose not to examine further for this project unless the MLP performed relatively well. An MLP consists of multiple hidden layers between the input and output layers, where each hidden layer contains multiple ‘neurons’, which have an ‘activation function’ which maps the weighted inputs to the output of each neuron, mimicking

Method	Correlation	RMSE
Linear Regression	0.759	0.241
Random Forest	0.871	0.191
Multilayer Perceptron	0.520	0.350
Bayesian Ridge	0.759	0.241

Table 5.1: Correlation coefficient and root-mean-squared errors for the four mass prediction methods.

biological neurons. The MLP learns by adjusting the weights based on the amount of error in the output compared to the known result. The ability to learn non-linear models are one of the primary advantages of an MLP, though it is disadvantaged by its sensitivity to feature scaling and the tuning of hyperparameters, such as the number of hidden neurons, layers and iterations.

5.1.4 Bayesian Ridge Regression

Bayesian ridge regression is similar to linear regression discussed earlier, but instead uses probability distributions rather than point estimates. The variable we predict \hat{y} is not a single value, but is rather drawn from a distribution. Additionally diagonal entries of the correlation matrix are shifted slightly towards zero to add a bias to the coefficients and stabilise them. This is designed to reduce multicollinearity, where one variable in a multiple regression model can be predicted from the others with a degree of accuracy. In general we expect similar results between the Bayesian ridge and linear regression models.

5.2 Determining the Best Model

We quantify the quality of the predictions using the root-mean-squared error (RMSE) and the correlation of the predictions. The RMSE is a measure of the average error in the predictions and is calculated as:

$$\text{RMSE} = \sqrt{\frac{\sum_{i=1}^N (\hat{y}_i - y_i)^2}{N}} \quad (5.2)$$

Where \hat{y}_i is the predicted value, y_i is the regression's dependent variable and N is the total number of observations. We also calculate the Pearson correlation coefficient ($r_{\hat{y}\hat{y}}$) between the predicted mass and asteroseismic mass. This gives us an idea of the predictive power of the regression. The correlation coefficient measures how close two variables are to a linear relationship, and takes a value between -1 and 1, with 1 being a positive

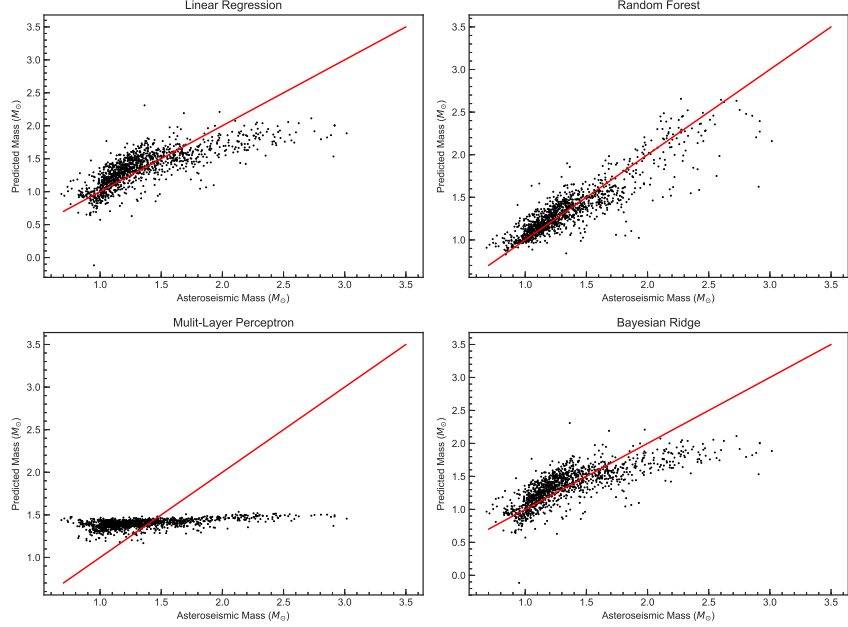


Figure 5.1: Comparison of the four different regression methods for predicting mass. The x -axis is the mass of the star predicted by asteroseismology, and the y -axis is the mass predicted by the regression. The red line is a line of $y = x$ representing the case that the predicted mass equals the asteroseismic mass

correlation, -1 being an anti-correlation and 0 being no correlation between the two variables. The correlation coefficient is calculated as:

$$r_{y\hat{y}} = \frac{\sum_{i=1}^N y_i \hat{y}_i - N \bar{y} \hat{\bar{y}}}{\sqrt{\sum_{i=1}^N y_i^2 - N \bar{y}^2} \sqrt{\sum_{i=1}^N \hat{y}_i^2 - N \hat{\bar{y}}^2}} \quad (5.3)$$

Where N is the total number of observations, y and \hat{y} are the asteroseismic and predicted masses respectively, and \bar{y} and $\hat{\bar{y}}$ are their means. The RMSE and correlation of the four prediction methods are listed in Table 5.1. As we can see the random forest regression greatly outperforms the other three methods in terms of both RMSE and correlation. Figure 5.1 plots the predicted mass against the asteroseismic mass, with a red line is a line of $y = x$ and represents the ideal case of predicted mass equals asteroseismic mass. This is to demonstrate the different correlations of the methods, as the methods with high correlation will have their data fall close to this line.

Due to the random forest regression's (hereafter RFR) clear superiority to the other methods we will use that to predict the masses of the APOGEE stars. It is important to note the short comings of this prediction method,

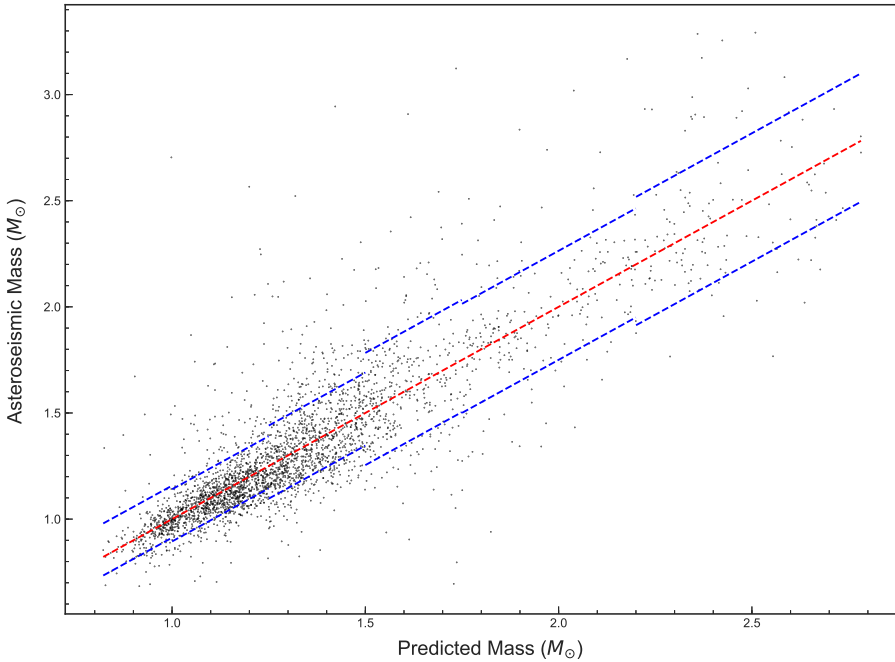


Figure 5.2: Mass predicted by a random forest regression plotted against the mass determined by asteroseismology for APOKASC stars. The blue dashed lines are 68% contour intervals indicating two standard deviations of the mass samples. The data is subdivided into mass samples $M/M_{\odot} < 1.00$, $1.00 \leq M/M_{\odot} < 1.25$, $1.25 \leq M/M_{\odot} < 1.50$, $1.50 \leq M/M_{\odot} < 1.75$, $1.75 \leq M/M_{\odot} < 2.20$ and $2.20 \leq M/M_{\odot}$. For each mass selection we fit a skewed normal distribution to the distribution of $M_{\text{Pred}} - M_{\text{Astero}}$, and calculate 68% confidence intervals based on the distribution (blue dashed lines). The red dashed line is a line of $y = x$, representing a predicted mass with 0 error.

which include that it over-predicts the mass of low mass stars ($M < 1M_{\odot}$), under-predicts the mass of intermediate mass stars ($M > 2.0M_{\odot}$) and cannot make predictions higher than the highest mass in the training set (in the training set used to make our regression models this was $\approx 3.1M_{\odot}$). The vast majority of the stars observed by APOGEE should exist in the range of $1.0 < M/M_{\odot} < 2.0$ so the predictions will be reasonably accurate for the majority of our dataset.

5.3 Uncertainties in Predictions

It is important to quantify the uncertainties in the predictions. To do this we use the test set used to validate the accuracy of the RFR. As noted by

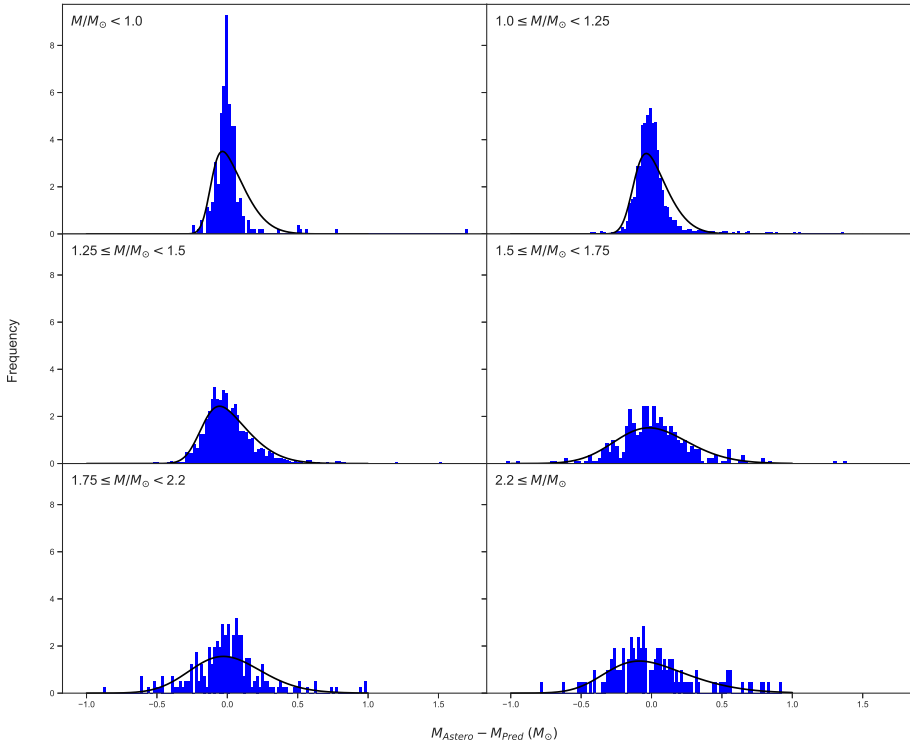


Figure 5.3: The normalised distribution of astroseismic mass M_{Astero} and predicted mass M_{Pred} for each mass selection. The blue histogram is the distribution of the difference in each mass selection, and the black line is the fitted skewed-normal distribution, the properties of which can be found in Table 5.2.

before there tends to be an over-prediction of mass at low masses and an under-prediction of masses at higher mass. Further more the distribution of the difference between predicted and astroseismic masses tends to be skewed, so our uncertainties will be asymmetrical. To account for this we split the dataset into 6 subsets based on their mass as follows, $M/M_\odot < 1.00$, $1.00 \leq M/M_\odot < 1.25$, $1.25 \leq M/M_\odot < 1.50$, $1.50 \leq M/M_\odot < 1.75$, $1.75 \leq M/M_\odot < 2.20$ and $2.20 \leq M/M_\odot$. For each mass range we fit a skewed normal distribution to the difference between astroseismic mass (M_{Astero}) and predicted mass (M_{Pred}). We use the “skewnorm” function in the SciPy python library (Virtanen *et al.*, 2019). This function allows us to fit a skewed normal distribution to the dataset, return parameters of the distribution (skewness, mean, variance, and kurtosis), and find confidence intervals based on the distribution. From this skewed normal distribution we calculate the 68% confidence interval so we can determine the uncertainty for new predictions within 2 standard deviations. These values are presented in Table 5.2, and the predicted mass is plotted against astroseismic mass in

Mass Range	Mean	Variance	Skew	Kurtosis	Median	68% Confidence Interval
$M/M_{\odot} < 1.00$	0.033	0.020	0.764	0.611	0.014	-0.088 – 0.158
$1.00 \leq M/M_{\odot} < 1.25$	0.016	0.020	0.657	0.500	0.000	-0.105 – 0.141
$1.25 \leq M/M_{\odot} < 1.50$	0.016	0.030	0.637	0.480	-0.005	-0.154 – 0.190
$1.50 \leq M/M_{\odot} < 1.75$	0.018	0.070	0.260	0.145	0.006	-0.246 – 0.283
$1.75 \leq M/M_{\odot} < 2.20$	0.007	0.070	0.251	0.138	-0.004	-0.250 – 0.264
$2.20 \leq M/M_{\odot}$	0.013	0.100	0.534	0.379	-0.018	-0.287 – 0.318

Table 5.2: Properties of the skewed-normal distribution fitted to each mass range.

Figure 5.2, and the distributions of each mass selection are plotted in Figure 5.3.

5.4 Predicting APOGEE Masses

We can now apply the RFR to the full APOGEE dataset. Since the RFR cannot predict outside of the parameter space of its training set, we limit the range of masses used by the bounds of the APOKASC dataset. This gives us the following selection criteria for APOGEE stars: $-2.34 \leq [\text{Fe}/\text{H}] \leq 0.54$, $-0.19 \leq [\alpha/\text{Fe}] \leq 0.52$, $-0.71 \leq [\text{C}/\text{Fe}] \leq 0.52$, $-0.87 \leq [\text{N}/\text{Fe}] \leq 0.92$, $1.07 \leq \log(g) \leq 3.63$, $3848 \text{ K} \leq T_{\text{eff}} \leq 5227 \text{ K}$. This will ensure that all the stars that we predict the masses for will be mostly accurate, and within the expected uncertainty range for each mass selection. This leave 139,473 in the reduced APOGEE dataset, all now with determined masses. The distribution of the predicted masses in the APOGEE dataset are shown in Figure 5.4.

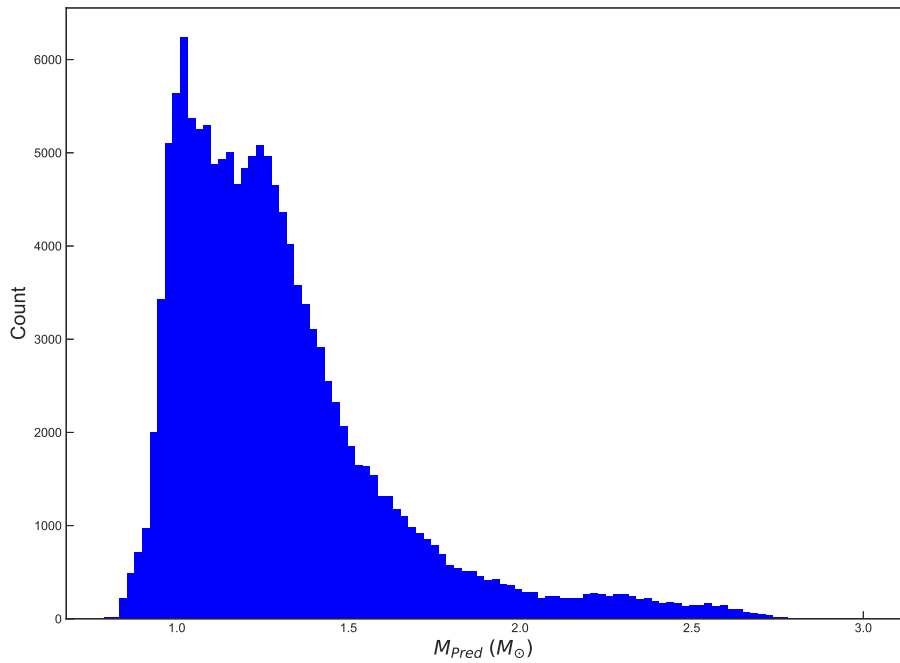


Figure 5.4: Distribution of predicted masses from the APOGEE dataset

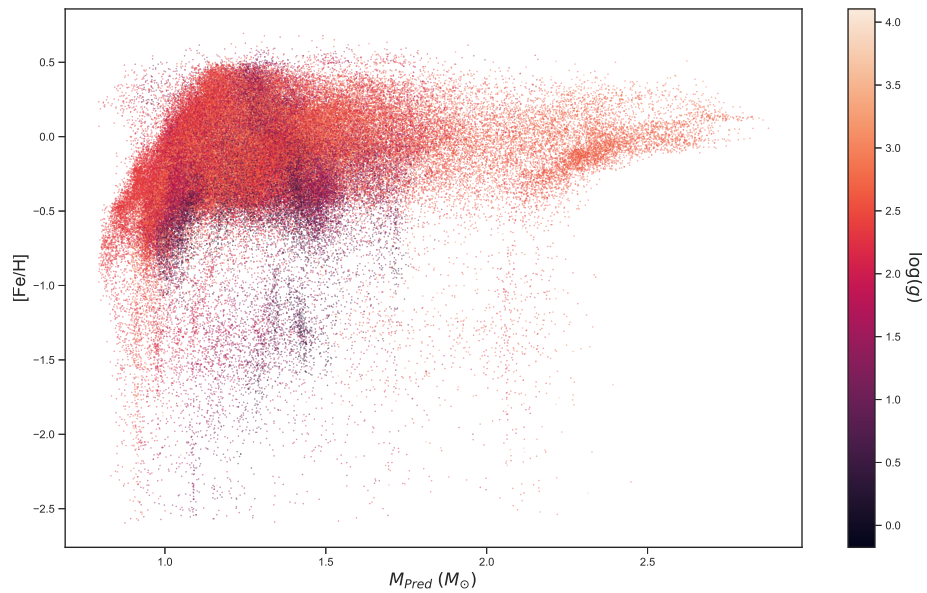


Figure 5.5: Predicted mass vs metallicity for APOGEE stars. The colouring indicates the surface gravity of each star. We note the lack of intermediate mass stars ($M > 2.00 M_\odot$) of low metallicity or surface gravity.

CHAPTER 6

Constraining Mixing Rates

One of the primary goals of this project is to determine the mass and metallicity dependence of the deep mixing rate. Now that we have estimates for the masses of all APOGEE stars we can separate them into groups of different masses and metallicities, and determine the rate at which carbon and nitrogen change with respect to surface gravity. We choose to subdivide our dataset into 25 subgroups, with masses ranges of $M/M_{\odot} < 1.00$, $1.00 \leq M/M_{\odot} < 1.25$, $1.25 \leq M/M_{\odot} < 1.50$, $1.50 \leq M/M_{\odot} < 2.20$, and $2.20 \leq M/M_{\odot}$ as well as metallicity ranges of $0.25 \geq [\text{Fe}/\text{H}] > -0.25$, $-0.25 \geq [\text{Fe}/\text{H}] > -0.75$, $-0.75 \geq [\text{Fe}/\text{H}] > -1.25$, $-1.25 \geq [\text{Fe}/\text{H}] > -1.75$ and $-1.75 \geq [\text{Fe}/\text{H}] > -2.50$. The mass selections reflect our choices for the categorisation of the mass prediction uncertainties, combining the $1.50 \leq M/M_{\odot} < 1.75$ and $1.75 \leq M/M_{\odot} < 2.20$ mass ranges due to the comparatively few stars in this range. The metallicity selections are chosen to split the dataset in a way such that the bins contain enough stars that a trend in abundance can be determined, while being small enough that the changes in metallicity reflected in abundance patterns is evident. Before we can calculate the mixing rate, we must identify the region where the mixing begins, the RGB bump so we can accurately know the pre-mixing carbon without confusing this for the value while the FDU is occurring.

6.1 Finding the Red Giant Branch Bump

To find the RGB bump (RGBb) we use the synthetic isochrones from the Dartmouth Stellar Evolution Database as described in Dotter *et al.* (2008). These isochrones provide stellar parameters for stars with the same composition over varying mass, effectively creating a synthetic globular cluster.

$\langle [\text{Fe}/\text{H}] \rangle$	[Fe/H]	$[\alpha/\text{Fe}]$	Y	$Z (10^{-3})$	RGBb Min	RGBb Max	RGBb Mean
0.50	0.55	-0.20	0.3105	40.420	2.58	2.63	2.60
	0.56	0.00	0.3294	52.071	2.60	2.67	2.63
	0.57	0.20	0.3537	67.081	2.60	2.67	2.64
0.00	0.06	-0.20	0.2682	14.342	2.51	2.59	2.54
	0.07	0.00	0.2741	18.850	2.53	2.63	2.58
	0.00	0.00	0.3300	15.000	2.42	2.47	2.45
	0.00	0.00	0.4000	13.432	2.31	2.33	2.32
	0.07	0.20	0.2863	25.504	2.55	2.65	2.62
	0.07	0.40	0.3020	35.205	2.57	2.66	2.63
	0.01	0.40	0.3300	29.760	2.51	2.56	2.55
	0.01	0.40	0.4000	26.600	2.38	2.40	2.40
	-0.50	-0.51	-0.20	0.2516	4.0467	2.32	2.37
-0.50	-0.50	0.00	0.2537	5.2740	2.36	2.41	2.40
	-0.50	0.00	0.3300	4.8170	2.23	2.26	2.25
	-0.50	0.00	0.4000	4.3137	-	-	-
	-0.49	0.20	0.2571	7.4439	2.40	2.46	2.44
	-0.49	0.40	0.2623	1.0686	2.43	2.51	2.48
	-0.49	0.40	0.3300	9.7045	2.32	2.36	2.35
	-0.49	0.40	0.4000	8.6906	-	-	-
	-1.00	-1.01	-0.20	0.2471	1.2930	2.13	2.17
-1.00	-1.00	0.00	0.2478	1.7242	2.17	2.21	2.20
	-1.00	0.00	0.3300	1.5308	2.02	2.03	2.03
	-1.00	0.00	0.4000	1.3709	-	-	-
	-0.99	0.20	0.2489	2.3966	2.20	2.24	2.23
	-0.99	0.40	0.2506	3.4642	2.25	2.30	2.29
	-0.99	0.40	0.3300	3.0995	2.13	2.13	2.13
	-0.99	0.40	0.4000	2.7757	-	-	-
	-1.50	-1.51	-0.20	0.2457	0.40983	1.96	2.00
-1.50	-1.50	0.00	0.2459	0.54651	1.99	2.02	2.02
	-1.50	0.00	0.3300	0.48484	-	-	-
	-1.50	0.00	0.4000	0.43418	-	-	-
	-1.49	0.20	0.2462	0.76184	2.03	2.06	2.05
	-1.49	0.40	0.2468	0.5.6277	2.06	2.10	2.09
	-1.49	0.40	0.3300	0.98327	-	-	-
	-1.49	0.40	0.4000	0.88054	-	-	-
	-2.00	-2.01	-0.20	0.2452	0.12990	-	-
-2.00	-2.00	0.00	0.2453	0.17240	1.84	1.84	1.84
	-2.00	0.00	0.3300	0.15339	-	-	-
	-2.00	0.00	0.4000	0.13737	-	-	-
	-1.99	0.20	0.2454	0.24080	1.88	1.88	1.88
	-1.99	0.40	0.2456	0.35040	1.91	1.94	1.93
	-1.99	0.40	0.3300	0.31135	-	-	-
	-1.99	0.40	0.4000	0.27873	-	-	-
	-2.50	-2.51	-0.20	0.2451	0.040890	-	-
-2.50	-2.50	0.00	0.2451	0.054739	-	-	-
	-2.50	0.00	0.3300	0.048515	-	-	-
	-2.50	0.00	0.4000	0.043447	-	-	-
	-2.49	0.20	0.2451	0.076210	-	-	-
	-2.49	0.40	0.2452	0.011110	-	-	-
	-2.49	0.40	0.3300	0.098457	-	-	-
	-2.49	0.40	0.4000	0.088170	-	-	-

Table 6.1: Synthetic isochrone parameters from Dotter *et al.* (2008).

The isochrones also vary with age, allowing us to examine globular clusters with intermediate mass stars on the giant branch, which is useful for our purposes. The composition of each isochrone is varied by 3 parameters: Metallicity ($[\text{Fe}/\text{H}]$, which spans from $-2.5 \leq [\text{Fe}/\text{H}] \leq 0.5$), alpha abundance ($[\alpha/\text{Fe}]$, which spans from $-0.2 \leq [\alpha/\text{Fe}] \leq 0.8$) and mass fraction of helium (Y, which takes values of $Y=0.245+1.54Z$, 0.3300 and 0.4000, where Z is the mass fraction of all metals). Each isochrone provides observable stellar parameters such as luminosity, surface temperature and surface gravity, which we can use to find where the RGBb occurs for each mass and metallicity range. The file for each isochrone contains data for the same isochrone observed at 37 different ages between 1 and 15 Gyr, with each age containing ≈ 277 stars of varying masses spaced from the start of the main sequence to the tip of the red giant branch (RGBt). Some evolutionary

Mass Range	$0.25 \leq [\text{Fe}/\text{H}] < -0.25$	$-0.25 \geq [\text{Fe}/\text{H}] > -0.75$	$-0.75 \geq [\text{Fe}/\text{H}] > -1.25$	$-1.25 \geq [\text{Fe}/\text{H}] > -1.75$	$-1.75 \geq [\text{Fe}/\text{H}] > -2.25$
$0.50 \leq M/M_{\odot} < 1.00$	2.241 – 2.666 (2.502)	2.003 – 2.509 (2.330)	1.781 – 2.301 (2.158)	1.605 – 2.106 (1.985)	1.622 – 1.953 (1.838)
$1.00 \leq M/M_{\odot} < 1.25$	2.187 – 2.661 (2.549)	1.946 – 2.500 (2.312)	1.736 – 2.277 (2.090)	1.569 – 2.060 (1.915)	1.421 – 1.895 (1.750)
$1.25 \leq M/M_{\odot} < 1.50$	2.136 – 2.654 (2.562)	2.121 – 2.432 (2.324)	1.714 – 2.222 (2.087)	1.550 – 2.036 (1.882)	1.560 – 1.881 (1.765)
$1.50 \leq M/M_{\odot} < 2.20$	1.833 – 2.587 (2.328)	1.921 – 2.456 (2.211)	1.999 – 2.186 (2.090)	1.875 – 2.098 (1.947)	1.725 – 1.846 (1.779)

Table 6.2: Location of the RGBb in surface gravity at different mass and metallicity ranges. Stars with masses greater than $2.2M_{\odot}$ are not observed to appear in the RGBb in these isochrones.

tracks terminate at the onset of thermal pulsations on the AGB, but we will not consider those tracks in this project.

To find the RGBb in an isochrone of the desired composition we simply search for an inversion in the trend of either luminosity or surface gravity on the giant branch. In this stage of stellar evolution the luminosity should be increasing while surface gravity decreases, except at the luminosity bump where the opposite is true. Finding the inversion then gives us the location of the bump. To avoid the early stages of evolution where this may also occur we limit our search for the inversion to surface gravities $\log(g) < 3.0$. At every age for each isochrone there is one mass of star at the RGBb, and that mass decreases as you look at older isochrones. Therefore we can work out the age and surface gravity for the RGBb at every age range we are interested in. This will allow us to determine the surface gravity of the luminosity bump for a specific mass and metallicity. To account for other changes in composition which we don't account for in our selections of the APOGEE dataset we examine all possible compositions (The three variations of Y and all possible $[\alpha/\text{Fe}]$) at a specific metallicity to give us the mean surface gravity at the RGBb, as well as upper and lower limits of the luminosity bump, which correspond to the minimum surface gravity before the inversion occurs, and the maximum surface gravity after the inversion in all the compositions. Table 6.1 lists the different compositions and masses of the isochrones, as well as the mean surface gravity for the RGBb and its corresponding upper and lower limits, for isochrones with ages between 10 and 13 Gyr, which are typical ages for a globular cluster. Table 6.2 lists the range in surface gravities where stars of particular masses and metallicities will be in the RGBb. The range was found using the method above, with the average $\log(g)$ of stars in the RGBb given in brackets. It is noteworthy that none of the stars with masses $M > 2.2M_{\odot}$ experience the RGBb. This

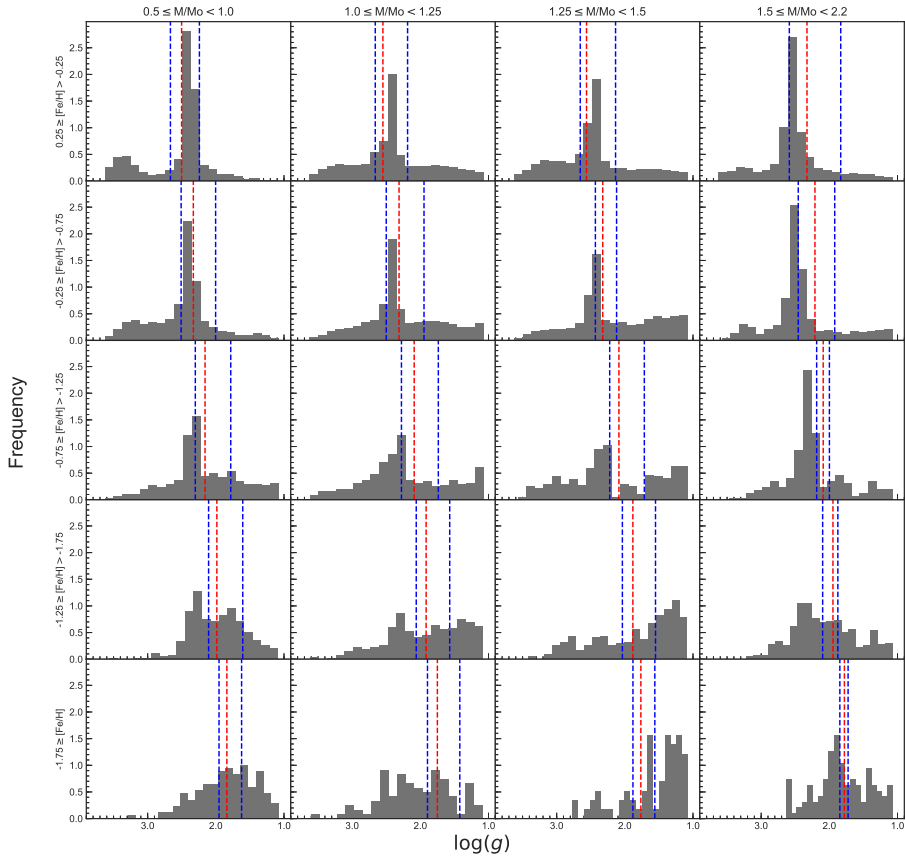


Figure 6.1: Normalised histogram of surface gravity for each of the subsets of APOGEE. The blue dashed lines indicate upper and lower bounds for the RGBb found using the Dartmouth isochrones (Dotter *et al.*, 2008), and the red dashed line is the mean surface gravity of the RGBb for each selection of mass and metallicity. The RGBb can be identified in many subsets as a large overdensity at a small range of surface gravities, and is most clearly seen in the highest metallicity stars. The isochrones tend to predict the RGBb at lower surface gravities than we observe. The histograms have been normalised to increase readability.

is not unexpected and is in line with standard evolutionary theory, as more massive stars begin fusing helium before the H-burning shell reaches the discontinuity in molecular weight (Christensen-Dalsgaard, 2015).

Figure 6.1 plots normalised histograms of the surface gravity for each selection of mass and metallicity that we will use to find the mixing rates in APOGEE. In these plots the RGBb can be clearly identified in many subsets as a large overdensity of stars in a small range of surface gravities. The blue dashed lines indicate the upper and lower bounds of the RGBb

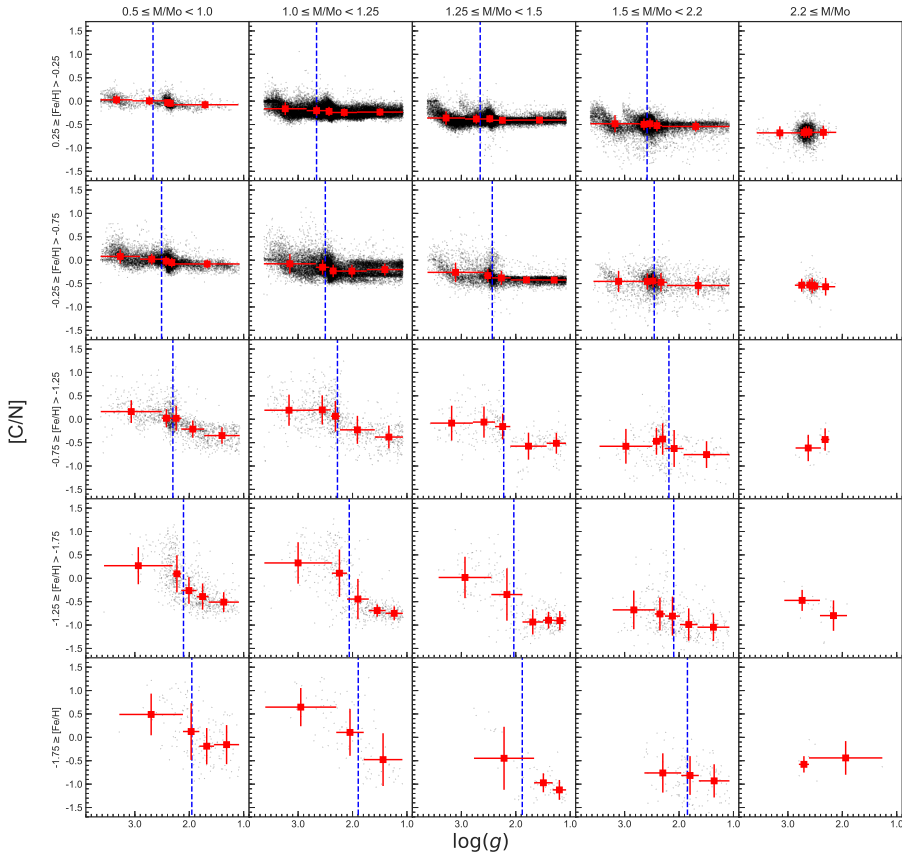


Figure 6.2: [C/N] abundance ratio for different selections of mass and metallicity in the APOGEE dataset. The red squares indicate the mean [C/N] abundance for the selection of $\log(g)$ represented by the horizontal error bar. The vertical error bar indicates the standard deviation of the [C/N] abundance. The dashed blue lines indicate the beginning of where we expect to find the RGBb, as determined in *Section 6.1*.

that we identified using the Dartmouth isochrones, and the red dashed line indicates the mean surface gravity of isochrone stars in the RGBb. It is notable from this that the isochrones tend to predict the RGBb occurring at lower surface gravities than we observe in APOGEE. However the upper bound of the surface gravity seems to roughly line up with the observed RGBb, so we will use this as the region to calculate pre-mixing carbon and nitrogen abundances.

Metallicity	Mass	$\Delta[\text{C}/\text{N}]$	$\Delta \log(g)$	$\frac{d[\text{C}/\text{N}]}{d \log(g)}$
$0.25 \geq [\text{Fe}/\text{H}] > -0.25$	$M/M_{\odot} < 1.00$	-0.08	-1.02	0.08
	$1.00 \leq M/M_{\odot} < 1.25$	-0.03	-1.16	0.03
	$1.25 \leq M/M_{\odot} < 1.5$	-0.02	-1.16	0.02
	$1.50 \leq M/M_{\odot} < 2.2$	-0.06	-0.84	0.07
$-0.25 \geq [\text{Fe}/\text{H}] > -0.75$	$M/M_{\odot} < 1.00$	-0.06	-0.76	0.08
	$1.00 \leq M/M_{\odot} < 1.25$	-0.05	-1.14	0.04
	$1.25 \leq M/M_{\odot} < 1.5$	-0.10	-1.22	0.08
	$1.50 \leq M/M_{\odot} < 2.2$	-0.10	-0.83	0.12
$-0.75 \geq [\text{Fe}/\text{H}] > -1.25$	$M/M_{\odot} < 1.00$	-0.37	-0.84	0.44
	$1.00 \leq M/M_{\odot} < 1.25$	-0.45	-0.98	0.45
	$1.25 \leq M/M_{\odot} < 1.5$	-0.36	-0.99	0.36
	$1.50 \leq M/M_{\odot} < 2.2$	-0.13	-0.60	0.22
$-1.25 \geq [\text{Fe}/\text{H}] > -1.75$	$M/M_{\odot} < 1.00$	-0.25	-0.64	0.39
	$1.00 \leq M/M_{\odot} < 1.25$	-0.30	-0.67	0.46
	$1.25 \leq M/M_{\odot} < 1.5$	-0.56	-0.97	0.57
	$1.50 \leq M/M_{\odot} < 2.2$	-0.24	-0.75	0.32
$-1.75 \geq [\text{Fe}/\text{H}] > -2.50$	$M/M_{\odot} < 1.00$	-0.28	-0.65	0.43
	$1.00 \leq M/M_{\odot} < 1.25$	-0.58	-0.61	0.96
	$1.25 \leq M/M_{\odot} < 1.5$	-0.68	-1.02	0.66
	$1.50 \leq M/M_{\odot} < 2.2$	-0.11	-0.44	0.26

Table 6.3: Change in [C/N] abundance for different selections of mass and metallicity.

6.2 Mixing Rates as Functions of Mass and Metallicity

To get an estimate of how the abundances change with respect to surface gravity we can find the mean [C/N] abundance ratio for varying selections of surface gravity. To do this we subdivide each mass-metallicity selection into a set number of bins based on their surface gravities, with each bin containing approximately an equal number of stars (the number of stars per bin will alter depending on how many stars are in each mass-metallicity selection). Then for each bin we calculate the mean [C/N] ratio and its standard deviation, which we can use to quantify the extent of the mixing. We choose the number of bins we split the data into based on the size of the subset. For a subset of N stars we use 5 bins to calculate the mixing rate if $N \geq 250$, if $150 < N \leq 250$ we use 4 bins, if $50 < N \leq 150$ we use 3 bins and if $N \leq 50$ then we only use 2 bins. We choose the bin closest to the upper limit of the RGBb as identified in the previous selection as the pre-mixing [C/N] abundance, and the last bin as the post-mixing [C/N]. From this we can easily calculate $\Delta[\text{C}/\text{N}]$, and we also find the mixing rate $\frac{d[\text{C}/\text{N}]}{d \log(g)} = \frac{\Delta[\text{C}/\text{N}]}{\Delta \log(g)}$.

The [C/N] ratio for our selection of APOGEE stars is plotted in Figure

6.2, where the red crosses indicate the mean [C/N] abundance for that selection of stars, as well as the standard deviation. Table 6.3 lists the change in the [C/N] ratio for each selection of the APOGEE dataset, as both the absolute change of the [C/N] ratio, and as a ratio of the change in [C/Fe] over the change in surface gravity ($\frac{d[C/N]}{d\log(g)}$). Additionally the independent carbon and nitrogen trends can be found in Appendix A (Figures A.3 and A.4), along with the pre- and post-mixing abundances (Tables A.1 and A.2).

Also noteworthy from this plot is that almost all the stars with $M \geq 2.2M_{\odot}$ have surface gravities close to $\log(g) \approx 2.6$, which suggests they are likely to be red clump stars, rather than RGB stars. Additionally the amount of scatter in [C/N] increases as we go to lower metallicities. This is likely due to the ASPCAP pipeline performing poorly on low metallicity stars due to the weaker line strength (Holtzman *et al.*, 2018). As a result of this, combined with the comparatively few stars in this metallicity range our calculations of mixing rates become increasingly uncertain at low mass and low metallicity.

CHAPTER 7

Discussion

Now that we have determined the mixing rate's dependence on the mass and metallicity of the stars, we can begin to see how our derived mixing rates compare to other methods, including globular clusters in the APOGEE dataset, theoretical predictions made by Lagarde *et al.* (2012) and previous work from the literature.

7.1 Comparison to Globular Clusters

Comparison between field stars and globular clusters (GCs) is an important step in this project, as stellar populations within the globular clusters are all approximately the same age and are typically of homogeneous composition, differing in only their masses (Carroll and Ostlie, 2006). This makes them ideal candidates to compare the mixing rates in. Additionally much of the previous work on this topic has been performed on GCs. Many GCs were observed in the APOGEE project, and had separate analysis pipelines to determine their properties more accurately. For this project we will consider two additional analyses of GCs in APOGEE, made by Masseron *et al.* (2019) and Nataf *et al.* (2019).

7.1.1 The Masseron Catalogue

For analysis of the GCs in APOGEE we will use the catalogue created by Masseron *et al.* (2019), which contains 885 GC stars in 10 different clusters. The GC included in this catalogue are M2, M3, M5, M13, M15, M53, M71, M92, M107 and NGC 5466. The Masseron *et al.* (2019) catalogue uses the APOGEE spectra, but utilises the Brussels Automatic Code for Characterizing High accUracy Spectra (BACCHUS, Masseron *et al.* 2016) to predict

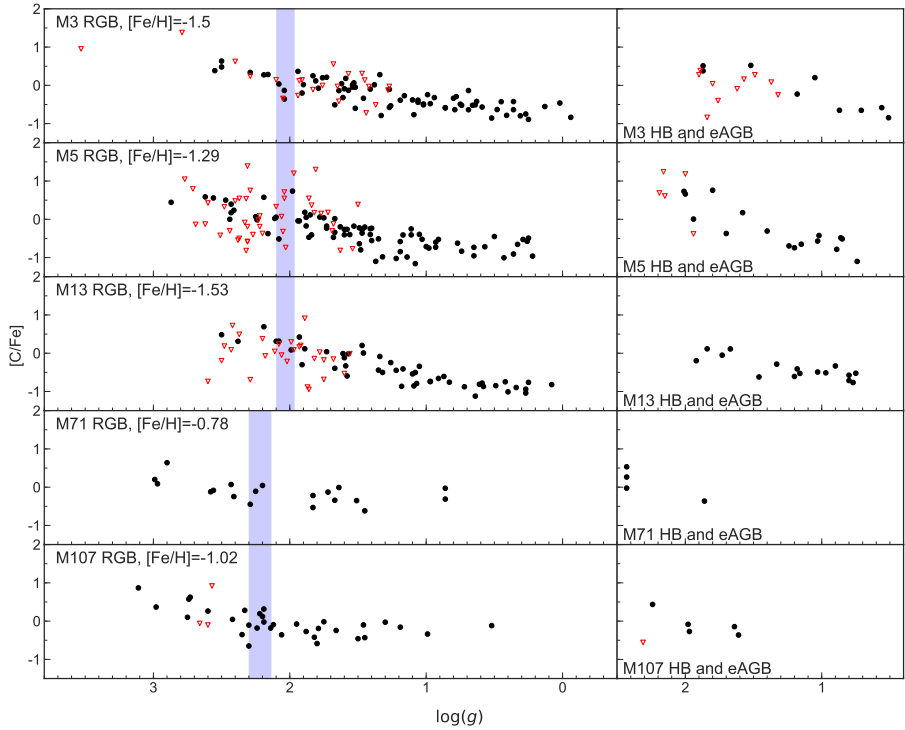


Figure 7.1: [C/Fe] abundances for M3, M5, M13, M71 and M107 on the RGB (left plots) and the HB and early AGB (Right Plots). Black dots indicate stars with a determined [C/Fe] abundance, while red triangles indicate stars with only an upper limit for [C/Fe]. The blue shaded region indicate the mean $\log(g)$ where the RGBb occurs in an isochrone of similar metallicity and age (see Section 6.1).

the stellar properties of the GC stars. Given the unusual abundance patterns found in GCs, a unique pipeline allows for more accurate abundance determination than the standard ASPCAP pipeline, which is optimised for field stars. Stars were selected from the APOGEE catalogue if they were a) previously observed as a member of a cluster b) were a radial velocity member or c) was part of a cluster based on its proper motion.

The BACCHUS code is able to determine metallicity, surface temperature and gravity, microturbulence, macroturbulence and abundances for light elements (C, N, O, Mg, Al, Na, Ca, Si, K) as well as two neutron-capture elements (Nd and Ce). Since the lines used to determine abundances (particularly C, N and O) are weak at the metallicities of many of the globular clusters, upper limits for these abundances are determined instead. Upper limits correspond to abundances where the line strength is comparable to the variance, and consequently is sensitive to the choice in stellar parameters, as well as the signal-to-noise ratio of the spectra. Ad-

ditionally due to the weakness of the spectral lines many stars do not have determined C or N abundances, and are flagged in the dataset as having no spectral lines. We remove these from our data, which leaves us with 206 GC giants with [C/Fe] and [N/Fe] determined, and 303 with upper limits for either [C/Fe] or [N/Fe]. Because of these upper limits in [C/Fe] and [N/Fe] we cannot accurately know [C/N] abundance trends, as many stars have upper limits for both. Instead we look at the changes in [C/Fe] and [N/Fe] separately, and find the independent mixing rates. From the independent mixing rates we can determine the mixing rate for [C/N] which can be found using the logarithm laws, and will be given by:

$$\frac{d[C/N]}{d \log(g)} = \frac{d[C/Fe]}{d \log(g)} - \frac{d[N/Fe]}{d \log(g)} \quad (7.1)$$

For analysis of mixing rates we remove any GCs that have either too few stars, or do not cover a large enough range in $\log(g)$ to accurately determine the mixing rate. We remove M2, M15, M53, M92, and NGC5466, leaving us 5 GCs (M3, M5, M13, M71 and M107) covering a metallicity range of $-0.78 \geq [\text{Fe}/\text{H}] \geq -1.53$. It is unfortunate, but unsurprising that all of the lowest metallicity GCs are removed by this process, as the lines used to calculate abundances are weaker at lower metallicities. For the mean metallicities of the GCs we use the values that were determined in the Harris (2010) catalogue, an updated version of the standard Harris (1996) catalogue.

The [C/Fe] abundance ratio is plotted against $\log(g)$ in Figure 7.1 and [N/Fe] in Figure A.1 (Located in *Appendix A*). In each figure the RGB stars in M3, M5, M13, M71 and M107 are plotted on the left side, while RC and early AGB stars are plotted on the right. The black dots are stars with their abundance determined, and the red triangles are stars with an upper limit for the abundance. Of note in these plots is that we see a relatively strong depletion in [C/Fe], but we only observe a corresponding increase in [N/Fe] in M13, with the other GCs having more or less a steady nitrogen abundance. This may be due to the large number of stars with a only upper limits for [N/Fe] at high $\log(g)$, so their actual abundances are likely lower than the more evolved stars in the same cluster. This is particularly likely in M5 as all of the stars near the RGBb have upper limits.

Also of note is the unusual pattern for the stars determined to be on the HB or eAGB, particularly the carbon abundances. In GCs M3, M5 and M13 we observe a depletion in the carbon abundances over decreasing surface gravity. This is not predicted by canonical stellar evolution theories, or any theories regarding deep mixing. Comparing the abundances of HB and eAGB stars with the RGB stars in the same cluster shows that the abundances calculated align with RGB stars at similar surface gravities. This suggests that this is an error with the abundance calculation pipeline

Cluster	[Fe/H]	# of Stars	$\frac{d[C/Fe]}{d\log(g)}$	$\frac{d[N/Fe]}{d\log(g)}$	$\frac{d[C/N]}{d\log(g)}$
M71	-0.78	12	0.19	-0.18	0.37
M107	-1.02	16	0.10	0.48	-0.38
M5	-1.29	42	0.48	0.12	0.36
M3	-1.5	62	0.43	0.09	0.34
M13	-1.53	47	0.63	-0.19	0.83

Table 7.1: Mixing rates for [C/Fe] and [N/Fe] from Masseron *et al.* (2019).

performed by Masseron *et al.* (2019). Like for the field stars, we find the mixing rates $\frac{d[C/Fe]}{d\log(g)}$ and $\frac{d[N/Fe]}{d\log(g)}$, and define the mixing rate for [C/N] as $d[C/N]/d\log(g) = d[C/Fe]/d\log(g) - d[N/Fe]/d\log(g)$. These results are presented in Table 7.1. To calculate these values we ignored the stars that had upper limits, only using the stars with determined abundances.

7.1.2 The Nataf Catalogue

In addition to the catalogue produced by Masseron *et al.* (2019), we also examine the catalogue of GCs in APOGEE from Nataf *et al.* (2019). This catalogue is an extended version of the one produced by Ting *et al.* (2019). The Ting catalogue uses a code known as *The Payne* to determine abundances, a neural network which is used to determine stellar parameters. The difference between the Nataf *et al.* (2019) and Ting *et al.* (2019) catalogues is that the Ting catalogue was produced using a training set with a restriction of $[Fe/H] \geq -1.50$, while the Nataf catalogue altered this restriction to $[Fe/H] \geq -1.55$, to allow for the inclusion of globular cluster M13 (NGC 6205). Both versions of the catalogue include clusters M3 (NGC 5272), M5 (NGC 5904), M12 (NGC 6218), M71 (NGC 6838) and M107 (NGC 6171), among others, with a total of 42 clusters in the catalogue. Since we are interested in finding trends in the abundances we choose to analyse only clusters with more than 20 stars with abundance information in the catalogue. This selection criteria leaves us with the 6 clusters mentioned previously. All these globular clusters, with the exception of M12, are also in the Masseron catalogue, so comparison between the Nataf, Masseron and ASPCAP abundances will give us insight into the accuracy of the three pipelines.

Figure 7.2 plots the [C/N] abundance against surface gravity. It is notable that these clusters span a smaller range in surface gravity compared to the Masseron *et al.* (2019) catalogue. It is also noteworthy that there appears to be some amount of bimodality in the [C/N] ratio in the plots, which is evident in all clusters except NGC 6171 and NGC 6218, which have too much scatter for any bimodal trends to be visible. This splitting of the [C/N] ratio appears to be an offset, as they appear to decrease at the same rate. This could potentially be a primordial change in the abundances for some

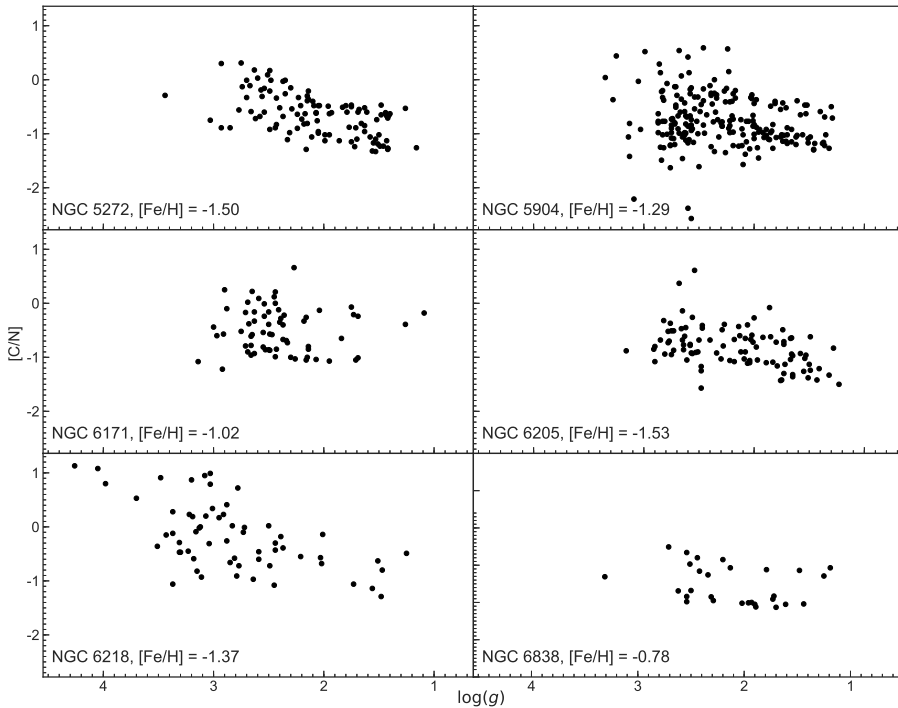


Figure 7.2: $[N/Fe]$ abundance for globular clusters determined by Nataf *et al.* (2019) using *The Payne*. While no clusters show strong increases in $[N/Fe]$, we note a bimodality in all clusters except NGC 6205 and NGC 6218, which have too large a scatter to observe any bimodality.

stars, or a second population of stars within the globular cluster. More likely though it is a fault within *The Payne* pipeline. The mixing rates for $[C/Fe]$, $[N/Fe]$ and $[C/N]$ are presented in Table 7.2. The nitrogen abundances tend to all be increasing, unlike what we observed in the Masseron *et al.* (2019) catalogue, with the exception of M107, where it is increasing. The $[C/N]$ abundance ratio is calculated from the actual $[C/N]$ abundances, rather than calculated as the difference between $d[C/Fe]/d\log(g)$ and $d[N/Fe]/d\log(g)$. We find that

7.1.3 ASPCAP Globular Clusters

To understand how these results in the globular clusters relate to the results we found for field stars we can compare these results to the values determined by the ASPCAP pipeline, which is what is used for the rest of the APOGEE catalogue. To do this we simply locate the stars analysed in either by either Masseron *et al.* (2019) or Nataf *et al.* (2019), and repeat the same method on each cluster using the ASPCAP values. This process will in some clusters lead to us having fewer stars than the GC specific pipelines, as the ASPCAP

Cluster	[Fe/H]	# of Stars	$\frac{d[C/Fe]}{d\log(g)}$	$\frac{d[N/Fe]}{d\log(g)}$	$\frac{d[C/N]}{d\log(g)}$
NGC 6838 (M71)	-0.78	29	0.10	-0.16	0.25
NGC 6171 (M107)	-1.02	66	0.10	0.14	-0.04
NGC 5904 (M5)	-1.29	214	0.16	-0.34	0.49
NGC 6218 (M12)	-1.37	61	0.32	-0.13	0.45
NGC 5272 (M3)	-1.50	110	0.25	-0.04	0.29
NGC 6205 (M13)	-1.53	97	0.34	-0.19	0.53

Table 7.2: The mixing rates from the Nataf *et al.* (2019) catalogue.

Cluster	[Fe/H]	# of Stars	$\frac{d[C/Fe]}{d\log(g)}$	$\frac{d[N/Fe]}{d\log(g)}$	$\frac{d[C/N]}{d\log(g)}$
M71	-0.78	14	0.16	-0.15	0.30
M107	-1.02	26	0.09	0.03	0.05
M5	-1.29	143	0.29	-0.10	0.38
M12	-1.37	36	0.23	-0.12	0.36
M3	-1.50	93	0.43	-0.31	0.74
M13	-1.53	68	0.43	-0.03	0.45

Table 7.3: Mixing rates using the ASPCAP abundances and surface gravities

pipeline often fails to predict stellar properties for stars of low metallicity. Because of this many of the stars analysed by Masseron *et al.* (2019) or Nataf *et al.* (2019) do not appear in our analysis here. Table 7.3 lists the mixing rates of [C/N], [C/Fe] and [N/Fe], while Table 7.4 compares the mixing rate in each cluster using the ASPCAP, Masseron and Nataf values. Figure 7.3 plots the carbon abundance against surface gravity for all three methods of analysing globular clusters.

From these tables we deduce that broadly there is no consistency between stellar properties determined by the different pipelines. This is consistent with the findings of Nataf *et al.* (2019), which found that there was no overall consensus of the abundances between the different pipelines. Nataf *et al.* (2019) also noted that ASPCAP may underestimate the nitrogen abundance, and compensate for this by overestimating the carbon abundance. Since there is no consensus on mixing rates or abundances in the three different pipelines, it is difficult to reach a consensus on the abundance trends in any single cluster. This highlights a fundamental weakness of this project: we are entirely dependent on the accuracy of the spectroscopic pipeline. The ASPCAP pipeline, which the entire APOGEE catalogue uses, is unable to accurately predict abundances at low metallicities, high masses, or for any other stellar parameter which may be outside its “normal” range. This is a problem for us as we are mostly interested in low metallicity stars, and we are left with the problem where not only do we not have many of these stars in our sample, but the stars we do have may not have accurate abundances

Cluster	[Fe/H]	ASPCAP	Masseron	Nataf
M71	-0.78	0.30	0.37	0.25
M107	-1.02	0.05	-0.38	-0.04
M5	-1.29	0.38	0.36	0.49
M12	-1.37	0.36	—	0.35
M3	-1.50	0.74	0.34	0.39
M13	-1.53	0.45	0.83	0.53

Table 7.4: Comparison between $\frac{d[C/N]}{d \log(g)}$ for the three different analyses of globular clusters in APOGEE.

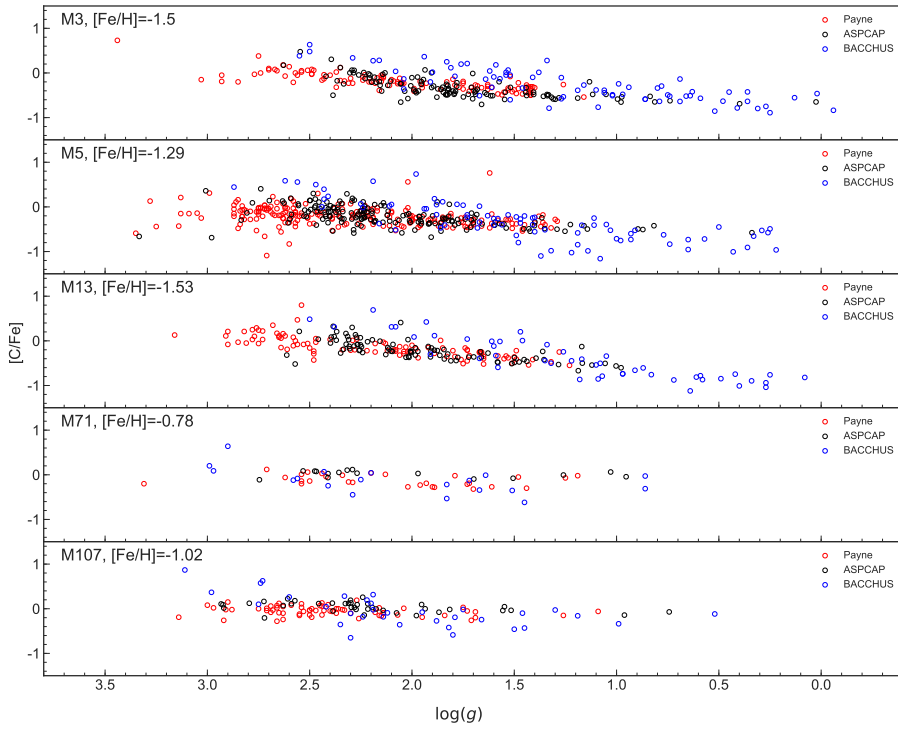


Figure 7.3: Comparison of [C/Fe] vs $\log(g)$ for the three different pipelines to analyse GCs from APOGEE spectra. Black circles are stars with parameters determined by ASPCAP (Holtzman *et al.*, 2018), blue circles are determined using the BACCHUS code (Masseron *et al.*, 2019), and red circles are determined using *The Payne* (Nataf *et al.*, 2019).

and stellar parameters.

[Fe/H]	Mass (M_{\odot})	Mixing	Model Name	$\Delta[\text{C/N}]$	$\Delta \log(g)$	$\frac{d[\text{C/N}]}{d \log(g)}$
0.0	1.00	None	m1.0z014_std	0.00	-3.16	0.00
		Th+Rot	m1.0z014.rot	-0.20	-3.07	0.07
	1.50	None	m1.5z014_std	0.00	-2.60	0.00
		Th+Rot	m1.5z014.rot	-0.04	-2.71	0.02
	2.00	None	m2.0z014_std	0.00	-2.07	0.00
		Th+Rot	m2.0z014.rot	-0.01	-2.02	0.00
-0.56	1.00	None	m1.0z004_std	0.00	-2.43	0.00
		Th+Rot	m1.0z004.rot	-0.46	-2.39	0.19
	1.50	None	m1.5z004_std	0.00	-2.03	0.00
		Th+Rot	m1.5z004.rot	-0.10	-2.12	0.05
	2.00	None	m2.0z004_std	0.00	-1.83	0.00
		Th+Rot	m2.0z004.rot	-0.03	-1.70	0.02
-0.86	1.00	None	m1.0z002_std	0.00	-2.23	0.00
		Th+Rot	m1.0z002.rot	-0.62	-2.33	0.26
	1.50	None	m1.5z002_std	0.00	-2.00	0.00
		Th+Rot	m1.5z002.rot	-0.14	-1.88	0.08
	2.00	None	m2.0z002_std	-0.01	-1.80	0.00
		Th+Rot	m2.0z002.rot	-0.05	-1.69	0.03
-2.16	1.00	None	m1.0z0001_std	0.00	-1.25	0.00
		Th+Rot	m1.0z0001.rot	-0.72	-1.17	0.62
	1.50	None	m1.5z0001_std	0.00	-0.80	0.00
		Th+Rot	m1.5z0001.rot	-0.07	-0.76	0.09
	2.00	None	m2.0z0001_std	0.00	-0.28	0.00
		Th+Rot	m2.0z0001.rot	0.00	0.00	0.00

Table 7.5: Mixing rates for 24 of the Lagarde *et al.* (2012) models with thermohaline and rotational mixing (Th+Rot) and without any deep mixing (None). The file name of each model used is listed as well.

7.2 Comparison with Theoretical Predictions

To compare our observations to theoretical predictions of thermohaline mixing, we use the models developed by Lagarde *et al.* (2012). These models use an implicit Lagrangian stellar evolution code called STAREVOL (See Siess *et al.* 2000; Palacios *et al.* 2003, 2006; Decressin *et al.* 2009 for details on previous versions of the stellar evolution code). These models treat deep mixing as diffusive thermohaline mixing, and use the mixing rates that were advocated for in Charbonnel and Zahn (2007). We choose these models as they include evolution with and without the effect of thermohaline mixing over a range of different masses and metallicities. While the original models presented in Lagarde *et al.* (2012) had separate simulations of no mixing, rotation induced mixing and thermohaline mixing, only the models with no mixing and the models with both thermohaline and rotation induced mixing have been made available to us.

The STAREVOL models provide us with theoretical values for a wide variety of stellar parameters including luminosity, surface and core temperatures and densities, surface gravity, mass loss and asteroseismic parameters (ν_{\max} and $\Delta\nu$). It also includes the mass fraction of a wide variety of elements at the core and surface, including for our purposes ^{12}C and ^{14}N . To convert between mass fractions and chemical abundance ratios we start by using the fact that the number density can be defined as $N_X = \frac{X_X}{M_X} \rho N_A$ where N_X , X_X and M_X are the number density, mass fraction and atomic mass of element X respectively, and ρ and N_A are the density and the Avogadro constant. These last two will cancel out when calculating abundance ratios. Using the general expression for the abundance ratios defined in *Section 2.2.2* we arrive at equation 7.2 where X_A and X_B are the mass fractions of elements A and B, and M_A and M_B are the atomic mass of elements A and B. For the solar abundances we use the values presented in Asplund *et al.* (2009), which are the most accurate to date. The solar abundance values are given in Asplund as $\log \epsilon_A = \log(N_A/N_H) + 12$ for element A. We also use the mass fractions for the sun determined in this paper with X=0.7381, Y=0.2485, Z=0.0134, where X, Y and Z are the mass fractions of hydrogen, helium and all metals respectively. Using these values and expanding some terms using log laws we define the new equation 7.3. In this equation X_H refers to the number density of ^1H , which of course has an atomic mass of 1. The STAREVOL models do not contain the mass fractions for iron however, so we replace these terms with the total metallicity mass fraction, as we expect the ratios of the iron abundance and total metallicity to be the same. This substitution finally gives us equation 7.4.

$$[\text{A}/\text{B}] = \log\left(\frac{X_A/M_A}{X_B/M_B}\right)_* - \log\left(\frac{X_A/M_A}{X_B/M_B}\right)_\odot \quad (7.2)$$

$$[\text{A}/\text{Fe}] = \log\left(\frac{X_A/M_A}{X_H}\right)_* - \log \epsilon_A + 12 - \log\left(\frac{X_{\text{Fe},*}}{X_{\text{Fe},\odot}}\right) + \log\left(\frac{X_{\text{H},*}}{X_{\text{H},\odot}}\right) \quad (7.3)$$

$$[\text{A}/\text{Fe}] = \log\left(\frac{X_A/M_A}{X_H}\right)_* - \log \epsilon_A + 12 - \log\left(\frac{Z_*}{Z_\odot}\right) + \log\left(\frac{X_{\text{H},*}}{X_{\text{H},\odot}}\right) \quad (7.4)$$

Figure 7.4 plots the [C/N] ratio against surface gravity for both the Lagarde models and APOGEE dataset. To compare the models to our data we split the APOGEE dataset into 12 subsets with metallicity ranges of $0.25 \geq [\text{Fe}/\text{H}] > -0.25$, $-0.25 \geq [\text{Fe}/\text{H}] > -0.65$, $-0.65 \geq [\text{Fe}/\text{H}] > -1.00$ and $-1.80 \geq [\text{Fe}/\text{H}]$, and mass ranges of $0.75 \leq M/M_\odot < 1.25$, $1.25 \leq M/M_\odot < 1.75$ and $1.75 \leq M/M_\odot$. These are similar to the selections used in *Section 6.2*, but are designed to be centred around the properties of the Lagarde models we use. For each selection of mass and metallicity we plot both the model with no mixing and with both thermohaline and rotation

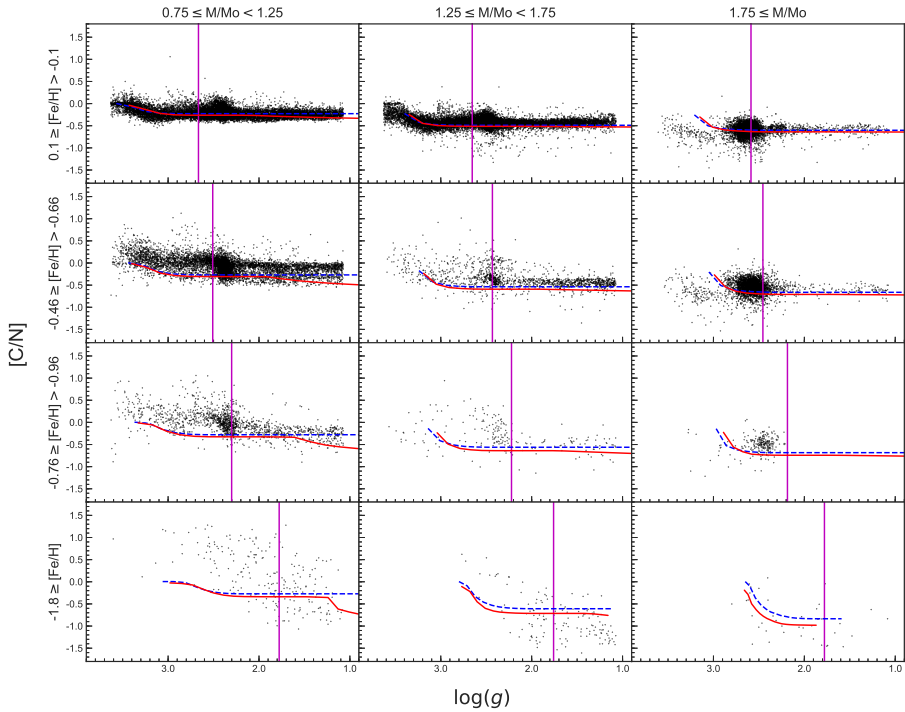


Figure 7.4: APOGEE carbon-nitrogen abundance ratio plotted against surface gravity, grouped by both mass and metallicity. The blue dashed line is the predicted carbon-nitrogen ratio on the RGB with no additional mixing. The red solid line is the predicted carbon-nitrogen ratio with both thermo-haline and rotation induced mixing. Both models were produced by Lagarde *et al.* (2012). The vertical magenta line indicates the beginning of where we predict the RGBb to occur, based on the isochrones we used in *Section 6.1*.

induced mixing. The models have masses of $1.0M_{\odot}$, $1.5M_{\odot}$ and $2.0M_{\odot}$, with metallicities of $[Fe/H] = 0.00, -0.56, -0.86$ and -2.16 . Because of the large range of each mass-metallicity bin we expect a large degree of scatter, but the general trends should follow the predictions made by Lagarde *et al.* (2012).

Comparison between the Lagarde models and APOGEE data yields some interesting observations. Firstly we note that the beginning of the mixing predicted in the Lagarde models does not match the observed RGBb and onset of carbon depletion in the data. The Lagarde models do not have the resolution to observe the luminosity bump directly, which makes it difficult to determine whether they are predicting the mixing onset occurring later in evolution, or whether they predict that the luminosity bump should occur at lower surface gravity. Another possibility is that the ASPCAP pipeline is unable to properly determine the surface gravity of stars in this stage of

evolution. To test this idea we compare the observed location of the RGBb to the one found in the isochrones developed by Dotter *et al.* (2008) that we used in the previous section. The onset of the mixing in the Lagarde models does not match the predictions of the RGBb locations from the isochrones, which tend to predict the bump at lower surface gravity than we observe in APOGEE.

Additionally we note that the Lagarde models are quite poor indicators of both extra-mixing and change in [C/N] due to FDU, with neither trend (the former occurring at high- $\log(g)$) matching the trends observed in the APOGEE data. In the high-metallicity $0.25 \geq [\text{Fe}/\text{H}] > -0.65$ models the FDU and APOGEE data fit well for the low mass stars ($M < 1.75M_{\odot}$), but they do not match accurately for high-mass or low metallicity data. Indeed, the no-mixing model more often fits our data set better than the rotation + thermohaline mixing model. This however is more likely due to the models' overprediction of abundance changes during FDU, causing a reduction in [C/N] abundances before the RGB.

As we did for the APOGEE data, we can express the mixing rate as $d[\text{C}/\text{N}]/d\log(g)$ for each mass and metallicity. For this we use the location of the RGBb we determined with the isochrones in *Section 6.1*, and find the difference in the [C/N] ratio and surface gravity from this point to the tip of the RGBb. Table 7.5 lists the mixing rates for 24 of the models made by Lagarde *et al.* (2012), listing the mass, metallicity and change in [C/N] and $\log(g)$ for each model. We note that for the model with mass $M = 2.0M_{\odot}$ and $[\text{Fe}/\text{H}] = -2.16$ we note that both the mixing and non-mixing models have similar changes in their [C/N] abundance, which suggests that this change is due to FDU effects rather than thermohaline mixing.

Additionally it appears that the initial [C/N] ratio for APOGEE field stars is often higher than the initial values used for the Lagarde models, particularly at lower metallicities. If this is the only difference between the Lagarde models and the APOGEE data then the mixing rates should in theory be the same. A comparison between the APOGEE mixing rates determined in *Section 6.2* and those predicted by Lagarde are given in Table 7.6. From here we see that the Lagarde models typically overestimate the observed strength of the mixing, except for stars in the range $-1.80 \geq [\text{Fe}/\text{H}]$, $0.75 \leq M/M_{\odot} < 1.25$ and $1.25 \leq M/M_{\odot} < 1.75$, where the observed mixing rate is comparable to what the model predicts. It should be noted that this selection of APOGEE data contains very few stars, so the mixing rate could easily be skewed. The mixing rates determined here for the APOGEE data were determined using the same method as in *Section 6.2*, using the selection criteria such that the mass is with $0.25M_{\odot}$ of the models mass (the highest mass selection has no upper bound due to the comparatively few stars in this mass range) and the metallicity is within 0.1 dex of the models for the models of $[\text{Fe}/\text{H}] = 0.00, -0.56$ and -0.86 . For the lowest metallicity model ($[\text{Fe}/\text{H}] = -2.16$) we select all stars with metallicities $[\text{Fe}/\text{H}] \leq -1.80$,

Metallicity	Mass Range	APOGEE	Lagarde
$0.10 \geq [\text{Fe}/\text{H}] > -0.10$ (0.00)	$0.75 \leq M/M_{\odot} < 1.25, (1.00)$	0.03	0.07
	$1.25 \leq M/M_{\odot} < 1.75, (1.50)$	0.02	0.02
	$1.75 \leq M/M_{\odot}, (2.00)$	0.02	0.01
$-0.46 \geq [\text{Fe}/\text{H}] > -0.66$ (-0.56)	$0.75 \leq M/M_{\odot} < 1.25, (1.00)$	0.15	0.19
	$1.25 \leq M/M_{\odot} < 1.75, (1.50)$	0.13	0.05
	$1.75 \leq M/M_{\odot}, (2.00)$	0.06	0.02
$-0.76 \geq [\text{Fe}/\text{H}] > -0.96$ (-0.86)	$0.75 \leq M/M_{\odot} < 1.25, (1.00)$	0.26	0.30
	$1.25 \leq M/M_{\odot} < 1.75, (1.50)$	0.29	0.09
	$1.75 \leq M/M_{\odot}, (2.00)$	0.00	0.02
$-1.80 \geq [\text{Fe}/\text{H}]$ (-2.16)	$0.75 \leq M/M_{\odot} < 1.25, (1.00)$	0.47	0.69
	$1.25 \leq M/M_{\odot} < 1.75, (1.50)$	0.56	0.12
	$1.75 \leq M/M_{\odot}, (2.00)$	0.00	0.00

Table 7.6: $\frac{d[\text{C}/\text{N}]}{d \log(g)}$ for the APOGEE field stars and models developed by Lagarde *et al.* (2012). The metallicity and mass ranges are the ranges used for the selection of APOGEE stars, the numbers in brackets are the mass and metallicity of the Lagarde model.

[Fe/H]	$d[\text{C}/\text{N}]/d \log(g)$
-1.0	0.08
-1.2	0.29
-1.4	0.25
-1.6	0.35

Table 7.7: Mixing rates at different metallicity ranges in APOGEE as found by (Shetrone *et al.*, 2019).

as there are relatively few stars in this metallicity range.

7.3 Comparison to the Literature

An accurate comparison to previous work on deep mixing from the literature is difficult to accomplish due to systematic differences between surveys and spectroscopic pipelines. However comparison to previous work that also used APOGEE, such as Shetrone *et al.* (2019) is possible. A brief summary of this paper was presented in *Section 3.1.2*, and here we will just go over some of the results they found in their analysis. Firstly it is important to remember that there was no rigorous mass selection in this paper. Instead only stars with $[\alpha/\text{M}] > 0.14$ were selected, as most stars in this mass range will have masses $M \approx 1.1M_{\odot}$.

Figure 7.5 plots histograms of the predicted masses, metallicity, carbon and nitrogen abundances of the stars with the criteria used by Shetrone *et al.* (2019). From subplot a) of this figure we see that while their cutoff in

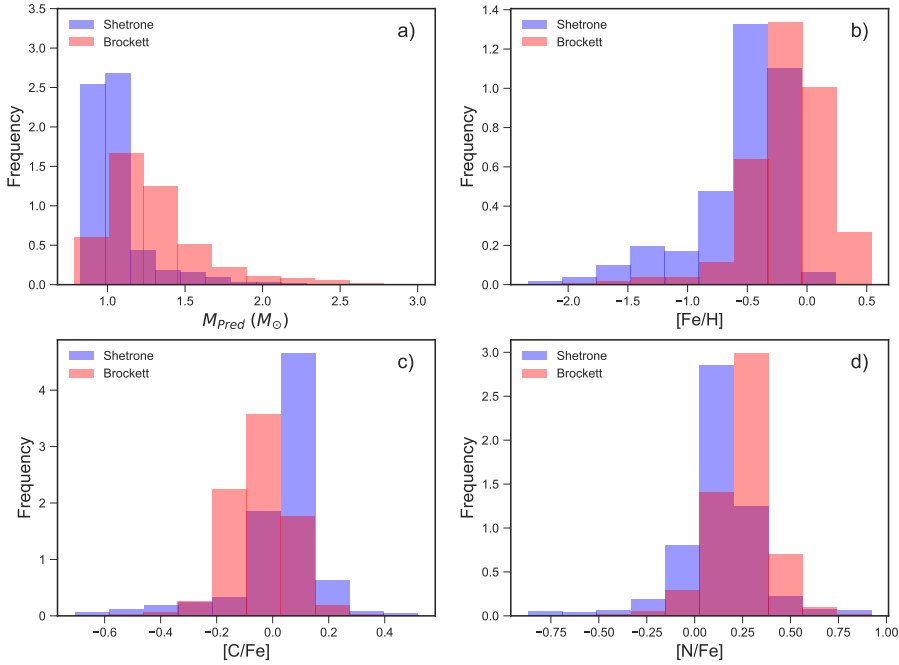


Figure 7.5: Histograms of predicted mass (M_{Pred}), metallicity, carbon and nitrogen abundances for the full APOGEE set used in this project, and the subset analysed in Shetrone *et al.* (2019). For each subplot the blue histogram is the subset used in Shetrone *et al.* (2019), and the red histogram is the APOGEE catalogue with mass predictions we calculated, labelled as “Brockett”.

alpha abundance does select mostly low mass stars, there are still significant numbers of stars with low to intermediate mass ($1.2 \leq M/M_{\odot} \leq 1.6$) in this dataset, and fewer but not inconsequential numbers of stars with masses greater than that. Subplot b) compares the metallicity between the two selections, and we note that the selection from Shetrone *et al.* (2019) has a tendency to select slightly more lower metallicity stars than are in proportion to the full APOGEE dataset. The carbon and nitrogen abundances of the stars selected however tend to be higher and lower respectively for the subset compared to the full dataset. This is likely due to higher mass stars having larger abundance changes during the FDU.

The mixing rates found in Shetrone *et al.* (2019) are listed in Table 7.7. A much finer selection in metallicity is used in this paper, but even so it is evident that their observed mixing rates are much lower than our observations at similar masses and metallicities. For a star with metallicity in the range of $-1.25 \leq [Fe/H] < -1.00$ and mass within the range ($1.00 \leq M/M_{\odot} < 1.25$) we observe a mixing rate of $d[C/N]/d\log(g) = 0.45$, nearly double what (Shetrone *et al.*, 2019) find at similar mass and metallicity. Examining the

Lagarde predictions we see that they agree well with the Shetrone observations. An analysis of the mixing rate over smaller metallicity ranges using our catalogue in the range of $-1.50 \leq [\text{Fe}/\text{H}] < -1.00$ could be beneficial, but the mixing rate measurement would be susceptible to outliers in the data since there would be fewer stars per selection. Ultimately while we lose precision by using large ranges for our metallicity bins, we prevent overfitting at low metallicities which overall should make our results more accurate.

CHAPTER 8

Conclusions

Throughout this project we have accomplished a number of tasks we set out to complete:

1. Used asteroseismology data to predict masses for stars with only spectroscopic data.
2. Analysed the deep mixing rate at different masses and metallicities.
3. Compared mixing rates in field stars to globular clusters of similar masses and metallicities.
4. Compared observational data to theoretical predictions of “thermohaline mixing”, the currently accepted explanation for the deep mixing phenomenon.

Our predictions for mass are accurate within $0.2M_{\odot}$ for star with masses $M < 1.5M_{\odot}$ and within $0.32M_{\odot}$ for stars with masses $M \geq 1.5M_{\odot}$. While the method we use is limited in the scope of its predictions, the accuracy within its bounds is impressive. It is unable to predict masses for stars that exist outside the scope of the training set, which includes stars of low metallicity ($[\text{Fe}/\text{H}] < 2.3$), low surface gravity ($\log(g) < 1.0$) and high mass ($M > 2.2M_{\odot}$). Using these masses we were able to find the mixing rate ($d[\text{C}/\text{N}]/d\log(g)$) for 25 different selections of mass and metallicity. The mixing rates we determine demonstrate the overall trends of increasing with decreasing metallicity and mass, but the exact mixing rates are susceptible to errors that occur when there are relatively few stars in the mass and metallicity selection.

The comparison of our mixing rates to theoretical work by Lagarde *et al.* (2012) further compounds the inaccuracies due to low numbers of low metallicity stars. Despite this it is evident that these models are unable to reproduce the abundance trends we observe in APOGEE. The onset of mixing occurs much later than we observe in our data, and the extent of the mixing is overestimated in higher metallicity stars, while it appears to underestimate mixing in higher mass stars.

8.1 Future Work

This project leaves many options for future work on the topic. In terms of updating the fundamental aspects of the project we would like to improve:

1. Larger dataset of stars with masses determined by asteroseismology.
2. More robust spectroscopic pipelines for surveys like APOGEE, which improve accuracy at low metallicities and high masses.
3. Advanced theoretical predictions to compare to observational data.

Larger asteroseismology dataset adds two benefits to this project: firstly the masses determined via seismology can be used to look at mixing rates directly and secondly a larger asteroseismology dataset will improve the accuracy of any machine learning techniques that we use to predict the masses of stars without seismology. The more robust spectroscopic pipeline will improve the accuracy of abundances and other stellar parameters. This will be particularly beneficial at high masses and low metallicities, which we noted the pipelines typically perform poorly on. More advanced theoretical predictions will allow for a) better comparison to observational work and b) could be used to enhance the accuracy of spectroscopic pipelines. A larger parameter space within the models like STAREVOL that have the resolution from features such as the luminosity bump would aid in determining how well they match observations. Additionally covering a larger range in metallicities would be helpful for future work.

On a smaller scale using the current data that is available future work in this topic could include:

1. More sophisticated machine learning techniques to predict masses.
2. Comparison to other theoretical models, both other models of thermo-haline and other mixing possibilities (such as magnetism and rotation).
3. Predicting ages to APOGEE stars, as well as masses.
4. Using similar methods in other spectroscopic surveys, and comparing observations

More sophisticated machine learning techniques is the easiest way to improve the certainty in our mixing rates. This will minimise cross contamination between our mass selections, and allow us to use smaller mass selection criteria when determining bins for analysis, which will allow for a more accurate assessment of the mass dependence of deep mixing. Additionally using a method that is able to predict outside of the parameter space of the training set will mean we can predict masses for stars with surface gravities $\log(g) < 1$ and metallicity $[\text{Fe}/\text{H}] < 2$ accurately. A comparison to other theoretical mixing models would also be beneficial as it will allow us to assess the accuracy of thermohaline mixing when compared to other options. Magnetism and rotation induced mixing have been previously proposed as potential candidates for deep mixing with some success, so a comparison between these three potential sources of mixing with observational data to compare to would bring a lot of insight to the accuracy of each model.

Predicting ages of APOGEE stars was not attempted in this project for a variety of reasons, including time limitations, and was decided that it would not likely bring any new information out of the project. Nevertheless an examination of the mixing rate as $d[\text{C}/\text{N}]/dt$ would allow for better comparison of the mixing rates, as more massive stars will evolve more rapidly along the giant branch, so the mixing rate could be more rapid than predicted using surface gravity. And lastly a similar analysis in other large spectroscopic surveys would be beneficial. APOGEE was chosen due to the accuracy of its carbon abundance (which some other surveys such as GALAH lack), but other surveys with accurate carbon abundance should be considered for future projects.

APPENDIX A

Additional Figures & Tables

This appendix contains figures and tables of data that isn't required for the thesis, but may be beneficial for the reader. Included are the plots of [C/Fe] Vs surface gravity and [N/Fe] Vs surface gravity, as well as the relevant changes in abundances for each selection of mass and metallicity, The nitrogen abundance for globular clusters in Masseron *et al.* (2019) plotted against surface gravity, and a comparison of [N/Fe] vs $\log(g)$ for all three analyses of globular clusters in APOGEE.

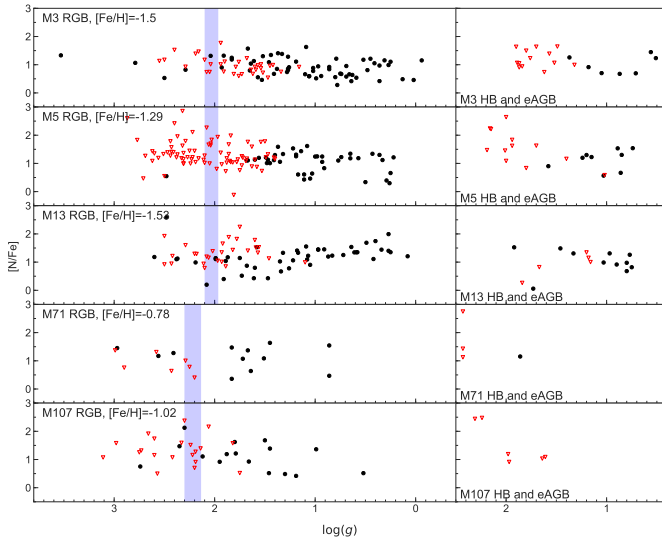


Figure A.1: [N/Fe] abundances for M3, M5, M13, M71 and M107 on the RGB (left plots) and the HB and early AGB (Right Plots). Black dots indicate stars with a determined [N/Fe] abundance, while red triangles indicate stars with only an upper limit for [N/Fe]. The blue shaded region indicate the mean $\log(g)$ where the RGBb occurs in an isochrone of similar metallicity and age.

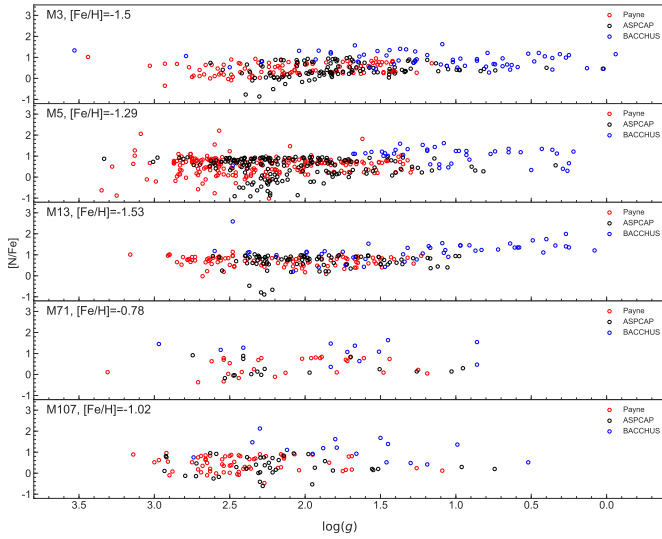


Figure A.2: Comparison of [C/Fe] vs $\log(g)$ for the three different pipelines to analyse GCs from APOGEE spectra. Black circles are stars with parameters determined by ASPCAP (Holtzman *et al.*, 2018), blue circles are determined using the BACCHUS code (Masseron *et al.*, 2019), and red circles are determined using *The Payne* (Nataf *et al.*, 2019).

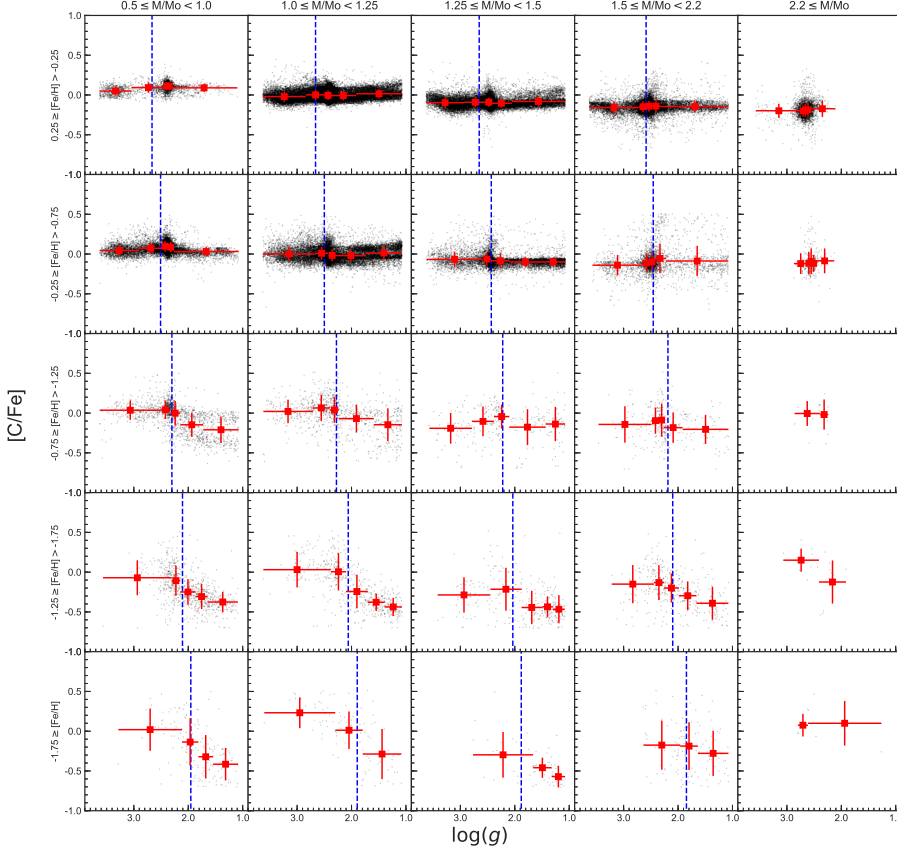


Figure A.3: [C/Fe] abundances for APOGEE stars, selected by their mass and metallicity.

Metallicity	Mass	$\Delta[\text{C}/\text{Fe}]$	$\Delta \log(g)$	$\frac{d[\text{C}/\text{Fe}]}{d \log(g)}$
$0.25 \geq [\text{Fe}/\text{H}] > -0.25$	$M/M_{\odot} < 1.00$ $1.00 \leq M/M_{\odot} < 1.25$ $1.25 \leq M/M_{\odot} < 1.5$ $1.50 \leq M/M_{\odot} < 2.2$	-0.00 0.01 0.01 -0.01	-1.02 -1.16 -1.16 -0.84	0.00 -0.01 -0.01 0.01
$-0.25 \geq [\text{Fe}/\text{H}] > -0.75$	$M/M_{\odot} < 1.00$ $1.00 \leq M/M_{\odot} < 1.25$ $1.25 \leq M/M_{\odot} < 1.5$ $1.50 \leq M/M_{\odot} < 2.2$	-0.07 0.00 -0.03 0.01	-0.76 -1.14 -1.22 -0.83	0.09 -0.00 0.03 -0.01
$-0.75 \geq [\text{Fe}/\text{H}] > -1.25$	$M/M_{\odot} < 1.00$ $1.00 \leq M/M_{\odot} < 1.25$ $1.25 \leq M/M_{\odot} < 1.5$ $1.50 \leq M/M_{\odot} < 2.2$	-0.21 -0.19 -0.09 -0.02	-0.84 -0.98 -0.99 -0.60	0.25 0.19 0.09 0.04
$-1.25 \geq [\text{Fe}/\text{H}] > -1.75$	$M/M_{\odot} < 1.00$ $1.00 \leq M/M_{\odot} < 1.25$ $1.25 \leq M/M_{\odot} < 1.5$ $1.50 \leq M/M_{\odot} < 2.2$	-0.13 -0.19 -0.25 -0.19	-0.64 -0.67 -0.97 -0.75	0.20 0.29 0.26 0.26
$-1.75 \geq [\text{Fe}/\text{H}] > -2.50$	$M/M_{\odot} < 1.00$ $1.00 \leq M/M_{\odot} < 1.25$ $1.25 \leq M/M_{\odot} < 1.5$ $1.50 \leq M/M_{\odot} < 2.2$	-0.28 -0.30 -0.27 -0.09	-0.65 -0.61 -1.02 -0.44	0.43 0.49 0.27 0.21

Table A.1: Change in [C/Fe] abundance for different selections of mass and metallicity.

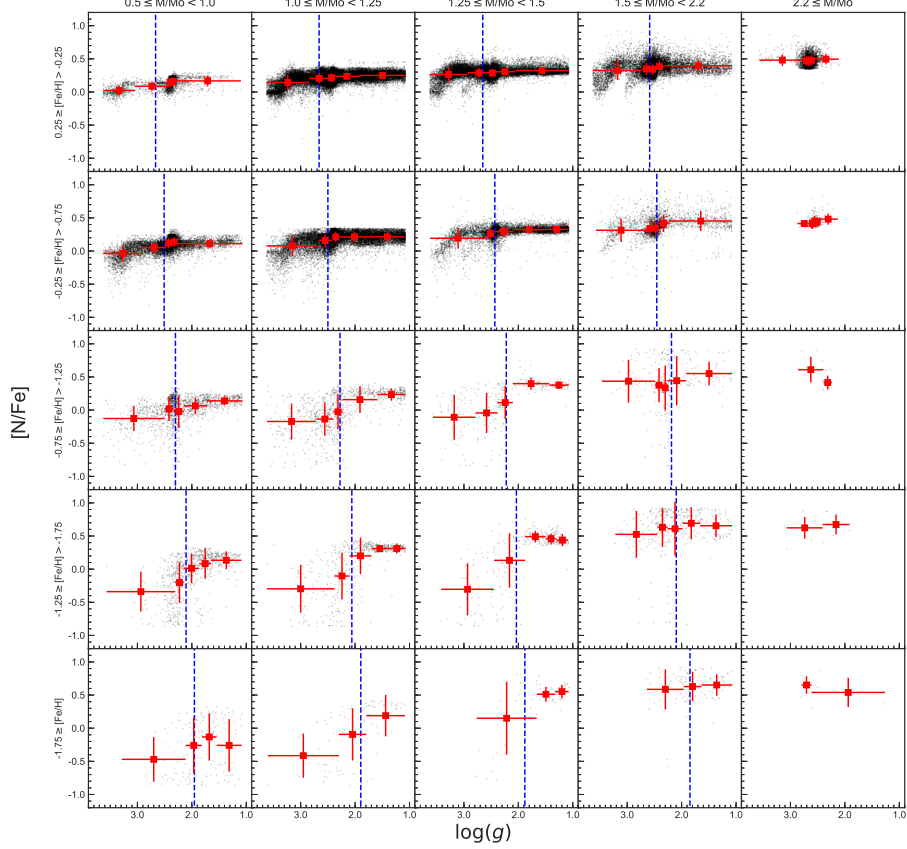


Figure A.4: [N/Fe] abundances for APOGEE stars, selected by their mass and metallicity.

Metallicity	Mass	$\Delta[N/Fe]$	$\Delta \log(g)$	$\frac{d[N/Fe]}{d \log(g)}$
$0.25 \geq [\text{Fe}/\text{H}] > -0.25$	$M/M_{\odot} < 1.00$ $1.00 \leq M/M_{\odot} < 1.25$ $1.25 \leq M/M_{\odot} < 1.5$ $1.50 \leq M/M_{\odot} < 2.2$	0.08 0.04 0.03 0.05	-1.02 -1.16 -1.16 -0.84	-0.08 -0.04 -0.03 -0.06
$-0.25 \geq [\text{Fe}/\text{H}] > -0.75$	$M/M_{\odot} < 1.00$ $1.00 \leq M/M_{\odot} < 1.25$ $1.25 \leq M/M_{\odot} < 1.5$ $1.50 \leq M/M_{\odot} < 2.2$	-0.01 0.05 0.06 0.11	-0.76 -1.14 -1.22 -0.83	0.01 -0.05 -0.05 -0.13
$-0.75 \geq [\text{Fe}/\text{H}] > -1.25$	$M/M_{\odot} < 1.00$ $1.00 \leq M/M_{\odot} < 1.25$ $1.25 \leq M/M_{\odot} < 1.5$ $1.50 \leq M/M_{\odot} < 2.2$	0.16 0.26 0.26 0.11	-0.84 -0.98 -0.99 -0.60	-0.19 -0.27 -0.27 -0.18
$-1.25 \geq [\text{Fe}/\text{H}] > -1.75$	$M/M_{\odot} < 1.00$ $1.00 \leq M/M_{\odot} < 1.25$ $1.25 \leq M/M_{\odot} < 1.5$ $1.50 \leq M/M_{\odot} < 2.2$	0.12 0.11 0.31 0.05	-0.64 -0.67 -0.97 -0.75	-0.19 -0.17 -0.31 -0.06
$-1.75 \geq [\text{Fe}/\text{H}] > -2.50$	$M/M_{\odot} < 1.00$ $1.00 \leq M/M_{\odot} < 1.25$ $1.25 \leq M/M_{\odot} < 1.5$ $1.50 \leq M/M_{\odot} < 2.2$	0.00 0.28 0.40 0.02	-0.65 -0.61 -1.02 -0.44	-0.00 -0.46 -0.40 -0.05

Table A.2: Change in [N/Fe] abundance for different selections of mass and metallicity.

APPENDIX B

Python Code

B.1 Mass Prediction Code

```
# -*- coding: utf-8 -*-
"""
Mass_predictions.py
Create a random forest regressor (RFR) to predict the masses of
stars using their surface gravity, temperature, and composition.
We use the masses determined by asteroseismology from the
APOKASC catalogue as a training set, then quantify the
uncertainty in our predictions by fitting a skewed-normal
distribution to the errors in specific mass ranges.
We also produce plots of predicted mass vs asteroseismic mass,
the histograms of the errors in each mass range, and a table with
the properties of the skewed-normal distributions.

@author: Christopher J. Brockett, November 2019
"""

# Import Relevant python packages
import numpy as np # for number handling
import pandas as pd # for table/data management
import matplotlib.pyplot as plt # produce plots
from scipy import stats # for statistics
from astropy.table import Table # for table/data management
from matplotlib.ticker import (MultipleLocator,
                               FormatStrFormatter)
# for styling axis ticks on plots
from sklearn.model_selection import train_test_split as tts
# Package to split data into training and test sets
from sklearn.ensemble import RandomForestRegressor
```

```

#import RF regression model
from sklearn.metrics import mean_squared_error
# calculate MSE of regression data
from astropy.io import ascii as io # to print table of data
import seaborn as sb # style package for plots
sb.set_style("white") # white background for plots
sb.set_style("ticks") # add ticks to axes

# load APOKASC data file
apk = Table.read('Apogee_Data/APOKASC_APOGEE_Refined.fits')

# Features we train the model on: surface temp, metallicity,
# surface gravity [C/Fe], [N/Fe], [O/Fe] and alpha abundance
features = ['TEFF', 'FE_H', 'LOGG', 'C_FE', 'N_FE', 'O_FE',
            'ALPHA_M']
apk.sort(keys='M_cor_') # sort table wrt masses

X = apk[features] # subset of the APOKASC data containing only
# relevant features
X = X.to_pandas() # convert to a pandas dataframe, necessary for
# the regression model
Y = apk['M_cor_'] #list of the asteroseismic masses

# Split the dataset into X_train, X_test, y_train, y_test
# Use a training dataset size of 50%
X_train, X_test, y_train, y_test = tts(X, Y, train_size = 0.5)

# Initialise the RFR with 200 estimators
rf1 = RandomForestRegressor(n_estimators=200)
rf1.fit(X_train, y_train) # fit the regressor to training data
y_pred = rf1.predict(X_test) # predict on test data
score = np.sqrt(mean_squared_error(y_test,y_pred))
# calculate MSE of the predicted data
corr = np.corrcoef(y_test, y_pred)[0][1] #calculate the
# correlation coefficient between predictions and asteroseismic
# data
print('RF_RMSE: {:.3f}'.format(score)) #print MSE
print('RF_corr: {:.3f}'.format(corr)) # print correlation

X_new = X.copy() # Copy features subset of APOKASC
X_new['M_pred'] = rf1.predict(X) # add new column with predicted
# mass for whole catalogue

# create a new dataframe with the predictions and test sets
dat = pd.DataFrame(data = {'y_test': y_test.tolist(),
                           'y_pred': y_pred}, index=None)
dat_sort = dat.sort_values('y_pred') #sort data wrt the
# predicted date

```

```

# find points where we can split the data into regions with
# predicted mass M<1, 1<M<1.25, 1.25<M<1.5, 1.5<M<2.2, 2.2<M
splits=[np.where(dat_sort.y_pred>1.0)[0][0],
        np.where(dat_sort.y_pred>1.25)[0][0],
        np.where(dat_sort.y_pred>1.5)[0][0],
        np.where(dat_sort.y_pred>1.75)[0][0],
        np.where(dat_sort.y_pred>2.2)[0][0]]

# split the predicted mass into those subsets
l = np.split(dat_sort.y_pred, splits)
# split asteroseismic mass into those subsets
o = np.split(dat_sort.y_test, splits)

# set empty arrays for skewnorm parameters a, loc and scale, as
# well as properties of each distribution including lower and
# upper 68% confidence intervals, mean, variance, skew, kurtosis
# and median
a, loc, scale, u68, l68, mean, var, skew, kurt, med = ([], [], [],
                                                       [], [],
                                                       [], [],
                                                       [], [],
                                                       [], [])

# for each subset we fit a skewed-normal distribution to the
# difference between asteroseismic mass and predicted mass.
# From this distribution we can calculate uncertainties in the
# prediction (lower and upper 68% confidence intervals),
# as well as properties of the distribution itself.
for k in range(len(l)):
    data = o[k]-l[k] # Difference between asteroseismic and
    # predicted mass
    # estimate parameters from sample
    ae, loce, scalee = stats.skewnorm.fit(data) #fit skewed-
    # normal distribution to the data
    # Append distribution paramaters a, loc and scale
    a.append(ae)
    loc.append(loce)
    scale.append(scalee)
    # calculate the upper and lower bounds of the 68% confidence
    # interval
    lo, up = stats.skewnorm.interval(0.68, ae, loc=loce,
                                    scale=scalee)
    # Append to list
    l68.append(lo)
    u68.append(up)
    #Calculate mean, variance, skew and kurtosis
    mvsks = stats.skewnorm.stats(ae, loc=loce, scale=scalee,
                                 moments='mvsks')
    # Append to lists

```

```

mean.append(mvsk[0].item())
var.append(mvsk[1].item())
skew.append(mvsk[2].item())
kurt.append(mvsk[3].item())
# Calculate and append median
med.append(stats.skewnorm.median(ae, loc=loce, scale=scalee))

# Create a table with values for each distribution

ME = Table([[round(elem, 3) for elem in mean],
            [round(elem, 3) for elem in var],
            [round(elem, 3) for elem in skew],
            [round(elem, 3) for elem in kurt],
            [round(elem, 3) for elem in med],
            [round(elem, 3) for elem in l168],
            [round(elem, 3) for elem in u168]],
            names=['mean', 'var', 'skew', 'kurt', 'med', 'l168',
                   'u168'])
# Print table in 'LATEX' format
io.write(ME, format='latex')

f, ax = plt.subplots(1,1,figsize=(12,9)) # Create a figure
# environment
for k in range(len(l)):
    ax.scatter(l[k], o[k], s=0.1, c='k') # For each mass range
    # make a scatter
    # plot of the predicted mass against the asteroseismic mass
    # Add blue dashed line for confidence intervals
    ax.plot(l[k], l[k]+l168[k], 'b--')
    ax.plot(l[k], l[k]+u168[k], 'b--')
x = np.linspace(min(l[0]), max(l[k]), 100) # Make array of evenly
# spaced values
# spanning the range of the dataset
ax.plot(x,x,'r--') # Make a plot of y=x representing a 100%
# accurate prediction

# Change style and location of ticks on axes
ax.tick_params(axis='both', which='both', direction='in')
ax.yaxis.set_major_locator(MultipleLocator(0.5))
ax.yaxis.set_major_formatter(FormatStrFormatter('%.0.1f'))
ax.yaxis.set_minor_locator(MultipleLocator(0.1))
ax.xaxis.set_major_locator(MultipleLocator(0.5))
ax.xaxis.set_major_formatter(FormatStrFormatter('%.0.1f'))
ax.xaxis.set_minor_locator(MultipleLocator(0.1))
f.text(0.52, 0.08, 'Predicted_Mass_(M_{\odot})', ha='center',
       va='center',
       fontsize=16) # Add text for xlabel
f.text(0.08, 0.5, 'Asteroseismic_Mass_(M_{\odot})',
       ha='center', va='center', rotation='vertical',

```

```

    fontsize=16) # Add text for ylabel
# Save figure as an eps file
plt.savefig('Plots/APOKASC_Predictions.eps', bbox_inches='tight',
            pad_inches=0.1, format='eps', dpi=1200)

# Create a new figure with 6 subplots
f, ax = plt.subplots(3,2, figsize=(18,15), sharex=True,
                     sharey=True)
masses = [1.00, 1.25, 1.50, 1.75, 2.20] # array of edges of the
# mass range
i, h = 0, 0 # Set counter variables i and h to 0
for k in range(len(l)):
    data = o[k]-l[k] # Calculate difference between
    # asteroseismic and predicted mass
    # Plot a normalised histogram of the data in each mass
    # selection
    ax[i,h].hist(data, bins=100, density=True, alpha=0.6,
                  color='b')
    xmin, xmax = plt.xlim() #find span of the x-axis
    x = np.linspace(xmin, xmax, 200) #an array that spans the
    # data set
    # Plot the pdf of the distribution fitted to the data
    p = stats.skewnorm.pdf(x,a[k], loc[k], scale[k])
    ax[i,h].plot(x, p, 'k', linewidth=2)
    if k==0: # Add annotation of the mass range of data
        ax[i,h].annotate('$M/M_{\odot} < '+str(masses[k]),
                         xy=(0.02,0.95),
                         xycoords='axes fraction', fontsize=16,
                         horizontalalignment='left',
                         verticalalignment='top')
    elif k==len(l)-1:
        ax[i,h].annotate(str(masses[k-1])+' \leq M/M_{\odot} $',
                         xy=(0.02,0.95),
                         xycoords='axes fraction', fontsize=16,
                         horizontalalignment='left',
                         verticalalignment='top')
    else:
        ax[i,h].annotate(str(masses[k-1])+' \leq M/M_{\odot} < '+
                         str(masses[k]),
                         xy=(0.02,0.95),
                         xycoords='axes fraction',
                         fontsize=16, horizontalalignment='left',
                         verticalalignment='top')
    # Increase relevant counter
    if h == 1:
        i += 1
        h = 0
    else:
        h += 1

```

```
# Remove space between subplots
f.subplots_adjust(hspace=0)
f.subplots_adjust(wspace=0)
f.text(0.52, 0.08, '$M_{\text{Astero}} - M_{\text{Pred}}; (M_{\dot{\text{O}}})$', 
       ha='center', va='center', fontsize=16) # Add xlabel
f.text(0.08, 0.5, 'Frequency', ha='center', va='center',
       rotation='vertical', fontsize=16) # Add ylabel
plt.savefig('Plots/Distributions.eps', bbox_inches='tight',
            pad_inches=0, format='eps', dpi=1200)
# Save figure as eps file
```

B.2 Determine Mixing Rates

```
# -*- coding: utf-8 -*-
"""
Mixing_rates.py
Determine the rate at mixing occurs on the red giant branch. Use the
    ↪ masses
determined by the RFR (see Mass_predictions.py) as the input. The
    ↪ APOGEE
catalogue will then be divided into 25 subsets based on mass and
    ↪ metallicity.
From this we calculate the mean [C/N] ratio for bins with equal
    ↪ numbers of stars
in each subset. From this we find the change in [C/N] over the
    ↪ change in log(g).

@author: Christopher J. Brockett, November 2019
"""

# Import Relevant python packages
import numpy as np # for number handling
import matplotlib.pyplot as plt # produce plots
from astropy.table import Table # for table/data management
from matplotlib.ticker import (MultipleLocator,
                                FormatStrFormatter)
# for styling axis ticks on plots
from astropy.io import ascii as io # to print table of data
import seaborn as sb # style package for plots
sb.set_style("white") # white background for plots
sb.set_style("ticks") # add ticks to axes

apg = Table.read('Apogee_Data/APOGEE_Masses.fits', hdu=1) # Load
    ↪ APOGEE dataset
# That already has had it's masses predicted

# Create a function that will produce edges for a histogram so that
    ↪ each bin
```

```

# contains an equal number of data points
# This ensures that when we divide our data into bins to determine
# mixing rates
# it will not be affected by outliers
def histedges_equalN(x, nbin):
    npt = len(x)
    return np.interp(np.linspace(0, npt, nbin + 1),
                    np.arange(npt),
                    np.sort(x))

# Create a figure of 25 subplots
f, ax = plt.subplots(5, 5, figsize=(15, 15), sharex=True, sharey=
    True)

feh = [0.25, -0.25, -0.75, -1.25, -1.75, -4.00] # List of
# Metallicity selections
masses = [0.5, 1.0, 1.25, 1.5, 2.2, 4.0] # List of Mass Selections
# The last number in each of those lists is an upper bound outside
# the range
# of the data
# Estimated location of the RGBb from Dartmouth Stellar Evolution
# Database
# isochrones.
rgbbedge = [[2.666, 2.661, 2.654, 2.587, 2.50],
             [2.509, 2.500, 2.432, 2.456, 2.4],
             [2.301, 2.277, 2.222, 2.186, 2.1],
             [2.106, 2.060, 2.036, 2.098, 2.0],
             [1.953, 1.895, 1.881, 1.846, 1.8]]

# Create a table to store the [C/N] abundance at the RGBb, RGBt, the
# change
# in [C/N], the change in logg, and mixing rate d[C/N]/dlog(g)
CN = Table(names=('feh_min', 'feh_max', 'mass_min', 'mass_max', ,
    CN_bump',
    'unc_CN_bump', 'CN_tip', 'unc_CN_tip', 'dCN',
    'dlogg', 'dCN/dlogg'))

for i in range(0,5): # Iterate over metallicity
    for k in range(0,5): #Iterate over mass
        if (k==0): # If the first plot in a row, add a label to y-
# axis
            ax[i,k].set_ylabel('{$\geq$[Fe/H]}'.format(feh[i],
                feh[i+1]))
        if (i==0) and (k<4): # If on top row, add a title
            ax[i,k].set_title('{$\leq$M/Mo} < {$\cdot$}'.format(masses[k],
                masses[k+1]))
        elif (i==0) and (k==4): # Edge case for upper limit of masses
            ax[i,k].set_title('{$\leq$M/Mo}'.format(masses[k]))
```

```

if k<4: # subset of data to be plotted
    sub = apg[(apg['M_pred']>=masses[k]) & (apg['M_pred']<
    ↪ masses[k+1]) &
                (apg['FE_H']<=feh[i]) & (apg['FE_H']>feh[i+1])]
else: # Edge case for upper bound
    sub = apg[(apg['M_pred']>=masses[k]) & (apg['FE_H']<=feh[
    ↪ i]) &
                (apg['FE_H']>feh[i+1])]

# Create scatter plot of [C/N] vs log(g)
ax[i,k].scatter(sub['LOGG'], sub['C_FE']-sub['N_FE'], s=0.1,
    ↪ c='k')

# Change parameters for axis ticks
ax[i,k].tick_params(axis='both', which='both', direction='in',
    ↪ )

# Choose the number of bins used to calculate mixing based on
    ↪ the size
# of the subset
if len(sub)<50:
    L = 2
elif len(sub)<150:
    L = 3
elif len(sub)<250:
    L = 4
else:
    L = 5

# split subset into bins with equal numbers of stars, and
    ↪ determine
# distribution of [C/N] and log(g) for each bin, as well as
    ↪ the standard
# deviation of [C/N]
g = histedges_equalN(sub['LOGG'], L)
n, _ = np.histogram(sub['LOGG'], bins=g)
sy, _ = np.histogram(sub['LOGG'], bins=g, weights=(sub['C_FE'-
    ↪ ]-
                    sub['N_FE'])))

sy2, _ = np.histogram(sub['LOGG'], bins=g,
    weights=(sub['C_FE']-sub['N_FE'])*(sub['
    ↪ C_FE']-
                    sub['N_FE'])))

# calculate mean [C/N] for each bin
mean = sy / n
# calculate standard deviation
std = np.sqrt(sy2/n - mean*mean)
# Find the edges of log(g) selections from the mean log(g) of
    ↪ each bin
med = (_[1:] + _[:-1])/2 #

xerr = []

```

```

for x in range(len(_)-1):
    xerr.append((_[x]-_[x+1])/2)
ax[i,k].errorbar(med, mean, yerr=std, xerr=xerr,
                  fmt='rs', label = 'Binned Data')
h = np.where(med==min(med, key=lambda x:abs(x-rgbbedge)))
    ↪ [0] [0]
# If the RGBb is located in the last bin, set mixing rate to
    ↪ 0
if h == 0:
    CN.add_row((feh[i], feh[i+1], masses[k], masses[k+1],
    ↪ mean[h],
        std[h], mean[0], std[0], (mean[0]-mean[h]),
        np.mean((std[0], std[h])), 0, 0))
# Else store relevant info into table (notably [C/N])
else:
    CN.add_row((feh[i], feh[i+1], masses[k], masses[k+1],
    ↪ mean[h],
        std[h], mean[0], std[0], (mean[0]-mean[h]),
        np.mean((std[0], std[h])), (med[0]-med[h]),
        (mean[0]-mean[h])/(med[0]-med[h])))
# Loop over each subset

# Remove space between subplots
f.subplots_adjust(hspace=0)
f.subplots_adjust(wspace=0)
# Set axis limits
ax[0,0].set_xlim(3.9, -0.3)
ax[0,0].set_ylim(-1.7, 1.7)

# Add labels to x and y axes
f.text(0.5, 0.1, '$\log(g)$', ha='center', va='center', fontsize=20)
f.text(0.06, 0.5, '[C/N]', ha='center', va='center', rotation=
    ↪ vertical',
    fontsize=20)

# Change tick parameters
ax[0,0].yaxis.set_major_locator(MultipleLocator(0.5))
ax[0,0].yaxis.set_major_formatter(FormatStrFormatter('%0.1f'))
ax[0,0].yaxis.set_minor_locator(MultipleLocator(0.1))
ax[0,0].xaxis.set_major_locator(MultipleLocator(1))
ax[0,0].xaxis.set_major_formatter(FormatStrFormatter('%0.1f'))
ax[0,0].xaxis.set_minor_locator(MultipleLocator(0.1))
plt.savefig('Plots/APOGEE_CN.eps', bbox_inches='tight', pad_inches
    ↪ =0.1,
        format='eps', dpi=1200) # Save figure as eps file

io.write(CN, format='latex') #print the table of paramaters in latex
    ↪ format

```

Bibliography

- Abolfathi, B., Aguado, D. S., Aguilar, G., Allende Prieto, C., Almeida, A., *et al.*, 2018. *ApJS*, 235(2):42.
- Adelberger, E. G., García, A., Robertson, R. G. H., Snover, K. A., Balantekin, A. B., *et al.*, 2011. *Reviews of Modern Physics*, 83(1):195–246.
- Aerts, C., Christensen-Dalsgaard, J., and Kurtz, D. W., 2010. *Asteroseismology*. Springer, Dordrecht.
- Ahn, C. P., Alexandroff, R., Allende Prieto, C., Anders, F., Anderson, S. F., *et al.*, 2014. *ApJS*, 211(2):17.
- Angelou, G. C., Church, R. P., Stancliffe, R. J., Lattanzio, J. C., and Smith, G. H., 2011. *ApJ*, 728(2):79.
- Angelou, G. C., Stancliffe, R. J., Church, R. P., Lattanzio, J. C., and Smith, G. H., 2012. *ApJ*, 749:128.
- Asplund, M., Grevesse, N., Sauval, A. J., and Scott, P., 2009. *Annual Review of Astronomy and Astrophysics*, 47:481–522.
- Borucki, W. J., Koch, D., Basri, G., Batalha, N., Brown, T., *et al.*, 2010. *Science*, 327(5968):977.
- Busso, M., Wasserburg, G. J., Nollett, K. M., and Calandra, A., 2007. *ApJ*, 671(1):802–810.
- Campbell, S. W. and Lattanzio, J. C., 2008. *A&A*, 490(2):769–776.
- Carbon, D. F., Langer, G. E., Butler, D., Kraft, R. P., Suntzeff, N. B., Kemper, E., Trefzger, C. F., and Romanishin, W., 1982. *The Astrophysical Journal Supplement Series*, 49:207–258.
- Carroll, B. W. and Ostlie, D. A., 2006. *An Introduction to Modern Astrophysics*. Pearson Education, 2nd edition.
- Chanamé, J., Pinsonneault, M., and Terndrup, D. M., 2005. *ApJ*, 631(1):540–571.
- Charbonnel, C., Brown, J. A., and Wallerstein, G., 1998. *A&A*, 332:204–214.

- Charbonnel, C. and Lagarde, N., 2010. *A&A*, 522:A10.
- Charbonnel, C. and Palacios, A., 2004. In A. Maeder and P. Eenens (editors), ‘Stellar Rotation,’ volume 215 of *IAU Symposium*, page 440.
- Charbonnel, C. and Zahn, J. P., 2007. *A&A*, 467:L15–L18.
- Christensen-Dalsgaard, J., 2002. *Reviews of Modern Physics*, 74(4):1073–1129.
- Christensen-Dalsgaard, J., 2015. *MNRAS*, 453(1):666–670.
- Clayton, D. D., 1968. *Principles of Stellar Evolution and Nucleosynthesis*. McGraw-Hill.
- Dearborn, D. S. P., Lattanzio, J. C., and Eggleton, P. P., 2006. *ApJ*, 639(1):405–415.
- Dearborn, D. S. P., Steigman, G., and Tosi, M., 1996. *ApJ*, 465:887.
- Decressin, T., Charbonnel, C., Siess, L., Palacios, A., Meynet, G., and Georgy, C., 2009. *A&A*, 505(2):727–733.
- Denissenkov, P. A., 2010. *ApJ*, 723:563–579.
- Denissenkov, P. A., 2012. *ApJ*, 753(1):L3.
- Denissenkov, P. A. and Merryfield, W. J., 2011. *ApJ*, 727:L8.
- Dotter, A., Chaboyer, B., Jevremović, D., Kostov, V., Baron, E., and Ferguson, J. W., 2008. *ApJS*, 178(1):89–101.
- Eggleton, P. P., Dearborn, D. S. P., and Lattanzio, J. C., 2006. *Science*, 314(5805):1580.
- Eggleton, P. P., Dearborn, D. S. P., and Lattanzio, J. C., 2007. In F. Kupka, I. Roxburgh, and K. L. Chan (editors), ‘Convection in Astrophysics,’ volume 239 of *IAU Symposium*, pages 286–293.
- Eggleton, P. P., Dearborn, D. S. P., and Lattanzio, J. C., 2008. *ApJ*, 677:581–592.
- Eisenstein, D. J., Weinberg, D. H., Agol, E., Aihara, H., Allende Prieto, C., et al., 2011. *AJ*, 142(3):72.
- Elsworth, Y., Hekker, S., Basu, S., and Davies, G. R., 2017. *MNRAS*, 466(3):3344–3352.
- García Pérez, A. E., Allende Prieto, C., Holtzman, J. A., Shetrone, M., Mészáros, S., et al., 2016. *AJ*, 151(6):144.
- Gilmore, G., Randich, S., Asplund, M., Binney, J., Bonifacio, P., et al., 2012. *The Messenger*, 147:25–31.
- Gratton, R. G., Sneden, C., Carretta, E., and Bragaglia, A., 2000. *A&A*, 354:169–187.
- Gray, D. F., 1975. *The Observation and Analysis of Stellar Photospheres*. Wiley, New York.
- Gunn, J. E., Siegmund, W. A., Mannery, E. J., Owen, R. E., Hull, C. L., et al., 2006. *AJ*, 131(4):2332–2359.
- Harris, W. E., 1996. *AJ*, 112:1487.
- Harris, W. E., 2010. *arXiv e-prints*, arXiv:1012.3224.

- Henkel, K., Karakas, A. I., Casey, A. R., Church, R. P., and Lattanzio, J. C., 2018. *ApJ*, 863:L5.
- Henkel, K., Karakas, A. I., and Lattanzio, J. C., 2017. *MNRAS*, 469(4):4600–4612.
- Holtzman, J. A., Hasselquist, S., Shetrone, M., Cunha, K., Allende Prieto, C., *et al.*, 2018. *AJ*, 156(3):125.
- Holtzman, J. A., Shetrone, M., Johnson, J. A., Allende Prieto, C., Anders, F., *et al.*, 2015. *AJ*, 150(5):148.
- Hon, M., Stello, D., García, R. A., Mathur, S., Sharma, S., Colman, I. L., and Bugnet, L., 2019. *MNRAS*, page 610.
- Howell, S. B., Sobeck, C., Haas, M., Still, M., Barclay, T., *et al.*, 2014. *PASP*, 126(938):398.
- Hubbard, E. N. and Dearborn, D. S. P., 1980. *ApJ*, 239:248–252.
- Iben, J., Icko, 1965. *ApJ*, 142:1447.
- Iben, J., Icko, 1967a. *Science*, 155:785–796.
- Iben, J., Icko, 1967b. *ApJ*, 147:650–663.
- Iben, J., Icko, 1967c. *Annual Review of Astronomy and Astrophysics*, 5:571–626.
- Iben, J., Icko, 1967d. *ApJ*, 147:624–649.
- Jordi, C., Gebran, M., Carrasco, J. M., de Bruijne, J., Voss, H., Fabricius, C., Knude, J., Vallenari, A., Kohley, R., and Mora, A., 2010. *A&A*, 523:A48.
- Kippenhahn, R., Weigert, A., and Weiss, A., 2012. *Stellar Structure and Evolution*. Springer, Berlin, Heidelberg, 2nd edition.
- Kjeldsen, H. and Bedding, T. R., 1995. *A&A*, 293:87–106.
- Lagarde, N., Charbonnel, C., Decressin, T., and Hagelberg, J., 2011. *A&A*, 536:A28.
- Lagarde, N., Decressin, T., Charbonnel, C., Eggenberger, P., Ekström, S., and Palacios, A., 2012. *A&A*, 543:A108.
- Lagarde, N., Reylié, C., Robin, A. C., Tautvaišienė, G., Drazdauskas, A., *et al.*, 2019. *A&A*, 621:A24.
- Langer, G. E., Kraft, R. P., Carbon, D. F., Friel, E., and Oke, J. B., 1986. *Publications of the Astronomical Society of the Pacific*, 98:473–485.
- Lind, K., Primas, F., Charbonnel, C., Grundahl, F., and Asplund, M., 2009. *A&A*, 503(2):545–557.
- Lind, K., Primas, F., Charbonnel, C., Grundahl, F., and Asplund, M., 2010. In C. Charbonnel, M. Tosi, F. Primas, and C. Chiappini (editors), ‘Light Elements in the Universe,’ volume 268 of *IAU Symposium*, pages 263–268.
- Majewski, S. R., Schiavon, R. P., Frinchaboy, P. M., Allende Prieto, C., Barkhouser, R., *et al.*, 2017. *AJ*, 154(3):94.
- Martell, S. L., Smith, G. H., and Briley, M. M., 2008. *AJ*, 136:2522–2532.

- Masseron, T., García-Hernández, D. A., Mészáros, S., Zamora, O., Dell’Agli, F., Allende Prieto, C., Edvardsson, B., Shetrone, M., Plez, B., and Fernández-Trincado, J. G., 2019. *A&A*, 622:A191.
- Masseron, T., Merle, T., and Hawkins, K., 2016. ‘BACCHUS: Brussels Automatic Code for Characterizing High accUracy Spectra.’
- Nataf, D. M., Wyse, R. F. G., Schiavon, R. P., Ting, Y.-S., Minniti, D., Cohen, R. E., Fernández-Trincado, J. G., Geisler, D., Nitschelm, C., and Frinchaboy, P. M., 2019. *AJ*, 158(1):14.
- Nordhaus, J., Busso, M., Wasserburg, G. J., Blackman, E. G., and Palmerini, S., 2008. *ApJ*, 684(1):L29.
- Palacios, A., Charbonnel, C., Talon, S., and Siess, L., 2006. *A&A*, 453(1):261–278.
- Palacios, A., Talon, S., Charbonnel, C., and Forestini, M., 2003. *A&A*, 399:603–616.
- Palmerini, S., Busso, M., Maiorca, E., and Guandalini, R., 2009. *Publ. Astron. Soc. Australia*, 26(3):161–167.
- Pedregosa, F., Varoquaux, G., Gramfort, A., Michel, V., Thirion, B., et al., 2011. *Journal of Machine Learning Research*, 12:2825–2830.
- Pinsonneault, M. H., Elsworth, Y., Epstein, C., Hekker, S., Mészáros, S., et al., 2014. *ApJS*, 215(2):19.
- Pinsonneault, M. H., Elsworth, Y. P., Tayar, J., Serenelli, A., Stello, D., et al., 2018. *ApJS*, 239(2):32.
- Schönberg, M. and Chandrasekhar, S., 1942. *ApJ*, 96:161.
- Shetrone, M., Tayar, J., Johnson, J. A., Somers, G., Pinsonneault, M. H., et al., 2019. *ApJ*, 872:137.
- Siess, L., Dufour, E., and Forestini, M., 2000. *A&A*, 358:593–599.
- Silva Aguirre, V., Bojsen-Hansen, M., Slumstrup, D., Casagrande, L., Kawata, D., et al., 2018. *MNRAS*, 475:5487–5500.
- Smith, G. H. and Martell, S. L., 2003. *Publications of the Astronomical Society of the Pacific*, 115:1211–1219.
- Stello, D., Chaplin, W. J., Basu, S., Elsworth, Y., and Bedding, T. R., 2009. *MNRAS*, 400:L80–L84.
- Stello, D., Huber, D., Bedding, T. R., Benomar, O., Bildsten, L., Elsworth, Y. P., Gilliland, R. L., Mosser, B., Paxton, B., and White, T. R., 2013. *ApJ*, 765(2):L41.
- Stern, M. E., 1960. *Tellus Series A*, 12(2):172–175.
- Sweigart, A. V. and Mengel, J. G., 1979. *ApJ*, 229:624–641.
- Ting, Y.-S., Conroy, C., Rix, H.-W., and Cargile, P., 2019. *ApJ*, 879(2):69.
- Ulrich, R. K., 1972. *ApJ*, 172:165.

- Virtanen, P., Gommers, R., Oliphant, T. E., Haberland, M., Reddy, T., *et al.*, 2019. *arXiv e-prints*, arXiv:1907.10121.
- Wilson, J. C., Hearty, F. R., Skrutskie, M. F., Majewski, S. R., Holtzman, J. A., *et al.*, 2019. *PASP*, 131(999):055001.
- Zamora, O., García-Hernández, D. A., Allende Prieto, C., Carrera, R., Koesterke, L., *et al.*, 2015. *AJ*, 149(6):181.
- Zinn, R., 1973. *ApJ*, 182:183–188.